UNIVERSITÉ DE MONTRÉAL

III-V HIGH SPEED ELECTRO-OPTIC LASER MODULATORS USING SLOW WAVE STRUCTURE TECHNIQUE

HAMID REZA KHAZAEI
DEPARTEMENT DE GÉNIE ÉLECTRIQUE ET DE
GÉNIE INFORMATIQUE
ÉCOLE POLYTECHNIQUE DE MONTRÉAL

THÉSE PRÉSENTÉE EN VUE DE L'OBTENTION
DU DIPLÔME DE PHILOSOPHIAE DOCTOR (Ph.D.)
(GÉNIE ÉLECTRIQUE)
OCTOBRE 1999

UNIVERSITÉ DE MONTRÉAL

ÉCOLE POLYTECHNIQUE DE MONTRÉAL

Cette thèse intitulée:

III-V HIGH SPEED ELECTRO-OPTIC LASER MODULATORS USING SLOW WAVE STRUCTURE TECHNIQUE

Présentée par: KHAZAEI Hamid Reza

en vue de l'obtention du diplôme de: Philosophiae Doctor

a été dûment acceptée par le jury d'examen constitué de:

M. MACIEJKO Romain, Ph.D. , président

M. GHANNOUCHI Fadhel M., Ph.D. , membre et directeur de recherche

M. BEROLO Ezio, Ph.D. , membre et codirecteur de recherche

M. KOUKI Amar B., Ph.D. , membre

M. ROY Langis, Ph.D. , membre externe

To the Loving Memory of My Father

ACKNOWLEDGEMENTS

During the course of my thesis work, there were many people who were instrumental in helping me. Without their guidance, help and patience, I would have never been able to accomplish the work of this thesis. I would like to take this opportunity to acknowledge some of them. I would like to thank my thesis advisors, Professor Fadhel M. Ghannouchi and Dr. Ezio Berolo, both of whom were driving factors to the successful completion of this research project. Their consistent advice, encouragement, and confidence are highly appreciated.

Special thanks go to Dr. Weijian Wang at Communications Research Centre (CRC) for his insight in lab experiments and our many discussions. My fellow colleagues at microelectronic facility of CRC were Rob James and S. Bernhoff. Without their work and dedication none of this work would have been possible.

I must give immense thanks to my wife Nasrin. Her love, support, and encouragement during long nights of work were of immeasurable value to me.

This research was supported in part by grant from Industry Canada. Nortel Networks supplied some of the substrates and materials used in this program.

RÉSUMÉ

Les modulateurs de laser externes sont des composants essentiels dans le développement des réseaux de transmission optique de longue distance à haute vitesse. Les modulateurs électro-optiques linéaires à semiconducteur basé sur le principe de l'onde progressive sont des dispositifs prometteurs pour la réalisation de modulation haute vitesse dépassant 100 GHz et à faible étalement spectral. Ils offrent également le potentiel pour l'intégration monolithique avec des sources de laser et d'autres dispositifs électroniques et photoniques. Il est bien connu que la limite dominante de la largeur de bande des modulateurs électro-optiques à onde progressive soit le désaccord de vitesse entre le signal optique et le signal de modulation RF dans la région d'interaction. Lorsqu'en accord de vitesse, la largeur de bande d'un modulateur est limitée principalement par les pertes micro-ondes inévitables des électrodes. Ces modulateurs souffrent également d'une tension de commutation relativement élevée due aux coefficients électro-optiques très petits.

Cette thèse se concentre sur le développement des modulateurs électro-optiques à onde progressive sur pastille de semi-conducteur. L'effet électro-optique linéaire (effet Pockels) est exploité pour convertir l'information du signal électrique au signal optique. Le projet se compose de trois étapes principales: i) conception des électrodes planaires à haute vitesse, ii) caractérisation du matériau, et iii) mesures. Différents types de modulateurs, y compris les modulateurs d'intensité Mach-Zehnder sensibles et peu sensibles à la polarisation, et convertisseurs de mode/polarisation, sont considérés.

La première partie de la thèse présente la conception de différents types de structures planaires chargées à intervalles périodiques. Certaines de ces structures utilisent des rubans coplanaires (CPS), d'autres des guides d'ondes coplanaires (CPW). Des éléments capacitifs sont ajoutés aux structures conventionnelles CPS et CPW pour réduire la vitesse de phase du signal micro-onde. Les électrodes sont également optimalisées pour obtenir la perte d'insertion micro-onde minimale. La séparation des électrodes est également un paramètre de conception important qui affecte la tension de commutation et le désaccord de vitesse. Ces électrodes sont intégrées avec les structures

optiques telles que l'interféromètre optique de Mach-Zehnder pour réaliser des modulateurs d'intensité.

Une partie de la thèse traite l'effet de la densité de porteurs de charge dans le substrat sur la performance des électrodes planaires. L'effet des porteurs de charge libres est employé pour expliquer et modéliser les pertes micro-ondes observées dans les modulateurs à onde progressive quand les électrodes à structures lentes sont fabriquées sur les matériaux optiques constitués de couches hétérostructures dopées involontairement. Les résultats expérimentaux et ceux en obtenus par modélisation prouvent qu'il y a une limite résiduelle critique de dopage au-dessus de laquelle la perte micro-onde augmente linéairement avec la densité de dopage.

La dernière partie de la thèse présente les résultats de mesure comprenant des mesures optiques, électriques, et électro-optiques. Des mesures de largeur de bande de modulation ont été faites jusqu'à 40 GHz sans atteindre le niveau de –3 dB. Quelques modulateurs ont démontré une tension de commutation aussi basse que 8,5 V.

ABSTRACT

External laser modulators are essential components in the development of high-speed long-haul optical communication networks. Semiconductor traveling wave linear electro-optic modulators are promising devices in achieving high-speed modulation in excess of 100 GHz and low chirp. They also offer the potential for monolithic integration with laser sources and other electronic and photonic devices. It is well known that the dominant bandwidth limitation of traveling wave electro-optic modulators is the velocity mismatch between the optical signal and RF modulating signal in the interaction region. In the velocity-matched condition, the modulator bandwidth is limited mainly by the unavoidable microwave losses of the electrodes. These modulators also suffer from relatively high half-wave voltage due to very small electro-optic coefficients.

This thesis focuses on the development of semiconductor traveling wave electro-optic modulators. The linear electro-optic effect (Pockels effect) is exploited to carry information from the electrical signal to the optical signal. The project consists of three main stages: *i*) design of high-speed planar electrodes, *ii*) material characterization, and *iii*) measurements. Different types of modulators, including polarization sensitive and insensitive Mach-Zehnder intensity modulators, and mode/polarization converters, are considered.

The first part of the thesis presents the design of different types of periodically loaded coplanar strips (CPS) and coplanar waveguides (CPW). Conventional CPS's and CPW's are loaded with capacitive elements to reduce the phase velocity of the microwave signal. The electrodes are also optimized to exhibit minimum microwave insertion loss. The interelectrode gap is also an important design parameter which affects both the half-wave voltage and velocity mismatch. These electrodes are integrated with optical structures such as Mach-Zehnder optical interferometer to realize intensity modulators.

Part of the thesis deals with the effect of substrate carrier density on the performance of planar electrodes. The free charge carrier effect is used to explain and model microwave losses observed in traveling wave modulators when the slow-wave

electrodes are fabricated on unintentionally doped heterostructure optical materials. Modeling and experimental results show that there is a critical residual doping limit, above which the microwave loss increases linearly with doping density.

The last part of the thesis presents the measurement results including optical, electrical, and electro-optical measurements. Modulation bandwidths were measured up to 40 GHz and no 3-dB roll-off was observed. Some modulators demonstrated a half-wave voltage as low as 8.5 V.

CONDENSÉ EN FRANÇAIS

1. Introduction:

Le développement sans cesse croissant des systèmes de télécommunications par fibre optique nécessite la mise au point de composants optoélectroniques capables de fonctionner à des vitesses élevées. Du côté transmetteur, le développement des modulateurs efficaces et ultra rapides est nécessaire. Pour ce faire, le signal optique (laser) peut être modulé soit directement ou par un modulateur externe. La modulation directe du laser a l'avantage d'être relativement simple, mais l'inconvénient est que la largeur de la bande de fréquence se trouve limitée par l'étalement spectral. Pour des systèmes à haut débit ($\geq$ 10 Gbit/s), le choix de la méthode de la modulation externe s'avère le plus intéressant car il permet la modulation des différentes sources optiques, présente un étalement spectral moins important et donc permet la transmission des signaux optiques à 1.55 μm sur des fibres monomodes à longue distance.

Ces modulateurs ont été conçus en exploitant les propriétés électro-optiques de Niobate de Lithium. D'autre part, le développement de procédés de croissance et celui de la fabrication de la famille de semi-conducteurs III-V ont permis d'augmenter considérablement la qualité des couches minces utilisées dans la fabrication de dispositifs optoélectroniques. Ce progrès a renouvelé l'intérêt dans ces matériaux, car ils offrent l'avantage d'intégrer de façon monolithique les dispositifs micro-électroniques avec les dispositifs photoniques.

Les modulateurs électro-optiques à onde progressive sont un choix avantageux pour obtenir des largeurs de bande élevées. Ils utilisent d'une part l'effet électro-optique linéaire (l'effet Pockels) qui consiste à induire un changement d'indice de réfraction du cristal à l'aide d'un champ électrique, et d'autre part l'effet Stark (Quantum Confined Stark Effect) qui est particulièrement prononcé dans les dispositifs à puits quantiques

multiples (MQW). Les dimensions de ces modulateurs sont réduites mais leurs caractéristiques varient fortement avec la longueur d'onde du signal optique; de plus, le problème d'étalement spectral se pose.

Durant la conception des modulateurs à onde progressive, il faut égaliser la vitesse de phase du signal modulant et la vitesse de groupe du signal optique, car un désaccord des deux vitesses limiterait la largeur de bande disponible. L'accord des vitesses peut être obtenu en utilisant des électrodes à charge capacitive dites "structures lentes". Ces structures permettent de ralentir la vitesse de propagation du signal micro-ondes à celle de propagation du signal optique. Le principe des structures lentes est d'ajouter des éléments capacitifs ou inductifs à intervalles périodiques aux structures planaires, ceci dans le but d'augmenter la capacité et l'inductance par unité de longueur du guide.

2. Objectifs :

Le but de ce projet est de développer des modulateurs électro-optique à ondes progressives ultra rapides en utilisant des structures lentes. Les étapes suivantes sont donc nécessaires.

1. Conception, optimisation, et fabrication du substrat semi-conducteur "pastille"
2. Caractérisation des matériaux semi-conducteurs en ce qui concerne la densité des porteurs libres
3. Conception, optimisation, fabrication, et mesure des structures lentes
4. Conception, optimisation, fabrication, et mesure guides d'ondes optiques
5. Faire simultanément des mesures micro-ondes et optiques

L'intégration de ces modulateurs avec le signal optique (laser) de façon monolithique constitue un travail très intéressant à développer dans l'avenir.

3. Théorie :

L'effet électro-optique linéaire (l'effet Pockels) utilisé par ces modulateurs consiste à induire un changement d'indice de réfraction du cristal à l'aide d'un champ électrique. Les propriétés optiques d'un cristal peuvent être décrites par son ellipsoïde d'indice ou indicatrice. Cette dernière se déforme en présence d'un champ électrique. L'arséniure de gallium (GaAs) et phosphure d'indium (InP) sont des cristaux isotropes appartenant au groupe de symétrie $\bar{4}3m$ de la famille des Zincblende. La croissance cristalline des substrats GaAs et InP s'effectue généralement dans le plan [100]. Pour la modulation optique dans ce type de substrat et dans le cas ou le signal optique se propage selon la direction $[0\bar{1}1]$, deux orientations sont généralement utilisées pour l'application du champ électrique. On peut appliquer un champ électrique selon la direction [100], perpendiculaire à la surface de pastille, ou encore selon[011], parallèle à la surface.

Le champ électrique selon [100] induit un changement d'indice de réfraction du cristal selon [011] (mode TE). Ce champ électrique n'a aucun effet sur le mode optique TM. On obtient donc un modulateur de phase uniquement pour le mode TE. Dans ce cas, le guide d'onde optique est situé en dessous de l'électrode. Le guide d'onde optique est constitué des couches hétérostructures de type AlGaAs/GaAs/AlGaAs ou InP/InGaAsP/InP.

Lorsqu'on applique un champ électrique parallèle à la surface du guide d'onde optique, celui-ci doit être situé entre les électrodes du signal et celui de la masse. Dans ce cas les axes principaux de l'ellipsoïde d'indice sont tournés selon [111] et $[\bar{1}11]$. Il y a alors un couplage entre les modes TE et TM qui joue la fonction d'un convertisseur de polarisation/mode. Afin d'éviter une absorption excessive du signal optique causée par la proximité de l'électrode, on ajoute une couche isolante entre l'électrode et le guide d'onde optique.

Il est nécessaire d'utiliser un interféromètre optique Mach-Zehnder (MZI) afin de convertir la modulation de phase et la conversion de mode en modulation d'intensité.

On considère trois types de modulateurs décrits ci-dessous:

1. Modulateur d'intensité dépendant de la polarisation (TE mode) : un MZI est intégré avec une structure à guides d'ondes coplanaires (CPW) de façon que l'un des bras de MZI est situé en-dessous de l'électrode du signal et l'autre est situé en-dessous de l'électrode de masse.

2. Modulateur d'intensité indépendant de la polarisation : les bras de MZI sont situés entre l'électrode du signal et celui de la masse d'un CPW.

3. Convertisseur de Mode : un guide d'onde optique est situé entre les électrodes du signal et de la masse d'une structure à rubans coplanaires (CPS).

4. Structures Lentes :

La conception d'un modulateur à ondes progressives ultra rapide nécessite l'utilisation une structure CPW et CPS pour propager le signal modulant aux fréquences micro-ondes. L'avantage des structures coplanaires face aux structures micro-rubans est la présence du plan de masse à la surface. L'indice de réfraction effectif micro-ondes dans une structure coplanaire sur GaAs ou InP est inférieur à l'indice de réfraction optique. Donc la vitesse de phase du signal modulant sera supérieure à la vitesse de groupe du signal optique. Comme la largeur de bande d'un modulateur électro-optique à onde progressive est limitée par un désaccord des vitesses, il serait avantageux de ralentir la propagation du signal modulant. On peut atteindre cet objectif avec des structures coplanaires non uniformes. On ajoute un élément capacitif à intervalles périodiques afin d'augmenter la valeur de la capacité linéique. La conception de structures lentes a pour

but d'obtenir principalement une impédance caractéristique 50 Ω, une vitesse de phase de 8.5 cm/nsec (qui est la vitesse de groupe du signal optique), et une perte micro-onde réduite.

Nous avons conçu trois groupes de masques micro-électroniques, LIT-1, LIT-2, et LIT3. Plusieurs types de structures lentes sont présentes dans ces masques. Les structures CPW's ou CPS's contiennent des éléments capacitifs qui ont été ajoutés par intervalles périodiques afin de ralentir la propagation du signal modulant. Plusieurs géométries ont permis de vérifier la validité des résultats obtenus avec le simulateur électromagnétique. Les différentes structures utilisées servent également à comparer leur efficacité en ce qui concerne les pertes, les vitesses de phase, et la dispersion, et enfin de déceler celles qui sont les plus performantes. L'annexe I et l'annexe II décrivent en détail les structures présentes sur ces masques. Ces structures sont du type CPW, CPWA, CPWB, CPWC, CPWD, CPWD-aie (asymétrique), CPSD, et CPSD-id (CPS intrelacé). Dans les structures lentes de type CPWD-as, la longueur des ailettes ajoutées à l'électrode centrale, L_{SS}, est plus petite que la longueur des ailettes ajoutées aux électrodes de terre, L_{SG}. Les structures lentes du type CPWD-as sont particulièrement plus performantes que celles du type CPW (symétrique), car elles présentent certains avantages décrits ci-dessous:

a) la séparation des bras de l'interféromètre Mach-Zehnder (MZ) est très petite ce qui permet de réduire la perte optique de la jonction, la longueur de l'interféromètre MZ et par conséquent la longueur du modulateur;

b) la longueur effective de la structure lente du type CPWD-as est plus grande que la longueur physique, c'est à dire que le champ électrique appliqué devient plus important quand le signal modulant se propage dans la direction de propagation.

On a utilisé le simulateur électromagnétique *Sonnet* qui permet une analyse en 2.5D des structures lentes. Ces simulateurs nous permettent également d'obtenir les paramètres *S* équivalents des différentes structures. L'impédance caractéristique, la constante de propagation, ainsi que la vitesse de phase peuvent être trouvées a partir de la matrice ABCD, déduite de la matrice S.

5. Structures Optiques

Pour concevoir nos structures optiques, nous nous sommes servis de la méthode de l'indice effectif et de la méthode de propagation du champ optique BPM (Beam propagation method). On a conçu deux pastilles hétérostructures du type $Al_yGa_{1-y}As$-$Al_xGa_{1-x}As$-$Al_yGa_{1-y}As$ avec y = 0.13 et x = 0.08 pour la première pastille et y = 0.3 et x = 0 pour la deuxième. Les guides optiques et les structures lentes ont été déposées sur ces pastilles. Le guidage vertical de la lumière est assuré par la différence de concentration d'aluminium qui produit une différence d'indice de réfraction dans les couches minces. Pour le confinement latéral, on utilise la méthode qui consiste à graver dans la couche supérieure de la pastille, un guide d'onde à crête, afin de créer une différence d'indice effectif. La hauteur et la largeur de la crête ont été choisies pour obtenir un guide monomode. L'indice de réfraction de groupe de ces pastilles hétérostructures est calculé par la méthode de l'indice effectif, soit $Ng \approx 3.5$ où la vitesse de groupe est de 8.5 cm/nsec.

6. Caractérisation des Matériaux de Substrats:

On a remarqué que les pertes micro-ondes dépendent fortement du dopage résiduel dans les couches minces hétérostructures de la pastille. Les résultats obtenus montrent qu'au delà d'une certaine valeur critique, la perte micro-onde est si grande que toute modulation électro-optique aux hyperfréquences serait quasiment impossible. Nous

avons fait une étude plus détaillée sur ce point afin de déterminer plus exactement la valeur critique du dopage. Nous avons fabriqué des structures lentes sur plusieurs pastilles hétérostructure à différents dopages. Les résultats obtenus concernant les pertes micro-ondes ont été illustrés au Chapitre 5 de la thèse. On trouve une valeur critique du dopage égale à $N_d \sim 5\times10^{14}$ /cm^3. Toutes les pastilles hétérostructures utilisées dans cette thèse ont été fabriquées à dopages inférieur à 5×10^{14} /cm^3. Les résultats des mesures micro-ondes sont très encourageants, les pertes micro-ondes qu'on a obtenues sont très proches des pertes micro-ondes sur la pastille semi-isolante GaAs. Les résultats expérimentaux sont en très bon accord avec les résultats numériques obtenus par ordinateur.

7. Résultats Expérimentaux:

7.1 Mesures Optiques:

Les mesures optiques ont été réalisées sur les guides d'ondes optiques fabriquées sur des pastilles hétérostructures. Ces mesures permettent de déterminer si le guide est monomode ou multimode, la perte optique, et le profil du mode. Deux méthodes ont été utilisées afin de déterminer les pertes optiques, "Fabry-Perot" et "cut-back", on a obtenu des guide d'ondes optiques à faibles pertes (inférieurs à 1.5 dB/cm). Ces pertes peuvent être causées par l'absorbtion par des porteurs libres ou la dispersion (interne et externe).

7.2 Mesures Micro-ondes:

Nous avons utilisé des structures lentes fabriquées sur la pastille semi-isolante d'arséniure de gallium, puis nous avons mesuré la propagation du signal modulant par un analyseur de réseau de 0.045 a 40 GHz qui donne les paramètres S. Un programme en langage FORTRAN a été développé. Il permet de calculer l'impédance caractéristique, la vitesse de phase, l'indice effectif et la perte micro-onde. Les résultats obtenus montrent un très bon accord avec les résultats numériques calculés par ordinateur. Cependant on

observe des variations brusques pour quelques structures sur le masque. Nous pourrons supposer que ces variations ont pour origine un défaut de fabrication ou bien la géométrie des structures. Les impédances caractéristiques et les indices effectifs mesurés prennent généralement les valeurs respectives de 45 ± 5 et 3.4. On peut les modifier dans la prochaine conception en introduisant moins de capacité par unité de longueur du guide. Les pertes micro-ondes ($\approx$3 dB/cm) que nous avons atteint sont parmi les plus basses pertes micro-ondes obtenues jusqu'à présent. Nous avons aussi remarqué qu'il existe des variations presque périodiques des impédances caractéristiques surtout pour les structures du type guide d'ondes coplanaires sans encoches et ailettes.

On remarque que les pertes micro-ondes des structure du type CPWD et particulièrement CPWD-as sont les plus faibles. Ces structures ont aussi un facteur de recouvrement longitudinale élevé (0.9). En effet la structure CPWD-as apparaît comme la plus intéressante structure à guides d'ondes coplanaires.

Nous avons fabriqué les mêmes structures lentes sur une pastille à semi-isolant de phosphure d'indium (InP). Des mesures micro-ondes effectuées avec l'analyseur de réseau HP8510C montrent un bon accord entre les résultats numériques et ceux obtenus avec la pastille semi-isolante en arséniure de gallium. Les structures lentes sur une pastille à base de InP présentent des pertes plus faibles que celles rencontrées avec les pastilles GaAs, de plus les indices effectifs sont légèrement différents.

Les structures lentes du type CPSD-id (CPS intrelacé) sont appropriés pour la modulation électro-optique à haute fréquence. Avec ces structures, nous avons réussi à avoir un désaccord de vitesses inférieur à 5%, une impédance caractéristique située entre 40 Ω et 50 Ω, et des pertes micro-ondes très faibles. La comparaison des résultats expérimentale avec la simulation montre un très bon accord.

Pour accorder la vitesse de phase du signal modulant et du signal optique, on a mesuré la structure lente de type CPSD. Cette structure est utilisée pour réaliser des

convertisseurs de modes, les résultats obtenus sont très encourageants. En effet l'impédance caractéristique est d'environ 50 Ω, le désaccord des vitesses est inférieur a 5%, et les pertes micro-onde obtenues sont très faibles, pour ce type de structure. À notre meilleure connaissance, on n'a pas enregistré d'aussi faible valeur de pertes dans la littérature.

7.3 Mesures Électro-Optiques:

Les mesures de modulation électro-optique ont été faites afin de déterminer des largeurs de bandes disponibles et des fonctions de transfert. La fonction de transfert permet de calculer la tension de commutation et le coefficient d'extinction. On a utilisé la méthode hétérodyne pour mesurer des largeurs de bandes disponibles jusqu'à 40 GHz. Cette méthode nous permet d'augmenter la largeur de bande disponible du système de mesure. Les réponses fréquentielles sont presque constantes ce qui montre que la largeur de bande des modulateurs est supérieure a 40 GHz.

D'autre part on a mesuré des fonctions de transfert des modulateurs en appliquant un signal haute amplitude (de -80 V jusqu'à 80 V) à 50 KHz. Les modulateurs d'intensité dépendent de la polarisation. Avec la structure lente du type CPWD-as on obtient des tensions de commutations inférieures à 8.5 V avec des coefficients d'extinctions supérieurs à 13 dB. Pour les modulateurs dont les structures lentes sont du type CPSD-id, la tension de commutation est de 9.5 V et le coefficient d'extinction est de 13 dB.

Un analyseur de polarisation est utilisé à la sortie d'un convertisseur de mode afin de mesurer la fonction de transfert. On applique un signal optique TE ou TM à l'entrée du guide d'onde optique. On a obtenu les tensions de commutations de 9 V avec un coefficient d'extinction de 12 dB. La tension de polarisation dans ce cas est très élevée (60 V) et l'efficacité de modulation est inférieure à 80%. Ce type de modulateur dépend aussi de la polarisation du signal d'entrée.

On doit appliquer une tension de polarisation pour faire fonctionner des modulateurs. Cette tension fait varier la tension de commutation et le coefficient d'extinction. La valeur minimale qu'on peut avoir pour une tension de commutation est de 14 V, le coefficient d'extinction correspondant est de 10 dB. C'est pour cela qu'on a appliqué une tension de polarisation de 40 V à l'un des électrodes de masse du modulateur à structures lentes.

TABLE OF CONTENTS

LIST OF APPENDICES

LIST OF TABLES

LIST OF FIGURES

LIST OF ABREVIATIONS

CPS	Coplanar strip
CPSD	Periodically loaded coplanar strip type D (see Appendix I)
CPSD-id	Interdigitated coplanar strip type D (see Appendix I)
CPW	Coplanar waveguide
CPWA	Periodically loaded coplanar waveguide type A (see Appendix I)
CPWB	Periodically loaded coplanar waveguide type B (see Appendix I)
CPWC	Periodically loaded coplanar waveguide type C (see Appendix I)
CPWD	Periodically loaded coplanar waveguide type D (see Appendix I)
CPWD-as	Asymmetric CPWD (see Appendix I)
Gbit/s	Gigabit per second
LPE	Liquid phase epitaxy
MBE	Molecular beam epitaxy
MIS	Metal-insulator-semiconductor
MMI	Multimode interferometer
MOCVD	Metal-organic chemical vapor deposition
MQW	Multiple quantum well
MZI	Mach-Zehnder interferometer
OEIC	Optoelectronic integrated circuits
PDL	Polarization dependent loss
PMS	Planar microstrip
SI-GaAs	Semi-insulating gallium arsenide
SI-InP	Semi-insulating indium phosphide

CHAPTER 1

Introduction

As a consequence of our seemingly insatiable urge for information, long and medium distance communications are carried by glass fibers to enhance the transmission capacity. The expectation is that in the beginning of the next century most data transmission will take place via a worldwide optical and satellite network. High-speed external modulators are necessary components in such optical communication systems. This thesis concentrates on the development of ultrahigh-speed traveling wave electro-optic external modulators using slow wave electrodes on Gallium Arsenide (GaAs) and Indium Phosphide (InP). The bandwidth of these modulators can extend to the millimeter wave range, i.e. over 100 GHz.

In this chapter, the history and current status of the existing fiber networks is briefly given, opto-electronic integrated devices are introduced and the role of Electro-Optic (EO) modulators is presented.

1.1 Optical Communication

The invention of the laser in the early 1960's offered [1], for the first time, an appropriate light source for optical transfer of large amounts of data over long distances. Semiconductor lasers, especially, proved to be very suitable for this purpose due to their compactness, reliability, and potential for monolithic integration with other passive and active optical and electronic devices. Such a communication system still lacked an efficient medium of transmission. Optical fiber loss was in the order of 1000 dB/km around 1965. The appearance of optical fiber with loss of 20 dB/km in 1970 offered a preferred medium for high-throughput point-to-point optical communications [2]. The primary advantages of optical fiber are its large bandwidth, low attenuation, immunity to interference, and high security. Since then, the attenuation of optical fibers has been drastically reduced by at least a few order of magnitudes down to the theoretical limit of 0.2 dB/km.

There have been four distinct generations of fiber optic transmission systems; each new generation overcoming the limitations of its predecessor [3]-[6]. The first generation, deployed in the 1970's, uses multimode fibers at wavelengths near 850 nm [7]. Second generation systems, introduced in 1980's, avoid chromatic dispersion by operating at 1300 nm but still uses multimode fibers [8]. Third and forth generations of optical communication systems use single mode fiber at 1300 nm and 1550 nm wavelength ranges, respectively. The advent of the erbium doped fiber amplifier (EDFA) and optical loss near the theoretical limit in the 1550 nm range made this window the wavelength range of choice for medium and long haul optical communications. With the introduction of EDFA, the need for amplification via the electrical domain vanished and all-optical, long distance transportation has become feasible. However, there is still a significant amount of chromatic dispersion at 1550 nm, and low chirp single mode DFB lasers and modulators are still a requirement for high speed transmission systems.

Another property of optical fibers is their capability to transmit several different wavelengths simultaneously. This technique, called wavelength division multiplexing

(WDM) is getting tremendous attention because it can easily increase the capacity of the existing optical networks. Although WDM has offered the possibility of exploiting the large bandwidth in the 1500 nm wavelength range, the EDFA's bandwidth and the minimum channel separation are major limiting factors. Several high throughput WDM systems have been demonstrated to carry information over standard single mode fiber (SMF). Some researchers have chosen dense channel spacing and demonstrated a successful experiment of 60 5.3 Gbit/s WDM transmission over 1650 km of SMF [9]. Other researchers have increased the capacity of a single channel to 40 Gbit/s and demonstrated a 160 Gbit/s WDM transmission using a four-channel wide spaced multiplexed signal [10]. There certainly is a trade-off between the number of channels and operating speed of each channel with respect to the system capacity, optical and electrical crosstalk between channels, cost and performance of the overall system. At this moment, increasing the bit rate of each channel is still a viable option to enhance the capacity of the system. Presently, WDM systems at a channel speed of 10 Gbit/s are commercially available.

1.2 Opto-Electronic Integrated Devices

The need for high-speed optical communication systems has increased the need for the development of electronic, photonic, and opto-electronic components capable of operating at very high frequency. These devices generate, modulate, route, and process optical signals in a fiber-optic communication system. Optical circuits consisting of laser sources, modulators, routers, de/multiplexers and so on are either hybrid or monolithic. Hybrid optical integrated circuits consist of two or more substrate materials and have the advantage of utilizing the best material for each component with the existing process techniques. Severe integration problems in the packaging, compactness, and high cost are the main disadvantages. Monolithic optical integrated circuits use only a single substrate material that makes them suitable for mass production, but they suffer from a more complicated processing technology. Presently, it seems that for small numbers of devices,

hybrid integration is more beneficial and cost-effective than monolithic integration. It is expected that as more advanced, higher-yield processing techniques are developed, the advantages of monolithic integration will make it the technology of choice. Considerable progress has been made in the growth and fabrication of III-IV compound semiconductors. The development of growth processes such as Metal-Organic Chemical Vapor Deposition (MOCVD) and Molecular Beam Epitaxy (MBE) have considerably increased the quality of semiconductor wafers necessary for the fabrication of the optoelectronic devices [11]-[12]. The most promising substrate material for monolithic integration is III-V semiconductor InP. The main benefit of these materials is that their bandgap wavelengths can be tuned to the optical communication window at 1.55 μm. With the overlay of ternary and quaternary compounds of InP epitaxial layers, it is possible to integrate lasers, modulators, detectors, and other passive and active optical and electronic components on the same substrate.

It seems likely that serious technological improvements in the production process of opto-electronic integrated devices will only take place once the necessity for a high-speed optical network is recognized. An increment of consumer demand for broad bandwidth services and an increase in market competition may hasten that recognition. The next paragraph describes one of the key components of an optical communication system: electro-optic modulators.

1.3 Electro-Optic Modulators

There are basically two ways to carry the electrical information onto an optical signal, direct modulation of the laser or external modulation. Direct modulation of the laser has the advantage of transmitter simplicity and low cost, but carries with it some disadvantages, such as frequency chirping and modulation bandwidth limitation. The frequency chirping due to direct modulation of laser increases the spectral content of the optical signal. The chromatic dispersion of already installed standard single mode fiber severely limits the transmission span and spectral content (bit rate) of the optical signal

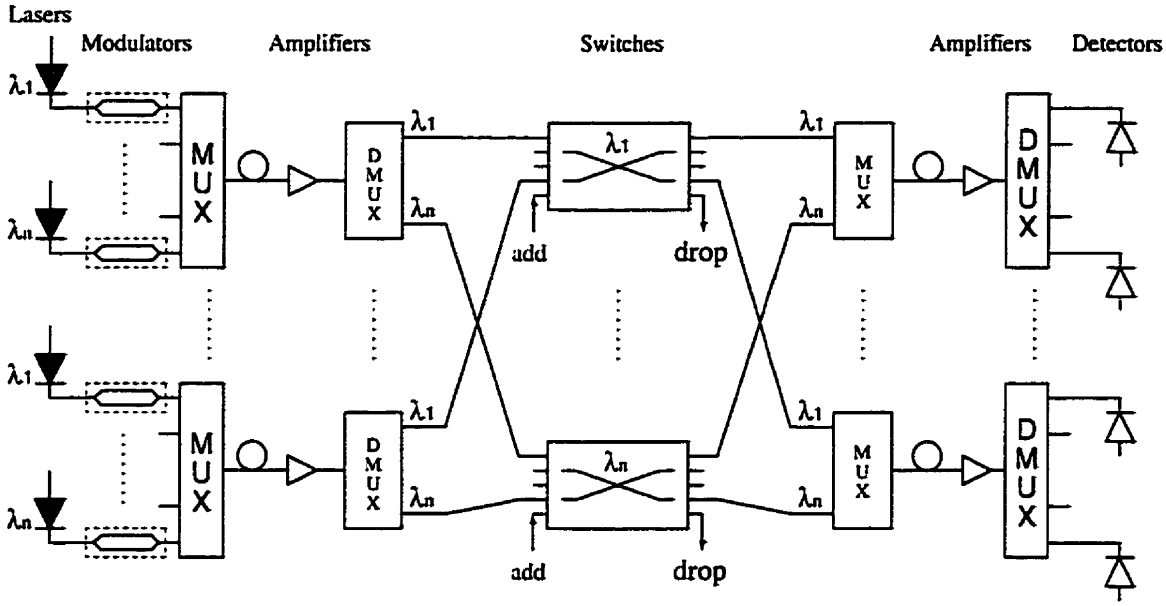

Figure 1.1 Schematic diagram of a typical optical communication network showing different components such as modulators and switches.

for a given bit error ratio (BER) [13]-[14]. Semiconductor lasers also demonstrate an inherent limited frequency bandwidth. The present frequency limit for direct laser modulation is at almost 30 GHz [15]-[16]. This approach is presently being employed for optical communication systems operating at 2.5 Gbit/s (OC48) or less. These limitations on the network performance of directly modulated lasers have motivated additional development of high-speed external modulators. These offer larger modulation bandwidth and negative frequency chirp under proper biasing [17]. All OC192 (≅ 10 Gbit/s) optical communication systems are using external modulators to modulate the optical signals. The schematic diagram of a high-speed optical communication network is depicted in Figure 1.1. External modulators are necessary components for the next generation of optical communication system operating at 40 Gbit/s and higher. These devices are capable of modulating an optical signal at frequencies well into the millimeter-wave range (≈100 GHz). An external laser modulator can be described as a device, separate from the laser, which uses an electric field or current to change the phase, amplitude, or intensity of the optical signal by changing the absorption coefficient or the refractive index of the medium in which the laser signal propagates.

There are two significantly different kinds of external modulators. These are the electroabsorptive devices (current devices) [18] and electro-optic devices (electric field devices) [19]. The electroabsorption modulator is basically an absorption device that attenuates the laser light passing through the component. In order to achieve modulation of laser light by absorption, a number of physical phenomena have been utilized, such as Quantum Confined Stark Effect in quantum wells [18] as well as waveguide or thin film structure bulk crystals [20]. In this type of modulator, an applied electric field causes a shift in the semiconductor bandgap. This results in a change in the optical absorption at a given wavelength. Invoking the Kramers-Kronig relations [21], which relates the real part of the refractive index to the its imaginary part, we know that any change in the imaginary part must lead to a change in the real part. Thus, the electro-absorption effect must be accompanied by an electro-optic effect. This undesired electro-optic effect leads to a spurious phase modulation in the output of MQW intensity modulators, an effect very similar to the phenomenon of chirp in directly modulated lasers. The Quantum Confined Stark Effect offers large changes in the real and imaginary parts of the refractive index in the wavelength range near its band gap region. Thus, multiple-quantum-well (MQW) electroabsorption modulators are mainly operating in that range and therefore suffer from frequency chirping and high insertion loss. These modulators are also expected to offer low modulation voltages due to the large electroabsorption effect (Quantum Confined Stark Effect). As mentioned earlier, in MQW structures, a large electroabsorption effect is accompanied by a large electro-refractive effect. This property of MQW structures has been used by a number of researchers to develop phase modulators and Mach-Zehnder intensity modulators [22]-[23]. Again, these devices offer very low modulation voltages and compact sizes suitable for integration with laser sources. The limited modulation bandwidth and high frequency chirping of these devices are still to be studied.

Electro-optic modulators are based on Pockels effect. F. Pockels established the theory of linear electro-optic effect and characterized this effect for several crystals [24]. The linear electro-optic (Pockels) effect provides a change in refractive index linearly proportional to the applied electric field. This index change results in phase retardation of

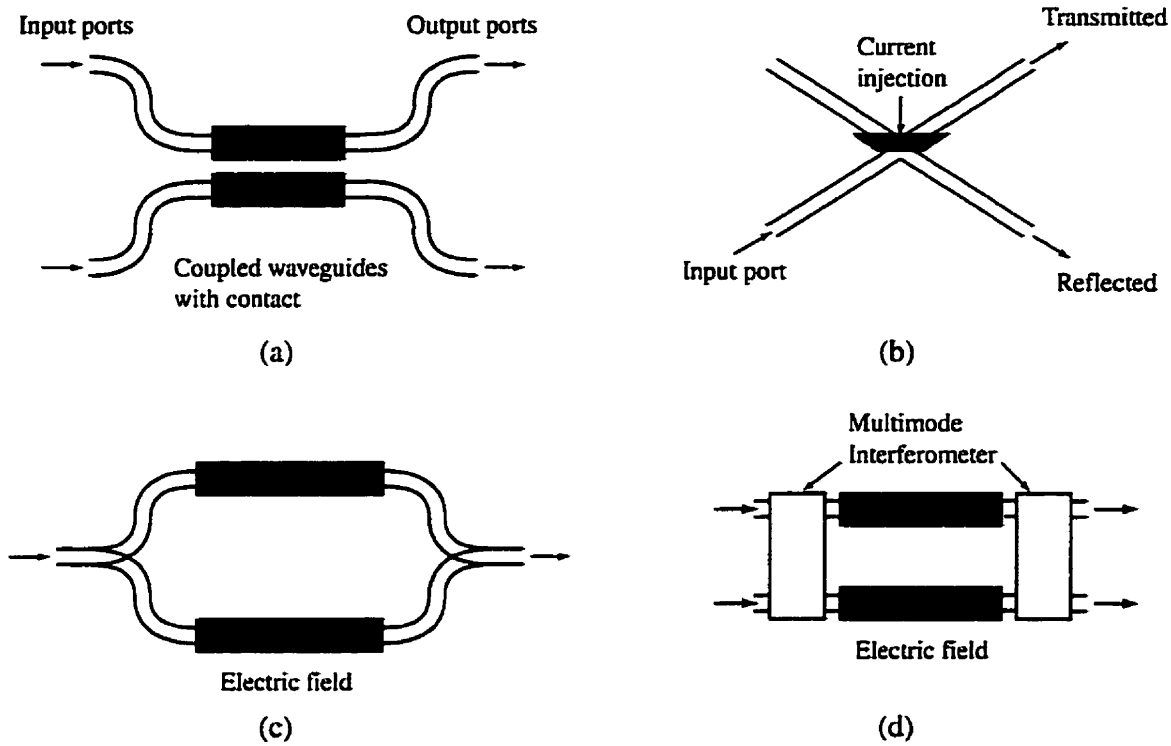

Figure 1.2. Schematic layout of a) a directional coupler electro-optic switch, b) a Total internal reflection switch (modulator), c) an electro-optic Mach-Zehnder modulator, and d) a 2x2 multimode interferometer (MMI) switch.

the optical signal. This will be the subject of the next chapter. Electro-optic modulators offer the advantages of simplicity and ease of fabrications. These modulators were first developed on lithium niobate ($LiNbO_3$) and gallium arsenide (GaAs) substrates. However, due to poor material quality in GaAs resulting in excessive insertion loss, the material of choice was lithium niobate ($LiNbO_3$). The modulators and switch technologies in lithium niobate have progressed to Mach-Zehnder and directional couplers with bandwidth in excess of 40 GHz [25]. The electro-optic effect of some other crystals such as ADP ($NH_4H_2PO_4$), KDP (KH_2PO_4), and lithium titalate ($LiTaO_3$) have also been studied [26]-[27]. Some of the most common structures for external modulators and switches are given in Figure 1.2. Each switch can be employed as a modulator with an additional capability of routing the signal. As shown in this figure, the basic operation of optical modulators and switches are identical. Figure 1.2a illustrates a directional coupler that exploits the electro-optic effect to change the propagation constant difference of the coupled waveguides [28]-[29]. The optical signal can be switched to either output.

A Total Internal Reflection (TIR) switch, Figure 1.2b, uses current injection to reduce the refractive index and therefore direct the optical signal to the opposite waveguide [30]. This device reflects only the optical signal coming from the bottommost input waveguide to the bottommost output waveguide. It operates as a waveguide crossing if there is no injected current. Mach-Zehnder intensity modulators, given in Figure 1.2c, are well known and use either electro-optic effect or electro-refractive effect to induce a π radian phase shift between the two optical signals traveling down the two arms of the modulators. This causes a destructive interference at the output Y-junction. Mach-Zehnder intensity modulators are the subject of this thesis and will be discussed in the next chapter. Replacing the Y-junctions at the input and output of the Mach-Zehnder modulators with Multimode interferometers (MMI) enables the device to operate as a 2x2 switch, as shown in Figure 1.2d [31]-[32].

The bandwidth of electro-optic modulators depends upon the electrode types and geometry, and the substrate dielectric constant. There are two types of electrodes used with waveguide modulators, lumped and traveling wave. An electrode is a lumped element when its length is small compared to the wavelength of the microwave signal on the electrode. In this case, the modulation bandwidth is mostly limited by the time constant of the lumped electrode [33]. There is a possibility of reducing the electrode size and increasing the device bandwidth at the expense of increasing the modulation voltage. Traveling wave electrodes, on the other hand, can offer wider modulation bandwidths. This is achieved by matching the phase velocity of the microwave signal to the group velocity of the optical signal. Consequently, the optical signal propagating through the optical waveguide always experiences the same electric field along every point of the electrode [34]. The velocity match condition is one of the most important criteria for achieving wide bandwidth, low modulation power, and high modulation depth [33]. Velocity mismatch may be due to either the leading or lagging of the microwave phase velocity on the electrodes with respect to the group velocity of the optical signal. For example, the phase velocity of the microwave signal moving along the coplanar electrodes on $LiNbO_3$ substrate is less than the velocity of the optical signal in the optical waveguide [35]. Therefore, to match the velocity of optical and microwave signals, the

modulating signal has to be sped up. These electrodes are called fast wave electrodes. Researchers have modified the conventional coplanar strip to increase the phase velocity of microwave signal on planar electrodes on $LiNbO_3$ substrates [36]-[38]. In the III-V compound semi-conductors, the modulating microwave signal travels faster on the electrodes than the optical signal. To achieve a velocity matched condition, the phase velocity of the microwave signal is reduced to match that of the optical signal, hence, employing slow-wave electrodes.

Two major slow-wave electrode configurations for GaAs electro-optic traveling wave modulators have been reported [19]. These are the microstrip configurations defined on *p-i-n* epitaxial semiconductor layer structures [39] and the coplanar strip configuration using undoped semiconductor epitaxial layers, all grown on semi-insulating semiconductor substrates [40]. These *p-i-n* modulators are normally fabricated on n^+ GaAs substrates. The microstrip transmission line is dispersive and the microwave loss is high due to the propagation of slow-wave and skin effect modes [42]-[43]. The overlap factor between the optical and microwave fields [33] in *p-i-n* modulators is close to 100%. A new structure, called planar microstrip (PMS), was proposed for the *p-i-n* velocity-matched traveling wave electro-optic modulator [41]. This is a slight modification to the conventional *p-i-n* structure and consists of a series of doped layers, n^--*i*-*n*-n^+ , grown on a semi-insulating GaAs substrate. In this design the ground plane is sitting on top of the n^+ layer as opposed to the bottom of the substrate in the conventional *p-i-n* modulators. This design significantly reduces the microwave dispersion and improves the velocity matching while maintaining the high overlap factor between the optical and microwave signals. This structure still demonstrates higher microwave insertion loss. Similar structures have been used in the development of traveling wave photodetectors [44]-[45].

Several slow wave electrode structures including metal-insulator-semiconductor (MIS) structures [46], Schottky contact structures [47], and coplanar waveguide structures, which use periodically doped semiconductor substrates [48], have been reported. Due to the inherent lossy nature of doped semiconductor materials, these slow wave electrode structures are unable to operate at a high modulation frequency.

Several velocity-matched modulators employing coplanar electrodes on undoped substrates have been reported. Alferness *et al.* have come up with a velocity matching technique by periodic phase reversal [49]. In this approach, the electrode is laterally shifted after an interaction length, so that the direction of the applied electric field in the waveguide is reversed. One potential drawback on device operation is the performance degradation caused by reflection occurring at the abrupt 90°-corners of the electrodes. Periodically loading two conductor coplanar strip waveguides (signal-ground, S-G) with capacitive elements such as narrow fins to achieve velocity match condition has been implemented by Jaeger *et al.* [50]. Although these electrodes have the potential of slowing the microwave signal, they will either require a high modulation voltage or result in a limited bandwidth due to the microwave insertion loss. Spickermann *et al.* have published several papers that are based on three conductor coplanar waveguides (ground-signal-ground, G-S-G) [51]-[54]. They have studied two different slow wave coplanar structures in which the slowing of the microwave signal is achieved by periodically loading the lines with narrow fins and pads. A small-signal modulation bandwidth of 40 GHz for both electrode configurations was measured. The measured half-wave voltage, the voltage required to induce a π phase shift between the two arms, was over 30 V for polarization sensitive and polarization insensitive modulators. The above-mentioned half-wave voltages are too large to be effectively utilized in a practical modulator especially for high frequency modulation. The publication of these results was concurrent with the design of the first mask and fabrication performed for this research thesis.

The carrier concentration of the substrate is an important variable in determining the performance of electro-optic modulators. High carrier concentration in the substrate causes high microwave loss and dispersion [19]. The common factor that ties together the demonstration of slow wave modulators in [40] and [53] and previous work referred to therein, is the fact that semiconducting heterostructures defining the optical waveguide were unintentionally doped. It is widely understood that unintentional doping can mean a broad range of residual carrier concentrations between 1×10^{14} cm^{-3} and 5×10^{16} cm^{-3}, depending upon the epitaxial material and growth technique used. As will be explained in the next chapter, linear electro-optic modulators are strictly electric field devices. The

interaction between the applied electric field and the crystallographic structure creates a linear change in the refractive index of the material (Pockels effect). Free carrier transport does not play any role in the operation of these devices, other than increasing the microwave loss and dispersion in traveling wave modulators. To the best of this author's knowledge, no study has been performed to establish a relation between the substrate carrier concentration and microwave electrode loss for electro-optic modulation applications. It was therefore necessary to investigate the threshold in carrier concentration of the substrate and the epitaxially grown layers which permit an acceptable level of microwave insertion loss while not imposing stringent practical limitations on growth techniques and cost.

In order to improve the performance of electro-optic modulators, it is necessary that the overlap factor between the microwave signal and optical signal be maximized. Some researchers have investigated the effects of interelectrode gap geometry, optical mode size and position, and overlap factor on the optical signal phase retardation [33], [55]-[56]. These studies were done only using uniform coplanar strips or coplanar waveguides, where the electric field in the propagation direction is considered constant. In periodically loaded coplanar slow wave structures, however, the electric field is not uniform in any direction, including the propagation direction. The microwave electrodes and optical waveguide structure and their relative position have to be designed in a way to maximize the transversal and longitudinal overlap factor between the optical and electrical signals.

1.4 Thesis Outline

The main goal of this research program is the design, development, characterization, and optimization of III-V traveling wave electro-optic modulators. The work is mainly experimental, but there is some modeling and simulation throughout the work. Some novel slow wave electrodes are proposed and demonstrated which enhance the overall performance of the electro-optic modulator. These slow wave electrodes are

fabricated on semi-insulating gallium arsenide (SI-GaAs) and semi-insulating indium phosphide (SI-InP). Microwave performances of the slow wave electrodes were investigated and the results were used for the design of new structures. The slow wave electrodes are integrated with different optical structures such as MZ interferometers or straight waveguides to realize different types of modulators. Electro-optic modulators are in the forms of mode converters and Mach-Zehnder intensity modulators. These modulators were fabricated on GaAs and InP based materials. The study on the performance of electro-optic modulators on InP materials is important when used for integration of the modulator with the laser. Modulators were characterized by measuring their characteristic transfer function, half-wave voltage, small-signal modulation bandwidth, and large-signal modulation. As for material characterization, a study was performed on the relation between substrate carrier concentration and microwave loss of slow wave electrodes. The results helped us to determine an upper limit on the substrate doping level suitable for electro-optic modulation applications.

The performance of slow wave electro-optic modulators depends upon several parameters such as interelectrode gap, device length, and the overlap between the optical and electrical fields. The relationship between these parameters was investigated using simulation of modulators with different electrode geometries and optical waveguide structures. The goal here is to establish some engineering design rules and to optimize design and performance parameters.

Chapter 2 **Theory of Electro-Optic Modulation**

In the first part of this chapter, the basic theory of linear electro-optic modulation (Pockels effect) in III-V semiconductor materials is presented. This is followed by the analysis of different types of modulation including phase modulation and mode conversion. Mach-Zehnder interferometers (MZI) are utilized to exploit these modulations for intensity modulation applications. Simulation results are obtained for Mach-Zehnder modulators under different bias configurations. A brief analysis of frequency chirp inherent to Mach-Zehnder modulators is presented.

Chapter 3 **Design of Traveling Wave Electro-Optic Modulators**

Design considerations and criteria for the development of semiconductor traveling wave electro-optic modulators are discussed in this chapter. Different heterostructure epitaxial layers used in the fabrication of modulators are presented. A novel technique is proposed which reduces the thickness of the cladding layer by inserting a thin layer of high refractive index AlAs in the cladding layer. The design of traveling wave electrodes to be integrated with optical structures such as the MZI is given. Geometrical dimensions and layout of the electrodes and optical structures are presented in Appendix I and II.

Chapter 4 **Characterization, Fabrication and Measurement Techniques**

The processing and fabrication aspects of traveling wave electro-optic modulators including the characterization and processing of AlGaAs wafers are given. Measurement techniques for optical losses through the semiconductor ridge waveguides using Fabry-Perot and cutback techniques are presented. Finally, the measurement techniques for low frequency transfer functions and high frequency responses are described.

Chapter 5 **Measurement Results**

This chapter presents the optical, electrical and electro-optical measurement results for different electro-optical modulators. It includes the characterization results of semi-insulating GaAs and epitaxially grown AlGaAs wafers. This chapter also contains the detailed study of the effect of substrate free carriers on the microwave insertion loss. The performances of polarization sensitive and insensitive MZ modulators as well as polarization converters are presented. Also included are values for half-wave voltage, on-off extinction ratio, and modulation bandwidth.

Chapter 6 **Discussion and Conclusion**

In this final chapter, the measurement results and the performance of the traveling wave electro-optic modulators on GaAs wafers are reviewed and research topics promising further improvements are proposed. Finally, some conclusions are drawn from

the work including the proposal of novel high-speed traveling-wave switches and detectors.

CHAPTER 2

Theory of Electro-Optic Modulation

In this chapter a number of topics fundamental to electro-optic modulation theory are discussed. Of particular interest are those issues which are related to the traveling wave modulator design on semiconductor materials upon which this thesis rests. Where appropriate, only brief summaries of material are provided in order to avoid lengthy expositions of previously published material. Ample references are provided to the textbooks, research journals, and conference proceedings, which comprise the basis for this chapter.

2.1 Electro-Optic Effect

The linear electro-optic effect (Pockels' effect) is utilized in large bandwidth electro-optic modulators. This effect consists of a linear change in refractive index of the crystal by applying an electric field. The birefringence of crystal is expressed in terms of its index ellipsoid as [24]:

$$\frac{x_1^2}{n_1^2}+\frac{x_2^2}{n_2^2}+\frac{x_3^2}{n_3^2}=1 \tag{2.1}$$

where the n_1, n_2, and n_3 are the three principal refractive indices with the crystallographic axes as the optical axes, x_1, x_2, and x_3. In the presence of an electric field, the index ellipsoid is deformed as:

$$\sum_{i,j,k}\left(\frac{1}{n_{ij}^2}+r_{ijk}E_k\right)x_i x_j = 1 \tag{2.2}$$

where i, j, and k vary from 1 to 3, E_k is the applied electric field component, r_{ijk} is the electro-optic coefficient of the crystal, and $n_{ii}^2 = \varepsilon_{ii} = n_i^2$.

GaAs and InP and their ternary and quaternary alloys are optically isotropic and belong to the $\bar{4}3m$ zincblende crystal symmetry group [57]-[58]. In this class of crystals, Equation (2.1) is reduced to

$$\frac{x_1^2+x_2^2+x_3^2}{n_0^2} = 1 \tag{2.3}$$

where $n_1 = n_2 = n_3 = n_o$. The only nontrivial electro-optic coefficients are the r_{41} elements. The electro-optic tensor is expressed as:

$$r_{ij} = \begin{pmatrix} 0 & 0 & 0 \\ 0 & 0 & 0 \\ 0 & 0 & 0 \\ r_{41} & 0 & 0 \\ 0 & r_{41} & 0 \\ 0 & 0 & r_{41} \end{pmatrix} \tag{2.4}$$

$r_{41} \approx 1.4\times10^{-4}$ m/V in GaAs and InP. If an arbitrary electric field is applied to the crystal, the index ellipsoid of Equation (2.2) becomes [57]:

$$\frac{x^2+y^2+z^2}{n_0^2}+2r_{41}\left(E_x yz+E_y zx+E_z xy\right)=1 \tag{2.5}$$

where $x = x_1$, $y = x_2$, and $z = x_3$. GaAs and InP substrates are normally grown in the [100] crystal plane. For this type of crystal, two orientations are considered, a) the applied electric field, E_{rf} is applied along the [100] direction and b) the applied electric field, E_{rf} is along [011]. In both cases the light propagates in the $[0\bar{1}1]$. The two orientations are shown in Figure 2.1 and Figure 2.2, respectively. These are convenient orientations since

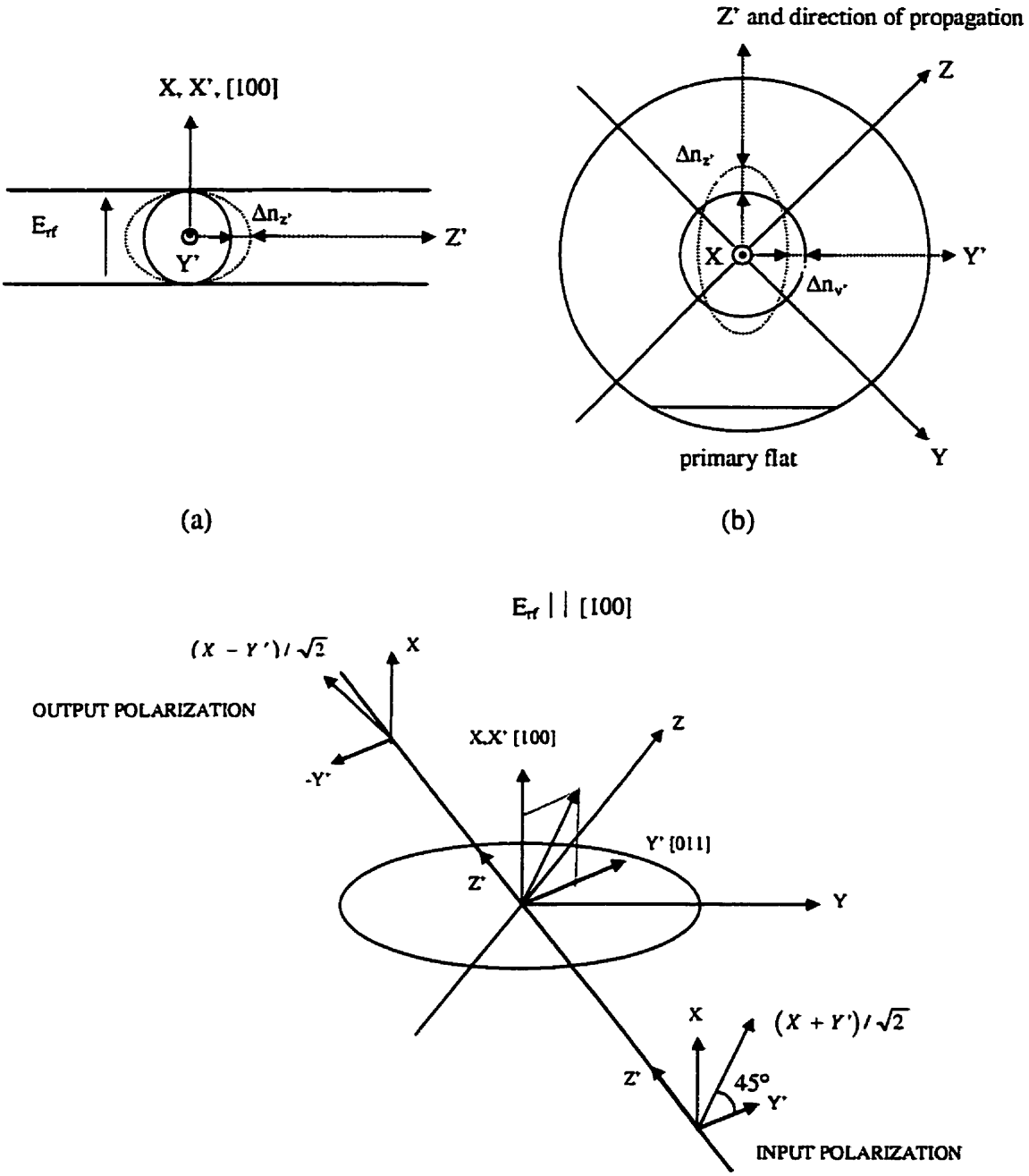

Figure 2.1 Index ellipsoid and polarization transformation in a zincblende crystal family for the electric field, E_{rf}, in the [100] direction and lightwave propagating in the $[0\bar{1}1]$ direction. (a) transversal view of the index ellipsoid deformation. (b) index ellipsoid deformation from wafer top view. (c) polarization modulation.

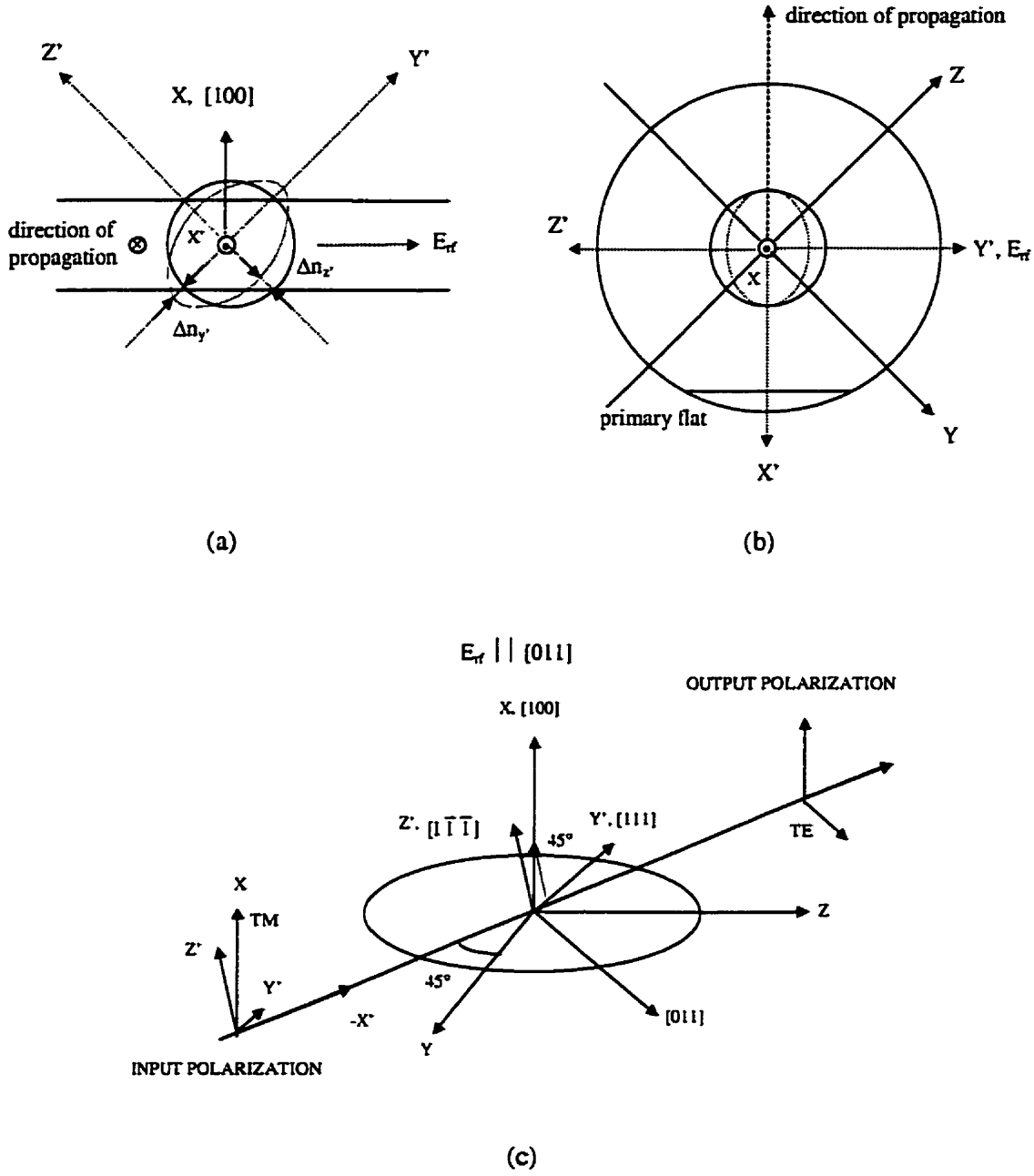

Figure 2.2 Index ellipsoid and polarization transformation in a zincblende crystal family for the electric field, E_{rf}, in the [011] direction and lightwave propagating in the [0 $\bar{1}$ 1] direction. (a) transversal view of the index ellipsoid deformation. (b) index ellipsoid deformation from wafer top view. (c) polarization modulation.

the epitaxial layers are grown on the [100] plane of the GaAs surface for most electronic and photonic devices.

As shown in Figure 2.1, an applied electric field in the [100] direction perturbs the index ellipsoid through the linear electro-optic effect that results in an index ellipsoid with principal axes along the TE and TM polarization directions. This results in a field induced refractive index change in the [011] direction (TE mode). The other axis of the index ellipsoid in the [100] direction (TM mode) is unaffected by the presence of the applied electric field. The indices of refraction along [011] and [100] directions are $n_0 \pm n_0^3 r_{41} E_{rf} / 2$ and n_0. The input polarization of the light propagating in the $[0\bar{1}1]$ direction will have no phase retardation for polarization along [100], a phase modulation for polarization along [011], and a polarization modulation for polarization at 45° to the [011] direction. Therefore, devices that are only based on the linear electro-optic effect and exploit the applied electric field in the [100] direction on [100] flat substrates, are polarization sensitive. These devices only modulate the TE component of the input optical signal. The optical signal phase retardation, $\Delta\varphi$, is expressed as [33],[57]:

$$\Delta\varphi_{[100]} = -\pi n_0^3 r_{41} \frac{V}{G} \frac{L}{\lambda} \Gamma_s \tag{2.6}$$

where λ is the optical signal wavelength, V is the applied voltage, L is the interaction length between the optical and electrical signal (electrode length), G is the space charge width or the electrode gap, and The Γ_s is the transversal overlap factor, between the optical and the microwave signals which is defined as [33]:

$$\Gamma_s = \frac{G}{V} \iint_A E_{rf} \left| E_{opt} \right|^2 dA \tag{2.7}$$

where E_{opt} is the normalized optical electric field and the integration is over the cross section area of the optical mode, A.

The modulation voltage required to achieve π phase shift is called the half-wave voltage, V_π. The half wave voltage length product is thus:

$$V_\pi L = \frac{\lambda G}{n_o^3 r_{41} \Gamma_s} \tag{2.8}$$

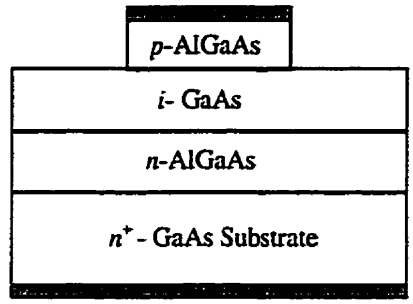

Figure 2.3 Cross section of a *p-i-n* waveguide microstrip configuration modulator on a n^+ [100] flat GaAs substrate with a double heterostructure cladding layer.

For E_{rf} along the [100] direction, two electrode configurations are possible, one is the microstrip configuration using a *p-i-n* structure as shown in Figure 2.3, and the other is a planar strip electrode configuration as shown in Figure 2.4(a). In the former, the metal electrodes are in contact with *p*-layer and the back of the substrate providing the electric field in the [100] direction across the *p-i-n* and Schottky junctions. In the *p-i-n* modulators fabricated on an n^+ substrate, the transmission line is dispersive and microwave loss is high due to interaction between the microwave signal and substrate free carriers. These disadvantages severely limit the application of this structure in the traveling wave electro-optic modulator which is the main purpose of this research thesis. This configuration may be used in lumped electrode optical modulators or switches in which the electrode length is much smaller than the microwave wavelength at the maximum frequency of operation. In such cases the microwave loss and dispersion are not issues.

In the coplanar strip configuration of Figure 2.4(a), the optical guide is a double heterostructure dielectrically loaded structure and the metal electrode crosses over the optical guide. When a voltage is applied between signal and ground electrode a predominantly vertical electric field is created along [100] direction under the inner edge of the signal and electrodes in the ridge optical waveguide region.

However, an applied electric field, E_{rf}, along [011] direction on a [100] flat substrate, creates an index ellipsoid with principal axes along [111] and [$\bar{1}$11] directions, see Figure 2.2. The index ellipsoid is rotated by 45° with respect to the TE and TM states of

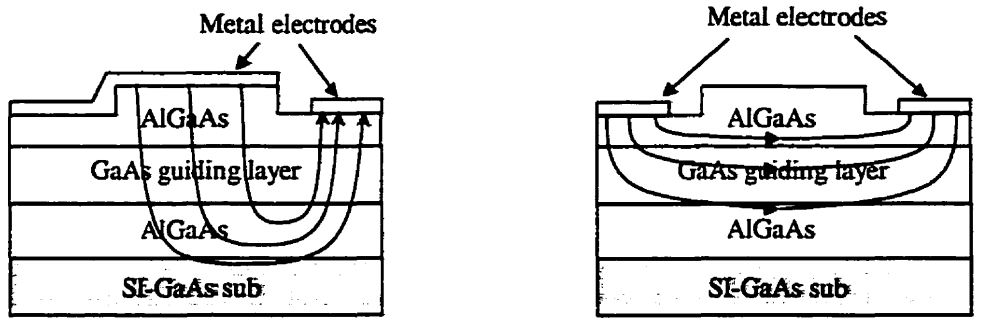

Figure 2.4 Cross section of a double heterostructure waveguide modulator fabricated on a [100] flat SI-GaAs with planar strip electrodes showing the dominant electric field component in the ridge waveguide region. (a) The metal electrode over the ridge waveguide provides the electric field in the [100] direction. (b) The electrodes on either side of the optical waveguide provide the electric field in the [011] direction.

polarization. The refractive indices along [111] and $[\bar{1}11]$ are $n_0 \pm n_0^3 r_{41} E_{rf}/2$ and $n_0 \mp n_0^3 r_{41} E_{rf}/2$, respectively. As light propagates parallel to $[0\bar{1}1]$ with either TE or TM polarization, it will project on both the fast and slow axes of the new index ellipsoid; thus giving a push-pull mode of operation that rotates the polarization state of the input optical signal. The input polarization state is rotated by 90° at the half-wave voltage. In other words, an input TE (TM) mode is converted to output TM (TE) mode at the half-wave voltage.

The phase retardation for light propagating along the $[0\bar{1}1]$ and E_{rf} along [011] is [33],[57]:

$$\Delta\varphi_{[011]} = -2\pi n_0^3 r_{41} \frac{V}{G} \frac{L}{\lambda} \Gamma_s \tag{2.9}$$

with the definition of the terms given above. The phase retardation for this orientation is a factor of two greater than for the former case with E_{rf} | | [011]. This is the optimum orientation for maximum phase retardation per volt.

For E_{rf} along the [011] direction, a coplanar strip electrode configuration can be used with a ridge heterostructure optical waveguide. Electrode are on either side of the optical guide as shown in Figure 2.4(b). This provides a predominantly horizontal electric field in the [011] direction in the ridge waveguide area.

2.2 Intensity Modulation

As discussed earlier, the linear electro-optic effect can be exploited to modulate the phase or the polarization of the input optical signal. Intensity modulation/direct detection is the most attractive modulation/detection scheme in today's optical communication systems. This is due to low cost and simple transmitter and receiver components and circuitry. Therefore, any phase or polarization modulation has to be converted to intensity modulation. In the following, we briefly discuss how to convert them to intensity modulation.

2.2.1 Polarization Conversion

The structure shown in Figure 2.5 schematically illustrates a device that electro-optically converts TE to TM polarization. The cross section view of the device in the optical waveguide region is similar to Figure 2.4(b).

The device uses the only off-diagonal element, r_{41}, of the GaAs or InP electro-optic tensor to convert TE (TM) to TM (TE) polarized light. As explained earlier, the device exploits the predominantly horizontal electric field along the [011] direction in the ridge waveguide region. This polarization or mode conversion can be regarded as coupled wave interaction and coupled mode theory can be used to describe this situation. The Jones matrix of this device can be expressed as [59]-[60]:

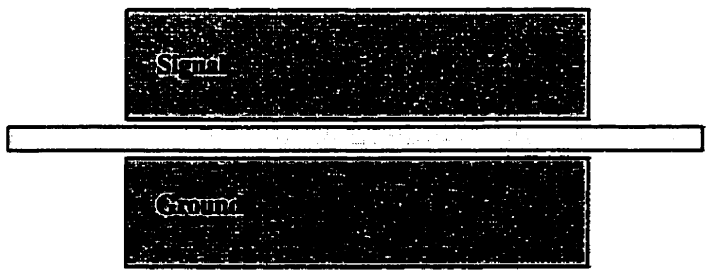

Figure 2.5 Schematic diagram of a polarization/mode converter. The dotted area is the optical waveguide.

$$\begin{pmatrix} A_{TE} \\ A_{TM} \end{pmatrix} = e^{-j\beta z}\begin{pmatrix} h_1 & -jh_2 \\ -jh_2^* & h_1^* \end{pmatrix}\begin{pmatrix} A_{TE}^0 \\ A_{TM}^0 \end{pmatrix} \tag{2.10}$$

$$h_1 = \cos(\beta_b z) + j\frac{\delta}{\beta_b}\sin(\beta_b z) \tag{2.11}$$

$$h_2 = \frac{k}{\beta_b}\sin(\beta_b z) \tag{2.12}$$

where

$$\beta = \frac{\beta_{TM} + \beta_{TE}}{2} \tag{2.13}$$

$$\delta = \frac{\beta_{TM} - \beta_{TE}}{2} \tag{2.14}$$

$$k = \frac{\pi n_0^3 r_{41} E_{rf}}{\lambda} \tag{2.15}$$

$$\beta_b = \sqrt{k^2 + \delta^2} \tag{2.16}$$

A_{TE}, A_{TM} are TE and TM components of the optical field at distance z, A_{TE}^0 and A_{TM}^0 are the input TE and TM components. These equations are used to calculate the transfer function of the device under different conditions. Although the device operates as a polarization/mode converter, it can be used as an intensity modulator. An analyzer has to be used at the output to transform the mode conversion into intensity modulation. For the sake of discussion, let's suppose that the analyzer at the output of the device is set to pass the TM polarization state. Figure 2.6 shows a typical transfer function of the device in the ideal case of zero modal birefringence optical waveguide, $\Delta\beta = 0$. As shown in this figure, the device completely transfers the power between the two modes even at low bias voltage. As one would expect, the operation of this device as an intensity modulator is highly polarization sensitive. In fact, the transfer functions with TE and TM input polarizations are complementary. The polarization problem can be solved by several methods. The easiest approach is to place a polarizer between the input fiber and the device to eliminate one of the polarization states. As the polarization state of the output

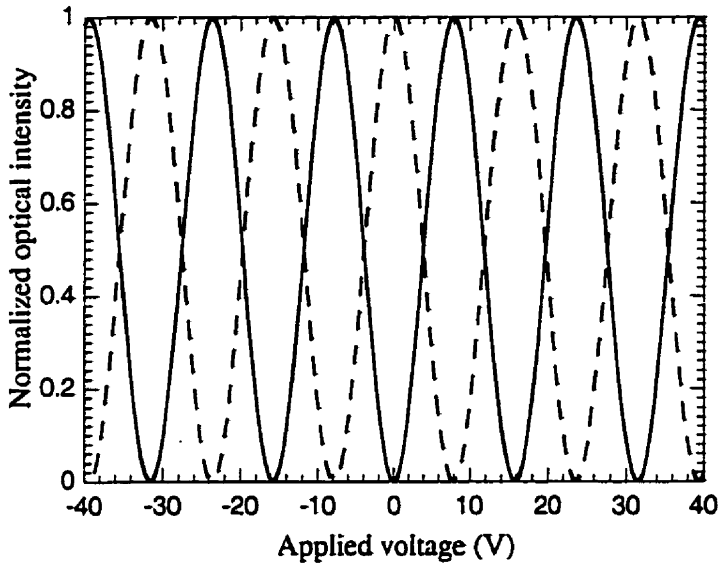

Figure 2.6 A typical transfer function of a mode converter with zero birefringence optical waveguide for input TE (solid) and TM (dashed) polarized signal. Output analyzer is parallel to TM polarization state.

light of the fiber varies with time in a random process, this leads to an optical loss of about 3 dB. A polatization controller may also be placed in front of the device. Both techniques result in higher optical loss, higher cost, and complexity in the integration with a laser source.

The performance of this device is strongly dependent upon the modal birefringence of the optical waveguide, $\Delta\beta = \beta_{TM}-\beta_{TE}$ or $\Delta n = n_{TM}-n_{TE}$. A small increase in the modal birefringence of the optical waveguide significantly degrades the performance of a mode converter. The transfer functions of a mode converter with non-zero modal birefringence optical waveguides are given in Figure 2.7. All parameters except Δn are the same as the device whose transfer function is shown in Figure 2.6.

It is clear that even a small modal birefringence of as low as 1×10^{-4} 1) reduces the power conversion between the TE and TM modes, 2) increases the half wave voltage of the device particularly at low bias voltage, and 3) significantly increases the bias voltage to obtain high modulation efficiency. For example, to achieve a modulation efficiency over 80%, the mode converter with $\Delta n= 1\times10^{-4}$ has to be biased over 30 V.

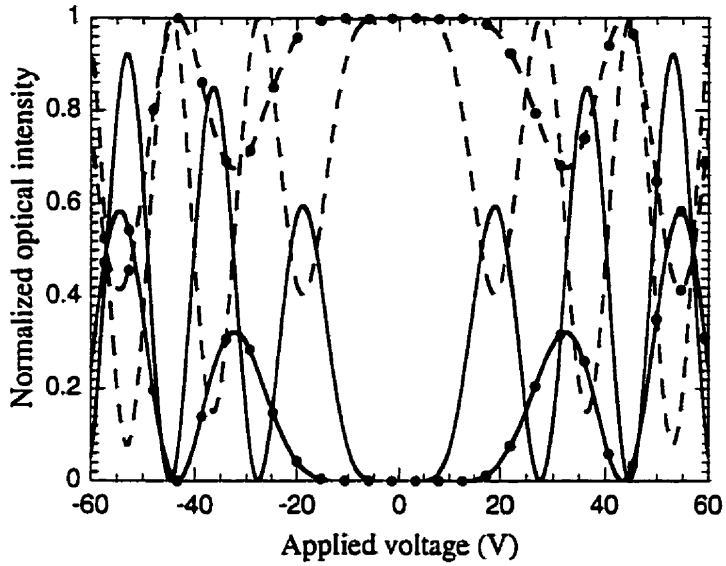

Figure 2.7 The transfer function of a mode converter with non-zero birefringence optical waveguide for input TE (solid) and TM (dashed) polarized optical signals and for $\Delta n = 1\times10^{-4}$ and $\Delta n = 3\times10^{-4}$ (circled). Output analyzer is parallel to TM polarization state.

The two polarized modes of the optical waveguides in a waveguide device in general have different propagation constants and may also suffer from different losses. Polarization dependence optical waveguide is a particularly serious problem in devices such as phasars whose operation relies on some form of phase matching as phase matching can not be easily satisfied simultaneously for two modes with different propagation constants. In a zero modal birefringence optical waveguide, the propagation constants of TE and TM modes are the same. In a polarization independent optical waveguide, the TE and TM modes see the same refractive index discontinuity across the structure. The birefringence in an optical waveguide can be eliminated by controlling the aspect ratio of the core of the waveguide. The idea has been applied in different types of optical waveguide such as buried waveguides, strip and rib waveguides.

2.2.2 Mach-Zehnder Intensity Modulators

In this section, different ways to accomplish intensity modulation are discussed. It is well known that a Mach-Zehnder optical interferometer (MZI) integrated with phase

Figure 2.8 Schematic diagram of a MZ modulator with phase modulation on each arm of the interferometer.

modulation on each arm will function as an intensity modulator. We will also show that a MZI can be employed to transform polarization/mode conversion to intensity modulation. Figure 2.8 shows a MZI integrated with a simple coplanar waveguide (CPW). A simple coplanar strip can also be used as the RF electrode. Each arm of the MZI is a phase modulator. We will use PM-MZI intensity modulator to refer to this type of device in the rest of this thesis. In this case, the two arms of MZI are placed under the inner edge of signal and ground electrodes. The cross section of the device in the optical waveguide area, relative position of the RF electrode to optical waveguide, and the induced electric field are illustrated in Figure 2.4(a). The phase modulation in each arm of this device is governed by the Equation 2.6. An input optical signal is equally divided at the Y-junction into two arms of MZI. In the absence of an applied voltage, the optical path length of the two arms of MZI remains the same and the two signals are then constructively added at the output Y junction. However, when the half wave voltage is applied to the center electrode, the optical path length difference between the two arms of MZI creates π phase shift between the two signals. This in fact excites the second-order mode at the output Y-junction and the signal is radiated into the substrate. This Figure also shows that the device operates in a push-pull fashion and therefore reduces the half-wave voltage by a factor of two. The characteristic function of such an intensity modulator can be expressed as:

$$I_{out} = I_{in} \cos^2(\varphi_{ind} + \Delta\varphi_{const}) \tag{2.17}$$

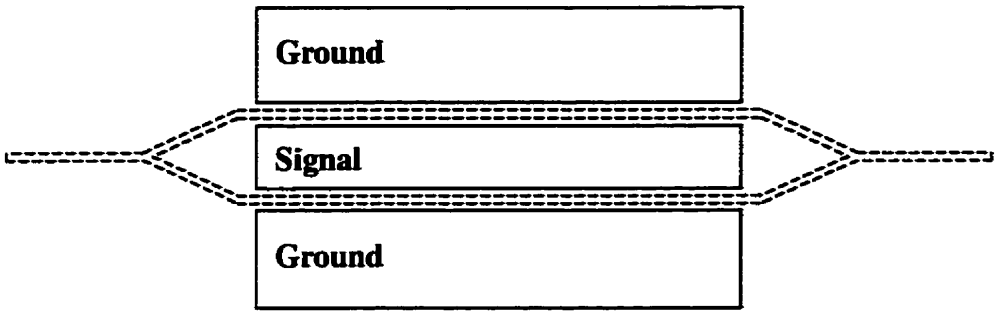

Figure 2.9 Schematic diagram of a MZ modulator with mode conversion on each arm of the interferometer.

where I_{out} and I_{in} are the output and input light intensity, respectively, φ_{ind} is the electric field induced phase-change on each arm of the MZI, and $\Delta\varphi_{const}$ is the optical phase difference between the two arms. This device can be operated at zero bias voltage by intentionally creating a 45° optical phase difference between the two arms of MZI. As discussed earlier, this device modulates only the phase of TE component of the input optical signal and the TM component will not be affected by the electric field. This results in a polarization sensitive modulator.

Figure 2.9 illustrates a schematic diagram of a polarization independent modulator. The cross section of the device in the optical waveguide area, relative position of the RF electrode to optical waveguide, and the induced electric field are illustrated in Figure 2.4(b). It consists of a MZI integrated with a CPW. Each arm of the device operates as a polarization/mode converter. This type of device will be referred to as MC-MZI intensity modulator. Equations given in the last section can be used to accurately analyze the device. However, a simple explanation for the operation of this device is as follows: an input optical signal with an arbitrary polarization state is divided at the input Y junction. By applying the RF signal to the centre electrode a push-pull electric field is created in the optical waveguide region. This rotates the polarization of the optical signal in each arm in opposite direction by 90°. At the output Y-junction the two signals are combined and they cancel each other. This polarization insensitive electro-optic modulator can be operated in the following biasing configurations:

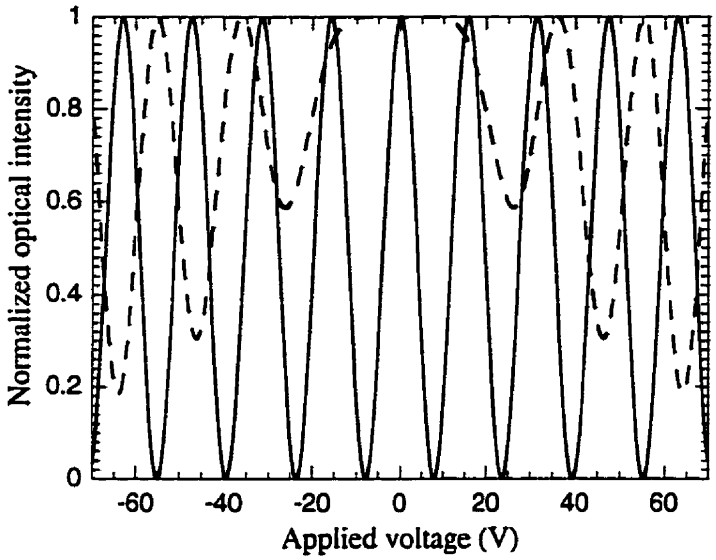

Figure 2.10 Transfer function of a polarization independent MC-MZI intensity modulator for input TE and TM polarized signals with optical waveguide modal birefringence of $\Delta n = 0$ (solid) and $\Delta n = 2\times10^{-4}$ (dashed). The DC and RF signals are applied to the centre electrode.

1. The RF and bias signals are applied to the centre electrode and the two side electrodes are grounded. In this case the DC and RF electric fields are both in the same direction in the optical waveguide regions in each waveguide. Figure 2.10 gives a typical transfer function of an MC-MZI intensity modulator under this biasing configuration for both TE and TM input polarizations with optical waveguide modal birefringence, Δn, as parameter. This graph again emphasizes the importance of zero birefringence optical waveguides to be used in the polarization/mode converter on which this device is based. A small increase in $\Delta\beta$ significantly reduces the on-off extinction ratio at low bias voltage. This configuration provides a polarization insensitive modulation with relatively high on-off extinction ratio at high bias voltage. Optical path length difference between the two arms of a MZI is due to any asymmetry in the long structure that is very difficult to control. For example an optical path phase difference, $\Delta\varphi_{const}$, of 90° at the wavelength of 1.55 μm on a GaAs/AlGaAs optical structure is equal to 0.47 μm in optical path length difference. Since these devices are relatively long , ≥1 cm, this can happen due to nonuniformity in the optical structure across the wafer, nonuniform etching along the device, errors during mask

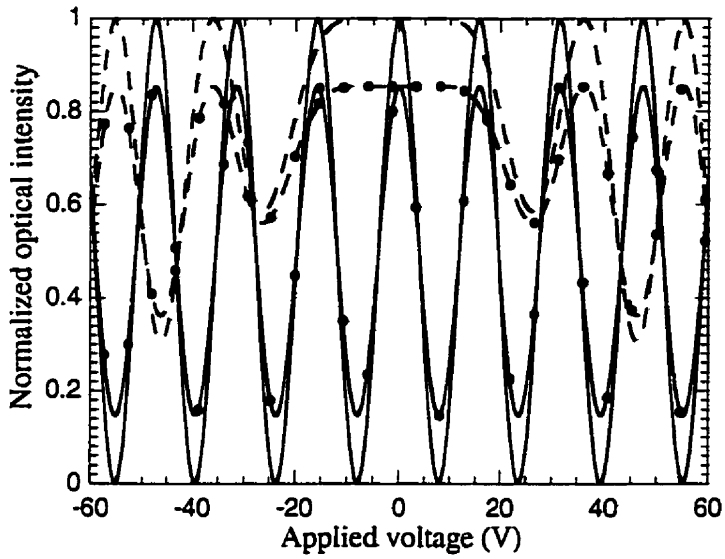

Figure 2.11 Transfer function of a polarization independent MC-MZI intensity modulator for input TE and TM polarized signals with optical waveguide modal birefringence of $\Delta n = 0$ (solid) and $\Delta n = 2\times10^{-4}$ (dashed) and for optical phase difference of $\Delta\varphi_{const} = 0$ (non-marked) and $\Delta\varphi_{const} = 90°$ (circled). The DC and RF signals are applied to the centre electrode.

fabrications, and so on. Therefore the effect of such asymmetry in the MZI has to be considered. Figure 2.11 shows the transfer function of an MC_MZI intensity modulator for different optical path phase differences and different modal birefringence values in optical waveguide for both states of polarization, TE and TM modes. Although any optical path length difference between the two arms of the MZI causes a decrease in the on-off extinction ratio, the device still maintains its polarization independence. For $\Delta\varphi_{const} = 90°$, the extinction ratio reduces to 0 dB; in other words, there is no modulation. The problem is less severe if the ridge optical waveguide is designed to be polarization insensitive.

2. In the second biasing configuration, the RF and DC bias signals are applied to the centre electrode and one of the side electrodes is also biased above ground. The other side electrode is grounded. The maximum bias point of the side electrode is limited by the electric field breakdown of the substrate. The transfer function of a device under this biasing configuration is given in Figure 2.12. In this calculations, it was assumed that $\Delta\varphi_{const} = 0$ and $\Delta n = 2\times10^{-4}$. As seen the on-off extinction ratio and half-

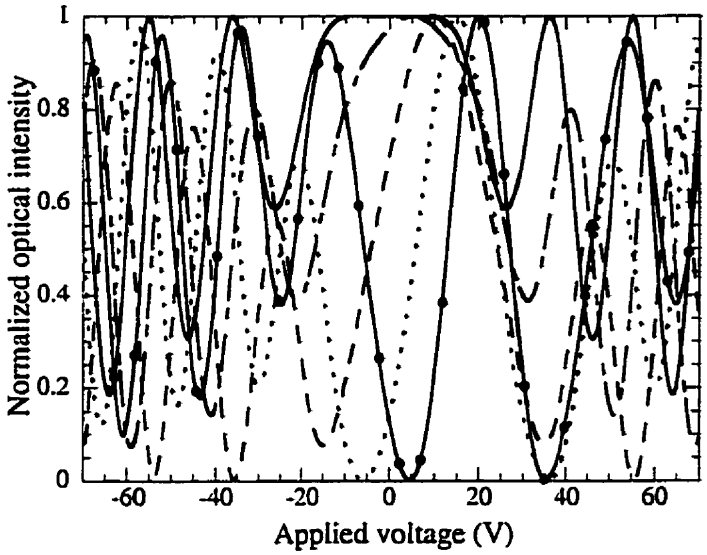

Figure 2.12 Transfer function of a polarization independent MC-MZI intensity modulator for input TE and TM polarized signals with optical waveguide modal birefringence of $\Delta n = 2\times10^{-4}$ and optical phase difference of $\Delta\varphi_{const} = 0$ for different side electrode bias voltage, 0 V(solid), 10 V(dashed-dotted), 20 V(dashed), 30 V(dotted), and 40 V(solid-circled). The RF signal is applied to the center electrode.

wave voltage, V_π, depends upon the bias point of the side electrode. The modulator operating point can be chosen on either side of the peak transfer function to generate an in-phase or out-of-phase optical output signal with regard to the applied RF signal. This configuration provides a higher extinction ratio and a lower V_π at lower bias voltage of the center electrode compared to the last bias configuration. Figure 2.13 illustrates effects of optical phase difference between the two arms of MZI, $\Delta\varphi_{const}$, on the transfer function of the modulator with $\Delta n \neq 0$. The transfer function is calculated for the MC-MZI intensity modulator with optical waveguide birefringence of $\Delta n = 2\times10^{-4}$ and optical phase difference, $\Delta\varphi_{const} = 45°$.

When $\Delta n \neq 0$, both on-off extinction ratio and the polarization insensitivity of the device deteriorates with an increase in the optical path length difference between the two arms of the MZI.

When $\Delta n = 0$, the transfer function is exactly the same as the last case except it has been shifted to the right or left. In other words, a zero birefringence waveguide MC_MZI intensity modulator maintain its polarization insensitivity with an optical

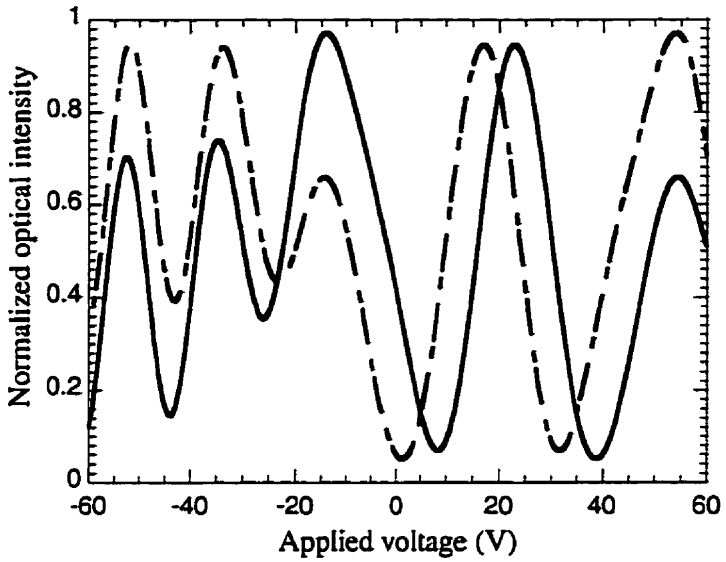

Figure 2.13 Transfer function of a MC-MZI intensity modulator for input TE (solid) and TM (dashed) polarized optical signals with optical waveguide modal birefringence of $\Delta n = 2\times10^{-4}$ and optical phase difference of $\Delta\varphi_{const} = 45°$. The side electrode is biased at 40 V and the RF signal is applied to the center electrode.

phase difference but loses its high on-off extinction ratio. This particularly enables the designer to design the modulator to operate at zero bias voltage for the center electrode. This can be achieved by changing the bias point of the side electrode. Other than that there is no advantages for this configuration over the last case.

3. In the third configuration, the signal is applied to one of the side electrodes and the two other electrodes are grounded. In fact, the modulation is performed only on one arm of the MZI and the optical signal in the other arm is unaffected by the applied electric field. The transfer function of the device is given in Figure 2.14. As expected, since the device is not operated in the push-pull fashion, this configuration does not offer an effective scheme for modulation. In fact, the half-wave voltage of the device under this biasing configuration is almost twice as the last cases. Despite doubling the half wave voltage over the last two cases, this configuration offers large on-off extinction ratio at relatively low bias voltage. Since this case is not of practical importance, we do not discuss the effect of asymmetry in the MZI, but briefly it is very similar to the second biasing configuration. An MC-MZI intensity modulator with zero birefringence optical waveguides maintains its polarization insensitivity

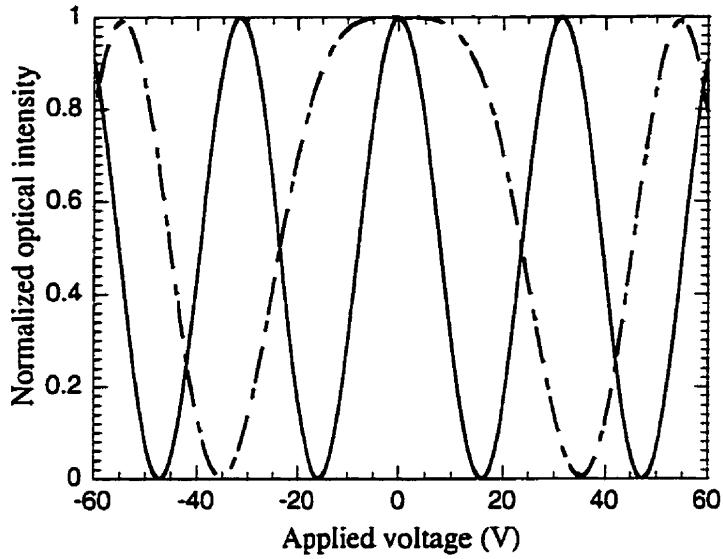

Figure 2.14 Transfer function of a MC-MZI intensity modulator for input TE and TM polarized signals with optical waveguide modal birefringence of $\Delta n = 0$ (solid) and $\Delta n = 2\times10^{-4}$ (dashed). The RF signal is applied to one of the side electrodes. The other two electrodes are grounded.

with any optical phase difference in MZI, but looses its large on-off extinction ratio. If the device employs birefringent optical waveguides and has an asymmetric MZI, both polarization independence and high on-off extinction ratio degrades.

In conclusion, the second biasing configuration offers the designer the maximum degree of freedom to optimize the bias point, on-off extinction ratio, half wave voltage. This case offers the possibility of achieving an efficient modulator without requiring zero birefringence optical waveguides.

2.3 Microwave Structure

The potential modulation bandwidth of waveguide modulators depends upon the electrode type and geometry and upon the substrate dielectric constant. There are two electrode configurations, lumped and traveling-wave electrodes, which can be used in electro-optic waveguide modulators. The modulation bandwidth for lumped electrode modulators (whose electrode length is small compared to the RF wavelength) is the

smaller of the inverse of the optical or electrical transmit times and the time constant of the lumped circuit parameter. The latter is usually the more restrictive. Although the electrode can be made small to increase the bandwidth, it will also increase the half wave voltage.

The goal of the traveling wave electrode is to make the electrode appear as an extension of the driving transmission line. As such, it should have the same characteristic impedance as the source and the cable. In this case, the modulator bandwidth is limited by the velocity mismatch between the optical signal propagating in the optical waveguide and the RF modulating signal moving down the electrodes. To examine the bandwidth limitation of traveling wave modulators, we assume the electrode impedance to be matched to the connecting cable and source. The microwave drive signal is:

$$V(z,t) = V_0 e^{-\alpha_m z} \sin\left(\frac{2\pi N_m}{\lambda_m} z - 2\pi f t\right) \tag{2.18}$$

where $N_m = \sqrt{\varepsilon_r}$, λ_m and f are the microwave refractive index, free space wavelength, and frequency, respectively. α_m is the microwave loss coefficient in Np/unit length, V_0 is the input microwave voltage, and z is the position along the electrode. The voltage seen at any point along the electrode by a photon that enters the optical waveguide at any time t_0 can then be written as:

$$V(z,t_0) = V_0 e^{-\alpha_m z} \sin 2\pi f\left(\frac{N_m \delta}{c} z - t\right) \tag{2.19}$$

where $\delta = 1 - N_o / N_m$ is a measure of velocity mismatch between the optical and microwave signals, N_o is the effective refractive index of the optical waveguide. Since the electro-optically induced phase shift per unit length, $\Delta\beta$, is proportional to V, the integrated phase shift over the electrode length, l, is:

$$\Delta\varphi(t_0) = \int_0^l \Delta\beta(f)dz = \Delta\beta_0 l \left\{\frac{1+\exp(2\alpha_m l) - 2\exp(\alpha_m l)\cos\theta}{(\alpha_m l)^2 + \theta^2}\right\}^{\frac{1}{2}} e^{-\alpha_m l} \sin(2\pi f t_0 - \phi + \psi) \tag{2.20}$$

where $\Delta\beta_0 = -\pi n_0^3 r_{41} V_0 \Gamma_s l / \lambda G$, Γ_s is the transversal overlap integral (factor) between the applied electric field and the optical mode, G is the interelectrode gap, $\theta = \pi f / f_d$, $f_d = c / (2N_m l\delta)$, and

$$\phi = \tan^{-1}\left(\frac{\theta}{\alpha_m l}\right) \tag{2.21}$$

$$\psi = \tan^{-1}\left(\frac{\exp(-\alpha_m l)\sin\theta}{1-\exp(-\alpha_m l)\cos\theta}\right) \tag{2.22}$$

If the characteristic impedance of the traveling wave electrode is not matched to those of the load and input transmission lines, the principals of the analysis remain the same, but both forward and reflected waves have to be considered in the analysis. Therefore, if the electrodes are lossless, α_m = 0, and if N_o = N_m, the optical wave travels down the waveguide at the same speed as the microwave signal moves along the electrode and sees the same voltage over the entire electrode length. Therefore, as Equation 2.20 shows, $\Delta\varphi(t_0)$ is proportional to $V_0 l$ and arbitrary long electrodes can be used to reduce the required drive voltage with no frequency limitation. However, for $N_o \neq N_m$ and $\alpha_m = 0$, there is a walk-off between the optical wave and microwave signal which results in a reduction of $\Delta\varphi$. This results in a $sin(x)/x$ functional frequency response. Some researchers have defined the modulator 3 dB bandwidth as the frequency for which the integrated phase change is reduced by 50 percent relative to its low frequency value and is expressed as:

$$\Delta f . l = \frac{2c}{\pi N_m \delta} \tag{2.23}$$

The dominant bandwidth limitation of traveling wave electro-optic modulators is the velocity mismatch between the optical signal and RF modulating signal in the interaction region. The value for $N_m\delta$ for GaAs is almost 0.75 that results in a 21.7 GHz.cm bandwidth electrode length product for a lossless electrode. If the electrodes are lossy, $\alpha_m \neq 0$, and velocity match condition is achieved, $N_o = N_m$, Equation 2.20 reduces to:

$$\Delta\varphi(t_0) = \int_0^l \Delta\beta(f)dz = -\Delta\beta_0 l\left(\frac{1-e^{-\alpha_m l}}{\alpha_m l}\right)\sin(2\pi f t_0) \qquad (2.24)$$

For a given electrode dimension, the high frequency microwave loss is determined by the skin effect and one expects a loss in dB/cm proportional to $\sqrt{f}$ [61]. From Equation 2.24, it can be shown that in the velocity match condition the frequency at which the total electrode loss reaches 6.34 dB determines the 3 dB bandwidth of the modulator. So if the velocities of optical and microwave signals are matched, the modulator bandwidth is mainly limited by the unavoidable frequency dependent microwave losses of electrodes and the modulator bandwidth extends well into the millimeter frequency range. Therefore, in addition to phase velocity matching, microwave losses should be minimized. It should be clear by now that both the half-wave voltage of the modulator and the 3-dB modulation bandwidth are inversely proportional to the electrode length. Therefore, although an increase in the electrode length will reduce the half wave voltage, it will also reduce the modulation bandwidth.

In the following, the effect of different parameters of a traveling wave modulator on the modulation bandwidth will be discussed. Since the prime goal of this thesis is the design and fabrication of traveling wave intensity modulators, from now on, the 3-dB modulation bandwidth is defined as the frequency at which the output modulated optical power is reduced by 3 dB. Figure 2.15 shows the variation of a traveling wave modulator bandwidth as a function of microwave loss with velocity mismatch as parameter. The characteristic impedance of the line is 50 Ω and electrode length is considered to be 1 cm. The modulation bandwidth of a traveling wave electro-optic modulator demonstrates large sensitivity to microwave loss for small velocity mismatch. As the velocity mismatch increases over 10%, the modulation bandwidth remains almost constant with an increase in microwave loss. A large bandwidth, ≥ 40 GHz, can be achieved with a velocity mismatch less then 5 percent and microwave loss less than 2.25 dB/cm.sqrt(GHz) depending upon the velocity mismatch. As a rule of thumb, a high speed traveling wave modulator has to demonstrate microwave loss of less than 1 dB/cm.sqrt(GHz) and velocity mismatch less then 5%. Therefore, electrode microwave

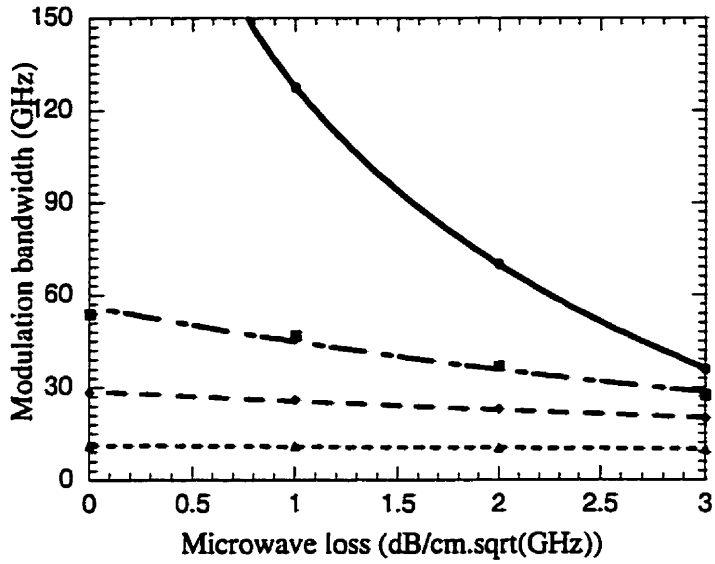

Figure 2.15 Modulation bandwidth of a traveling wave electro-optic modulator as a function of electrode microwave loss for different velocity mismatches of zero (solid), 5% (dashed-dotted), 10% (dashed), and 30% (dotted).

loss is a very critical parameter in the design of high-speed traveling-wave modulators with small velocity mismatch.

In addition to the phase velocity mismatch, characteristic impedance of the traveling wave electrode should also be matched to that of input transmission line and output load, 50 Ω. Figure 2.16 shows the normalized modulation spectrum as a function of frequency with characteristic impedance of the electrode as parameter. It is assumed that the electrode loss is 1 dB/cm.sqrt(GHz) and velocity mismatch is 5%. As expected, any impedance mismatch results in some ripple in the frequency response. A decrease in the characteristic impedance of the line marginally increases the modulation bandwidth. For example, reducing the characteristic impedance of the electrode from 50 Ω to 40 Ω increases the bandwidth from 46.5 GHz to 48.5 GHz, and introduces a maximum of 0.6 dB ripple at low frequencies. The ripple amplitude reduces for higher frequencies. Therefore, depending upon the tolerable amount of ripple in the frequency response, the traveling wave electrode can be designed with lower characteristic impedance. The obvious setback of this technique is the reduction in the amount of the transmitted power to the electrode, hence, higher half-wave voltage.

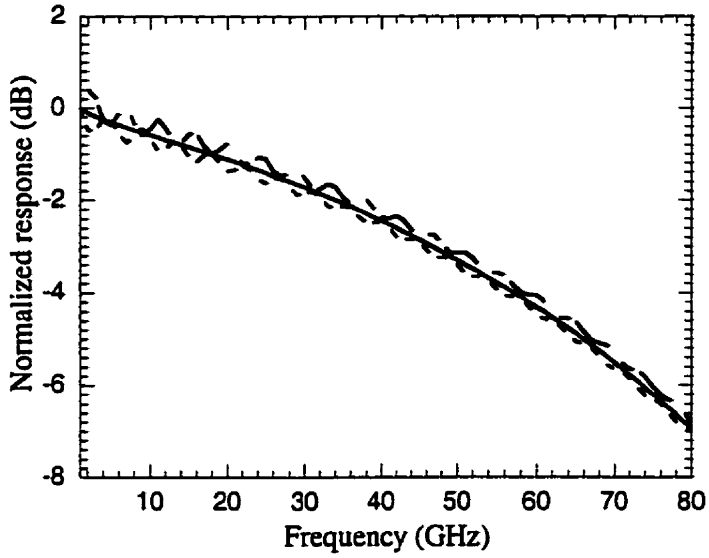

Figure 2.16 Modulation spectrum of a traveling wave modulator as a function of frequency for different electrode charateristic impedances of 40 Ω (dashed-dotted), 50 Ω (solid), and 60 Ω (dashed).

Both coplanar strip (CPS) and coplanar waveguide (CPW) configurations can be used in the design of traveling wave electro-optic modulators. The advantage of coplanar transmission lines over microstrip lines is the presence of the ground plane at the surface of the substrate that facilitates the fabrication of active and passive microwave elements. Coplanar transmission lines also support quasi-TEM mode propagation and therefore the microwave dispersion is practically negligible. In the future chapters some experimental results will be given that support the statement. In a planar transmission line such as CPW and CPS, the phase and group velocities of the microwave signal are practically the same. On the other hand, due to hybrid mode propagation, microstrip lines are highly dispersive [19]. This in turn limits the modulation bandwidth in a traveling wave modulator. In the coplanar strip and coplanar waveguide structures, the electric field propagates almost equally in the substrate and in the air. The microwave effective index is given approximately by [61]:

$$N_m = \sqrt{\frac{\varepsilon_r + 1}{2}} \tag{2.25}$$

where ε_r is the dielectric constant of the substrate (GaAs: ε_r = 13.1). In the III-V compound semi-conductors such as GaAs, InP and their ternary and quaternary compounds, the microwave refractive index of a coplanar structure is less than the optical refractive index. For example for GaAs N_m = 2.655 and $N_o(\lambda=1.55\ \mu m)$ = 3.35. Therefore, the modulating microwave signal travels faster than the optical signal. In order to achieve velocity match condition, the microwave signal velocity has to be reduced to match that of optical signal. In this case, these electrodes are called slow wave electrodes. In the lithium niobate and glass substrates, the effective refractive index of the optical waveguide is less than the microwave refractive index of the coplanar structure. So, the velocity match is obtained by reducing the capacitance and/or inductance per unit length of the line and therefore, increasing the velocity of microwave signal. These electrodes are called fast wave electrodes. Since the purpose of this thesis is to develop large bandwidth modulators on semiconductor materials, we only focus on the design of slow wave electrodes.

Assuming a quasi-TEM mode propagation for a lossless coplanar structure, the characteristic impedance and the phase velocity of the line can be given by:

$$Z_0 = \sqrt{\frac{L}{C}} \tag{2.26}$$

$$V_{ph} = \frac{1}{\sqrt{LC}} \tag{2.27}$$

where L and C are inductance and capacitance per unit length of the line, respectively. The phase velocity of the transmission line can be reduced by increasing L or C or both. Changing the dimension of the uniform transmission line will change the capacitance and inductance of the line, but the LC product and therefore phase velocity will remain almost constant. This objective can be achieved by using nonuniform transmission lines. Capacitive or inductive elements can be added periodically to the uniform transmission line to increase the total capacitance or inductance of the line. If the periodicity of the loading elements is small compared to the microwave wavelength at the frequency of operation, the loaded line will appear electrically smooth.

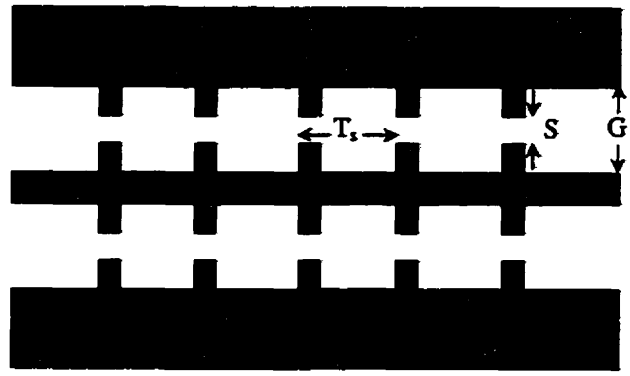

Figure 2.17 Schematic diagram of a coplanar waveguide periodically loaded with narrow fins to increase the capacitance per unit length of the line and therefore to reduce the phase velocity of the microwave signal.

For example, Figure 2.17 shows a uniform coplanar waveguide loaded with narrow fins as capacitive elements. The fringing electric field in the vicinity of the fins increases the local stored electric energy. This will translate to an increase in the shunt capacitance of the loaded coplanar waveguide. The presence of these fins will also change the characteristic impedance of the line. It is possible to change the geometry of the fins and/or the uniform transmission line to match the phase velocity of microwave signal to that of the optical signal and the characteristic impedance to 50 Ω or the desired value.

The frequency characteristic of a capacitively loaded transmission line is given as [62]:

$$\cos(\beta_l T_s) = \cos(k_0 T_s) - Z_{0nl} \frac{\omega C_l}{2} \sin(k_0 T_s) \tag{2.28}$$

where β_l is the phase constant of the loaded transmission line, k_0 and Z_{0nl} are the phase constant and characteristic impedance of the uniform (unloaded) transmission line, T_s is the periodicity of interval, C_l is the shunt load capacitance. This function shows passband and stopband intervals in the frequency response of the loaded transmission line. The first passband of this curve for a coplanar periodic structure on GaAs substrate with Z_{0nl} = 66.5 Ω, C_l = 10.22 fF, and T_s =100 μm is shown in Figure 2.18. These values provide a traveling wave electrode with characteristic impedance of 50 Ω and velocity match

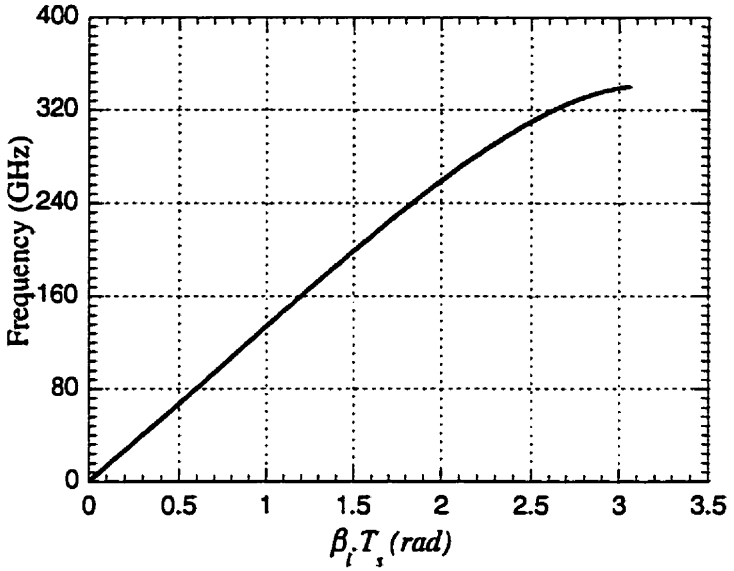

Figure 2.18 Frequency variation of the first passband of the periodically loaded coplanar structure on GaAs as a function of $\beta_t T_s$.

condition with an optical mode in a GaAS/AlGaAs optical structure. For a given structure, the frequency of operation has to stay well away from the cut-off frequency to minimize the line dispersion. This curve shows that the dispersion in the microwave signal caused by this structure is negligible up to frequencies well above 100 GHz, the operational bandwidth of these devices. The cutoff frequency of a periodically loaded transmission line is approximately

$$f_{cut-off} \cong \frac{V_{ph(sw)}}{2T_s} \tag{2.29}$$

For T_s =100 μm and $V_{ph(sw)} \cong$ 8.5 cm/nsec (for GaAs/AlGaAs optical structure at 1.55 μm wavelength), the cutoff frequency is almost 425 GHz. This indicates that for frequencies below 200 GHz dispersion due to the periodicity of the structure is negligible.

2.4 Modulation Chirp

Chirp is a critical element in a well-designed high-speed long distance multigigabit system because it can ultimately limit the transmission span. Chirp tends to cause the guided modes to spread out and create interference. Most optical fiber

transmission systems today, whether they transmit digital or analog data, rely on direct modulation of a laser to generate the time varying signals. This method works for low speed systems. For high-speed systems, narrow linewidths are required in the optical source to keep dispersion to a minimum. However, the direct modulation of a laser cavity forces the width to widen. The variations in the carrier density, produced by changes in the injected modulation current, affect the index of refraction in the laser cavity. This causes the wavelength to vary and the result is a broadened linewidth. This phenomenon is referred to as laser chirp which is given in terms of (MHz/mA).

External modulators offer a way to reduce or eliminate chirp because the laser source is held in the narrow linewidth, steady-sate CW mode. Operating the laser in the CW state also reduces the laser driving circuitry and therefore temperature stability problems. This continuous beam is then acted upon by an external form of modulation to generate useful information. The external modulator is typically either an electro-optic modulator or an electro-absorptive modulator.

Electro-absorptive modulators are operating near the band gap wavelength of the optical material. Because of Kramers-kronig relations, which relate the real and imaginary parts of the index of refraction, we know that any change in the imaginary part must lead to a change in the real part. Thus the electro-absorption effect observed in MQW's must be accompanied by an electro-optic effect. Since the operational wavelength of the electro-absorptive devices are close to the excitonic wavelength of the MQW's, any change in guided mode intensity is accompanied by relatively large change in the phase of the optical signal. This is one of the major disadvantages of electro-absorptive modulators.

In the following, the chirp characteristics of an electro-optic MZ intensity modulator are discussed. The incoming optical field undergoes a phase change in each arm of the MZ modulator. The respective phase change is due to the applied voltage acting on that arm. The resulting exit field from the modulator is thus:

$$E = E_0 \cos\left(\frac{\varphi_2 - \varphi_1}{2}\right) \exp\left(j\frac{\varphi_2 + \varphi_1}{2}\right) \tag{2.30}$$

where E_0 is the input optical field, φ_1 and φ_2 are the phase change in two arms of MZI. By definition, the chirp α of a modulator is the ratio of the phase modulation to the amplitude modulation as [63]:

$$\alpha = 2S\frac{\left(\frac{d\varphi}{dt}\right)}{\left(\frac{dS}{dt}\right)} \tag{2.31}$$

where φ is the average phase change in each arm, and the intensity, S, is the square of the field. The phase change in each arm is related to the length of that arm and the index of refraction. The change in the refractive index in each arm is proportional to the applied voltage to that arm of the MZI, $\Delta n_i(t)=\eta_i V_i(t)$. If it is assumed that the arms of the device are driven with $V_1(t)=V_1 sin(\omega t)$ and $V_2(t)=V_2 sin(\omega t)+V_b$, V_b is the bias voltage, the modulator chirp factor cab be obtained as:

$$\alpha = \left(\frac{\eta_1 V_1 + \eta_2 V_2}{\eta_1 V_1 - \eta_2 V_2}\right)\cot\left\{\left(\frac{\pi l}{\lambda}\right)\left(\eta_2 V_2 \sin(\omega t) + \eta_2 V_b + \eta_1 V_1 \sin(\omega t)\right)\right\} \tag{2.32}$$

where l is the arm length of the MZI. In a push-pull operation of the MZ modulator such as devices considered in this research, the voltage applied to the arms of the MZI are of opposite polarity and equal amplitude, $V_1 = -V_2$. This achieves a zero chirp modulation. This, in fact, is the most attractive feature of the electro-optic modulators compared to electro-absorptive modulators for long haul optical transmission systems. Of course, other driving schemes can also be applied to achieve even a negative chirp factor.
The voltage applied to the modulator can control the chirp and thereby helps to maximize the overall system length.

2.5 Discussion

This chapter has served as a theoretical introduction to electro-optic modulation and the associated subjects related to the traveling-wave modulators. The chapter began by outlining some basic modulation principles and then proceeded to distinguish different

modulation techniques. The requirements for large bandwidth modulation, polarization sensitive and polarization insensitive modulation were discussed with particular attention to semiconductor materials as substrates.

The next chapter will discuss the design aspects of heterostructure epitaxial layers for optical waveguides, and traveling wave electrodes. It will begin with the design of heterostructure optical layers with attention to electro-optic modulation. Then the discussion moves to the design of slow-wave electrodes.

CHAPTER 3

Design of Traveling Wave Electro-Optic Modulators

In this chapter we will discuss the issues in the design of traveling wave electro-optic modulators. This includes the design of heterostructure optical layers, traveling wave electrodes and different configurations. Some of these issues are the optical and electrical overlap integral, single mode optical fiber to waveguide coupling, optical and microwave losses and their effects on the overall performance of the modulator.

3.1 Optical Structures

3.1.1 Design of Heterostructure Epitaxial Layers

There are a few considerations that have to be made in the design of heterostructure epitaxial layer for optical applications. One of the major issues here is the

optical insertion loss. The insertion loss is comprised of coupling loss, Fresnel reflection loss, propagation loss due to scattering to air and substrate, free carrier absorption, and electrode proximity [64]. To reduce the coupling loss, it is necessary to design the optical guide to couple efficiently to a single mode fiber with a 9 μm core diameter. When the two modes are exactly the same, the coupling efficiency is maximized. So, the optical guide mode should be symmetrical in the vertical and lateral direction and close to a circular mode. This leads us to a very large optical mode size with almost 9 μm vertical and lateral width. On the other hand, the other requirements lead us to the design of smaller optical modes and therefore smaller ridge optical waveguides. The main purpose of designing traveling wave electro-optic modulators on semiconductor materials is its potential for integration with lasers and other optical and optoelectronic components on the same wafer. Therefore, the optical mode size in these modulators can be as small as in laser sources to reduce the coupling losses.

Besides, an efficient modulator design requires a large overlap factor between the optical and electrical signals. Researchers have shown that the interelectrode gap has to be between 0.5 to 1 times the optical mode lateral width in an efficient electro-optic modulator [55],[65]. Therefore a large optical mode size translates to an almost large gap. On the other side, the interelectrode gap has to be small to establish a large electric field in the optical waveguide. Optimization of the electro-optic induced index change thus requires both minimizing the optical waveguide mode size and interelectrode gap.

In addition to the facts stated above, the single mode propagation of optical signal with large waveguide dimensions requires a very small difference in the refractive indices between the core and the clad region. In the lateral direction that means a very shallow etching and therefore a very loosely confined optical mode. This results in higher optical losses particularly at waveguide bends. The refractive index difference in the vertical direction is provided by changing the material composition in the clad and core layers. There are practical limitations in the accuracy of the layer compositions. For example, all manufacturers of the epitaxial layers have difficulties growing AlGaAs layer with aluminum concentration of less than 7%.

A highly confined optical mode in a small waveguide increases the coupling loss to a single mode optical fiber. There are different techniques to increase the coupling efficiency. The use of lensed optical fiber or micro-lense can match the mode size of a single mode fiber to that of a semiconductor waveguide and thereby greatly increase the coupling efficiency. Optical mode spot size transformation techniques can also be used to increase the optical waveguide mode spot size and match that to the optical fiber [66]. It can be achieved by employing vertical couplers using polymer waveguides. Due to the close proximity of the refractive index of the polymer waveguides to that of optical fiber, optical mode size of as large as optical fiber mode size can be obtained.

The optical mode has to be as close as possible to the surface of the wafer where the applied electric field has its maximum values. One way to achieve this is to remove the top cladding layer that will result in an undesirable asymmetric optical mode in the vertical direction. The presence of top cladding layer attenuates the optical mode in the vertical direction so that the optical loss due to electrode proximity and defects on the surface of the substrate is also minimized. Therefore, a top cladding layer is considered for the optical structure. The bottom-cladding layer has to be chosen to minimize the leakage loss of the optical mode to the substrate. This is usually done by choosing a thick bottom-cladding layer (normally ≥ 4 μm).

The effective index method and beam propagation method (BPM) were used in the design of the heterostructure epitaxial layers [67]-[68]. Figure 3.1 illustrates different layers of the designed ridge optical waveguides. The two structures are two generations of the optical structures designed for this research. The optical waveguides on wafer #1 optical structure have ridge width, W, of 3, 4, and 5 μm and on wafer #2 have width of 2 and 2.5 μm. The maximum ridge width is chosen to generate a single mode propagation for both states of polarization (TE and TM polarization) and for the given ridge height. In the second optical structure, wafer #2, a thin layer of GaAs of 2.5 nm was inserted in every 200 nm of $Al_xGa_{1-x}As$ to smooth the surface during growth. The top thin layer of GaAs is supposed to prevent the AlGaAs layer from oxidization. A SiO_2 layer of 0.2 μm is also deposited to both structures after etching to reduce the optical loss due to the

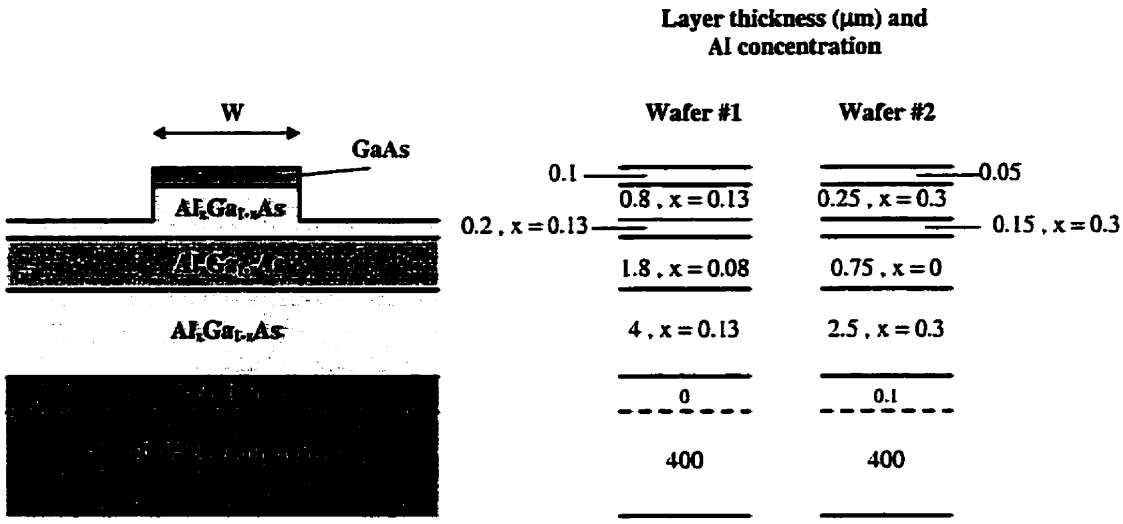

Figure 3.1 Cross section of the ridge optical waveguide. The two columns for the thickness and Al concentration are given for the two generations of optical structures designed for traveling wave electro-optic modulators.

proximity of the optical mode and metallic electrode. Although the presence of this dielectric layer significantly reduces the applied electric field in the optical waveguide region [69], it also attenuates the tail of the optical mode in the vicinity of the metal electrode and therefore reduces the optical loss. The ideal material for such dielectric layer would have a refractive index of one at optical frequencies and dielectric constant equal to that of the substrate at microwave frequencies. In this case, while the microwave signal will not be affected by the presence of such dielectric layers, the optical mode tail would be attenuated by the maximum refractive index difference and therefore the optical loss will be minimized. Table 3.1 gives the designed parameters of the optical waveguides on wafer #1 and wafer #2 optical structure for the maximum ridge width of 5 μm and 2.5 μm at the wavelength of 1.55 μm , respectively. These parameters consist of effective index, phase velocity, group index, group velocity, and coupling loss to a single mode fiber for both states of polarization. In these calculations, the effect of the thin layer of SiO_2 was also considered. The effective indexes of optical modes in waveguides are calculated using effective index method and finite difference method. Although the latter is more accurate, both techniques provide enough accuracy to be used for velocity–matching application.

Table 3.1 Parameters of the optical mode fabricated on wafers #1 and #2.

Wafer No.	n_{eff}		V_{ph} (cm/nsec)		n_g		V_g (cm/nsec)		Coupling loss (dB)
	TE	TM	TE	TM	TE	TM	TE	TM	
1	3.32321	3.323	9.02741	9.028	3.48608	3.48635	8.60565	8.605	3
2	3.31334	3.30916	9.05431	9.06574	3.53721	3.54101	8.48126	8.47216	6.2

In the first design, the aluminum concentration in the cladding layer is 13% and in the guiding layer is 8%. Theoretically, almost the same characteristics and mode profile can be obtained if the aluminum concentration in the cladding layer is 5% and the guiding layer is pure GaAs. The latter design also has lower carrier concentration to minimize the free carrier absorption. The only problem with this design is that no commercial manufacturer can guarantee the aluminum concentration below 7-8 percent. In the second design, the aluminum concentration between the core and clad was increased to 30% to reduce the mode size in both lateral and vertical directions. Due to larger refractive index difference in this design, the ridge height is also smaller and therefore the optical mode is also closer to the surface.

As opposed to traveling wave planar electrodes that are practically nondispersive, optical waveguides are dispersive. The dispersion is due to material and modal dispersion. Therefore there is some difference between the phase and group velocity of optical signal propagating in a ridge optical waveguide. The group index of an optical waveguide is given as:

$$n_g = n - \lambda \frac{dn}{d\lambda} \tag{3.1}$$

where n is the effective refractive index of the optical waveguide for TE or TM polarization. The optical signal group velocity is the velocity at which the optical information is traveling in the optical waveguide. The group velocity of optical signal is less than the its phase velocity. Therefore, the phase velocity of microwave signal has to be matched to the group velocity of optical signal to achieve maximum available bandwidth for a given electrode loss.

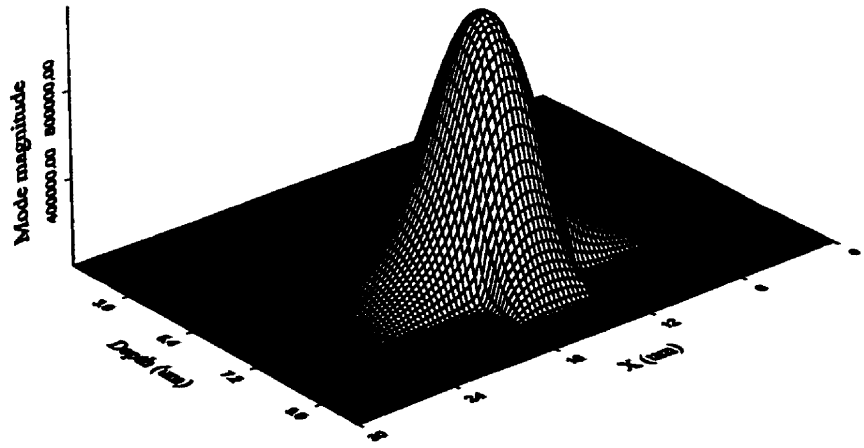

Figure 3.2 Mode profile of a 5 μm wide waveguide on the wafer #1 optical structure.

Theoretically, optical waveguides with different widths demonstrate different effective indices for different states of polarization that have to be match by the traveling wave electrodes. Within the single mode propagation constraints, the effect of ridge width and height change on the effective index of optical waveguides does not exceed 2%. This error is within the error in the electrode design and device fabrication process. Since the ridge height remains the same for all optical waveguides on a mask, the confinement factor for the fundamental mode of the optical waveguide with smaller width will be smaller. The optical mode profile of the first optical structure with 5 μm width is given in Figure 3.2.

Microwave insertion loss is mainly due to electrode metallization and substrate free carrier absorption. The former can be minimized by the optimal design of the electrodes. The carrier concentration in optical epitaxial layers and substrate has to be minimized to reduce free carrier absorption by the optical signal as well as by microwave signal. Free carrier absorption by the optical signal is given by the following empirical expression [70]:

$$\alpha_o(cm^{-1}) = 1.3\times10^{-18} N(cm^{-3}) \tag{3.2}$$

where N is free carrier density. As Equation 3.2 shows, a carrier concentration of 1.8×10^{16} cm^{-3} causes a negligible optical absorption loss of 0.1 dB/cm. On the other hand, this amount of carrier concentration in the substrate can cause huge microwave losess.

This was observed during the microwave s-parameter measurements of the traveling wave electrodes on such substrates. In fact, microwave loss imposes much more strict limitation on the substrate carrier concentration than optical loss. Researchers have reported the operation of traveling wave electro-optic modulators on unintentionally doped GaAs substrates. There has not been a critical study on this subject to describe more accurately the actual doping density of the substrate. An experimental study was performed to determine the maximum carrier concentration in the heterostructure epitaxial layers before creating an unacceptable level of microwave loss. This issue will be discussed in more detail later in another chapter. The results of the study suggest that semiconducting materials used for fabrication of traveling wave electro-optic modulators must not exceed carrier doping level of 5×10^{14} cm^{-3}. Therefore, in the optical structures presented here, the substrates are semi-insulating (SI) (doping density of 10^{8} cm^{-3}, as given by the manufacturer) and the carrier concentration of all epitaxial layers are less than 5×10^{14} cm^{-3}.

3.1.2 Leakage Loss and Mode Tail Engineering

Semiconductor optical waveguides are basic building blocks for passive and active optical circuits and optoelectronic devices. The GaAs/$Al_yGa_{1-y}As$ is an important optical waveguide material system used for these applications. One of the loss mechanisms in GaAs/$Al_yGa_{1-y}As$ optical waveguides is the leakage loss, caused by guided optical modes being coupled into non-guided radiation modes through the bottom cladding into the GaAS substrate. To reduce this leakage loss, a thick $Al_yGa_{1-y}As$ bottom-cladding layer is usually required. For example, to achieve a loss below 0.1 dB/cm, 4 μm thick $Al_yGa_{1-y}As$ bottom cladding layer is needed for an Al mole fraction y<10%.

A novel approach has been taken to shape the tail of the optical mode and therefore, reduce the leakage into the substrate. In this technique, thin layers $Al_xGa_{1-x}As$, $y<x\leq 1$, are inserted in the bottom cladding layer. The presence of these thin layers of lower index material suppresses the tail of the fundamental mode and thereby reduces the

leakage into the substrate. This in turn permits to drastically reduce the thickness of the bottom-cladding layer, while maintaining the integrity of the waveguide. The composition, thickness, and the position of the inserted thin $Al_xGa_{1-x}As$ layers are optimized in a such a way that the original waveguide parameters (effective index, optical confinement,...) are approximately maintained. Nearly 50% reduction of the total cladding thickness can be achieved when compared with conventional cladding layer thickness.

The insertion condition of the thin layers of $Al_xGa_{1-x}As$ in the cladding is not restricted to the bottom cladding layer and $y<x\leq 1$ condition. For example, in the case of traveling wave electro-optic laser modulators, it is important to maximize the overlap integral between the modulating electric field signal and the optical mode. One can achieve this by forcing the optical mode toward the surface of the device, where the electric field is the strongest. This may be accomplish by inserting thin layers of $Al_xGa_{1-x}As$, $(0\leq x<y)$, into the top cladding of the ridge waveguide.

In order to demonstrate the advantages of the inserting thin $Al_xGa_{1-x}As$ layers into the bottom cladding of $GaAs/Al_yGa_{1-y}As$ waveguides, three different layer structures were designed. The first consist of a control sample, (wafer #3), which represents a typical waveguide design for traveling wave electro-optic modulators, without the thin $Al_xGa_{1-x}As$, (Table 3.2)

In the second design, (wafer #4), the top cladding and guiding layer remains the same as for wafer #3, but a thin AlAs layer is inserted in the bottom cladding layer. The layer structure is given in Table 3.3.

The bottom cladding later thickness and the position of the insert layers were optimized until simulation indicates waveguide properties close to that of wafer #3. With this structure the total thickness of the bottom cladding was reduced by 36.5%.

In our third design, an $Al_xGa_{1-x}As$ ($x=0.25$) and an AlAs layers are inserted into the bottom cladding layer. Again, in order to yield the same waveguide properties as that of the control sample, wafer #3, the relative position of the inserts and the thickness of the bottom cladding were optimized using our simulator. The bottom cladding thickness is reduced by 46.6%. Table 3.4 contains the layer structure for the wafer #5.

Table 3.2 Heterostructure epitaxial layers of a typical planar waveguide (wafer #3), no thin layer of $Al_xGa_{1-x}As$ is inserted.

Layer #	Material	Al Concentration %	Thickness (μm)	Function
1	GaAs	0	0.1	Cap layer
2	$Al_yGa_{1-y}As$	7	1	Top clad
3	GaAs	0	1.75	Waveguide core
4	$Al_yGa_{1-y}As$	7	4	Bottom clad
5	GaAs	0	500	SI-substrate

Table 3.3 Heterostructure epitaxial layers of a planar waveguide with one thin layer of $Al_xGa_{1-x}As$ inserted in the bottom clad (wafer #4).

Layer #	Material	Al Concentration %	Thickness (μm)	Function
1	GaAs	0	0.1	Cap layer
2	$Al_yGa_{1-y}As$	7	1	Top clad
3	GaAs	0	1.75	Waveguide core
4	$Al_yGa_{1-y}As$	7	2	Bottom clad
5	$Al_xGa_{1-x}As$	100	0.04	Insert layer
6	$Al_yGa_{1-y}As$	7	0.5	Bottom clad
7	GaAs	0	500	SI-substrate

Table 3.4 Heterostructure epitaxial layers of a planar waveguide with two thin layers of $Al_xGa_{1-x}As$ inserted in the bottom clad (wafer #5).

Layer #	Material	Al Concentration %	Thickness (μm)	Function
1	GaAs	0	0.1	Cap layer
2	$Al_yGa_{1-y}As$	7	1	Top clad
3	GaAs	0	1.75	Waveguide core
4	$Al_yGa_{1-y}As$	7	0.65	Bottom clad
5	$Al_xGa_{1-x}As$	25	0.06	Insert layer
6	$Al_yGa_{1-y}As$	7	1.35	Bottom clad
7	$Al_xGa_{1-x}As$	100	0.075	Insert layer
8	GaAs	0	500	SI-substrate

The optical properties, such as effective indices, mode profile, leakage loss and confinement factors for the different modes supported in the slab waveguides in the three samples were calculated for both TE and TM polarization. The calculations give similar results except for the effective indices, which indicates small polarization dependence. The results are given in Table 3.5.

Table 3.5 Simulated parameters of the optical guided mode on three different heterostructure optical layers.

Calculated Parameter	wafer #3	wafer #4	wafer #5
$N^0_{eff(TE)}$	3.35946	3.35946	3.35934
$N^1_{eff(TE)}$	3.33603	3.33437	3.33299
L_0 (dB/cm)	0.01	0.326	0.316
L_1 (dB/cm)	115	64	52.1
Γ_0	0.87	0.86	0.87

Here $N^m_{eff}(TE)$ is the effective index for the TE guided modes (m=0,1,2,...), L_m is the leakage loss for each mode, and Γ_0 is the confinement factor for the fundamental mode. Results show that the waveguide properties for the fundamental mode, namely the effective index, leakage loss, and confinement factor do not change significantly as the thin $Al_xGa_{1-x}As$ layers are inserted in the bottom cladding layer. The position, composition, and thickness of the thin insertion layer can be optimized for a given device design to yield the required effective index, the acceptable leakage loss, and the required mode confinement.

We are also proposing that the insertion of thin $Al_xGa_{1-x}As$ layers, ($0 \le x < y$), in the top cladding layer can be used to modify the guided mode profile for specific applications such as traveling wave electro-optic modulators. It can reduce the thickness of the top cladding layer and modify the mode profile in such a way that while the overlap factor between the optical and electrical fields increases, optical loss due to proximity of optical mode to metallic electrode remains the same.

In other applications, where one needs to reduce the coupling losses between a single mode fiber and a semiconductor waveguide, waveguides with wider ridges and a thicker core layers are designed, whilst still maintaining a single mode operation. Wider ridges have the advantage of relaxing the photolithography and process requirements during component fabrication. Usually these design conditions can be met if the index

difference between core and cladding can be reduced. The drawback for such a design is that the thickness of the cladding layers, in particular, the layer between the core and the GaAs substrate, must be significantly increased. The technique demonstrated here relieves the thickness issues at the bottom-cladding layer.

Thin $Al_xGa_{1-x}As$, ($y \leq x < 1$), layers inserted in the bottom cladding layer has reduced its thickness by almost 50%. This also reduces the growth cost of the heterostructure epitaxial layers

The measurement results will be presented in the next chapter where the measurement techniques are discussed.

3.1.3 Optical Waveguide and Mach-Zehnder Interferometer

As discussed earlier, the electro-optic modulation consists of either phase modulation or mode conversion. A pure electro-optic mode converter is realized when a straight waveguide is positioned between two electrodes. In this case the electrodes are on either side of the straight optical waveguide. This device will function as an intensity modulator if a polarizer and an analyzer are being used with this device.

A Mach-Zehnder optical interferometer (MZI) is required to convert the phase modulation or mode conversion to amplitude (or intensity) modulation. Each interferometer consists of three sections: a power divider, an active section where the interaction between the optical and electrical signal takes place, a power combiner. The power divider and power combiner are fabricated as Y-branches. The Y-branch for the power divider and power combiner can also be replaced with three-branch coupler.

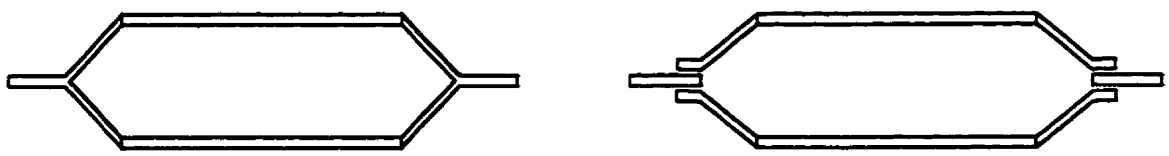

(a) (b)

Figure 3.3 Schematic diagram of MZIs used in traveling wave electro-optic modulators. a) Y-branch b) 3-branch coupler.

Figure 3.3 shows the two different MZ interferometers that have been used in the design of electro-optic modulators. The tilted waveguides in the Y-branch or coupler can be designed with s-bend waveguides that smooth the transition from one waveguide to another.

It is well known that the optical couplers are very sensitive to the design parameters. Some design parameters are hard to target in the fabrication process. These parameters are the ridge width, the ridge height, the spacing between two optical waveguides. Any change in these parameters will particularly effect the phase and splitting ratio at the junction and the device on-off extinction ratio. Therefore, only a few optical couplers were employed in the design of MZI. The principle of operation of a MZ interferometer is as follows. When there is no applied electric field, the input optical power is equally divided into two arms and then at the combiner, the two signals add in phase and constitute the original input signal. So the output optical power is equal to the input optical power. Now, if an applied electric field creates a phase delay of 180° in one arm of the active region, the asymmetric higher order mode will be excited at the output combiner. Since the output waveguide is designed to be single mode, the asymmetric mode will be attenuated rapidly and no optical power is detected at the output. The voltage that creates a phase delay of 180° is called half-wave voltage, V_π. The Y-branch has to be designed to minimize the optical loss at the junctions and reduce the overall device length. A large bending radius results in smaller optical loss and longer device length. The minimum bending radius for a given optical loss depends on the effective index of the optical waveguide. The more confined the optical mode is in the optical waveguide, the smaller the bending radius is. This bending radius is an important issue in devices whose length is small and/or the optical propagation loss per unit length is large. An example for such devices is the MQW electro-refractive intensity modulator operating near the bandgap wavelength [71]-[72]. This device is very short due to a large electro-optic coefficient and high optical propagation loss. Therefore, it makes sense to optimize the bending radius for such devices to reduce the Y-junction length as much as possible. In the traveling wave electro-optic modulators, since the electro-optic coefficient is very small (r_{41}=1.45×10^{-12} m/V) [73] and the electrode works as a

transmission line, the device is long (≥ 1 cm). Therefore, the Y-junction length is a small section of total device length that does not impose strict design criterion. The bending radius, which also depends on the arm separation, is directly related to the dimension and type of the slow wave electrodes. The bending radiuses were chosen to achieve optical loss of less than 0.1 dB per bend for the given slow wave electrode, optical structure, ridge width, and ridge height. A BPM-CAD simulator was used for the design and simulation of different optical elements such as Y-branch combiners and dividers, couplers, waveguides, etc [74].

3.2 Slow Wave Electrode Structures

As mentioned earlier, in III-V semiconductor materials, the microwave signal on coplanar electrodes travels faster than the optical signal propagating in the optical waveguide. Therefore, the phase velocity of microwave signal has to be reduced to match that of the optical signal to achieve maximum bandwidth available to the modulator, hence, slow wave electrodes. Capacitive and inductive elements can be periodically loaded to the uniform transmission line to reduce the phase velocity of the microwave signal. Capacitive elements in different combinations of narrow fins and pads (see Figure 2.17) can be added to the uniform transmission line. The design goals consist of a characteristic impedance of 50 Ω, phase velocity equal to that of the group velocity of the optical signal, approximately 8.5 cm/nsec depending on the epitaxial optical structure, and a low microwave loss, less than 1 $dB/cm.\sqrt{GHz}$.

In the slow wave structures (see Figure 2.17), due to the presence of fins and pads, not only is the electric field not uniform in any transversal plane, it is also a function of distance in the direction of propagation. Therefore, the expressions for the optical signal phase retardation, and the overlap factor between the optical and electrical signals have to be changed to accommodate the periodicity in the direction of propagation. For example, Equation 2.6 is changed as given below:

$$\Delta\varphi_{[100]} = -\pi n_0^3 r_{41} \frac{V}{G} \frac{N_c T_s}{\lambda} \Gamma_v \tag{3.3}$$

where N_c is the number of cells along the slow wave electrode, T_s is the periodicity of loading fins and pads, and Γ_v is the volume overlap factor (integral) defined as:

$$\Gamma_v = \frac{G}{V} \frac{1}{T_s} \int_{T_s} \iint_A E_{rf} \left| E_{opt} \right|^2 dA dz = \frac{1}{T_s} \int_{T_s} \Gamma_s dz \tag{3.4}$$

where the integration is over the cross section area of the optical mode and along one period of loading fins and pads. For simplicity, we assume that the electric field distribution in the substrate is constant where there is a pad and null in the area between the adjacent fins/pads. In this case, the volume overlap factor simplifies to:

$$\Gamma_v = \frac{W_p}{T_s} \Gamma_s = \Gamma_l . \Gamma_s \tag{3.5}$$

The longitudinal overlap factor (also called duty cycle) is defined as $\Gamma_l = W_p / T_s$. It can be used as a figure of merit for the slow wave electrodes and is a measure of the area along the electrodes, where the interaction between the optical signal and the electric field is maximal. Consequently, the electrode length has to be multiplied by the longitudinal overlap factor to obtain the effective interaction length of the slow wave structure. Therefore, an efficient traveling wave electro-optic modulator employs a slow wave electrode with longitudinal overlap factor close to one.

In the following, some of the benefits of using slow wave electrodes for high-speed electro-optic modulations are presented. As discussed earlier, the microwave loss is a limiting factor for the bandwidth of a traveling wave modulator. The microwave loss depends upon some parameters such as electrode conductivity and geometry, substrate dielectric constant and carrier concentration. Microwave loss due to substrate carrier concentration will be discussed in the next chapter. The metallic microwave loss is mostly determined by the proximity of the axial currents in the signal and ground electrodes. If the planar slow wave structure such as the one shown in Figure 2.17 is designed so that the axial transmission line currents cannot flow along loading fins and pads, and only displacement currents are flown in the small capacitive elements, current crowding and the microwave loss are determined by the distance between the signal

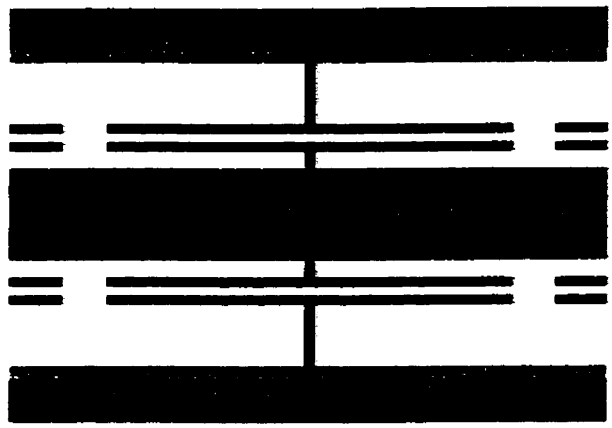

Figure 3.4 Current distribution along a slow wave electrode. High current density is shown by red color.

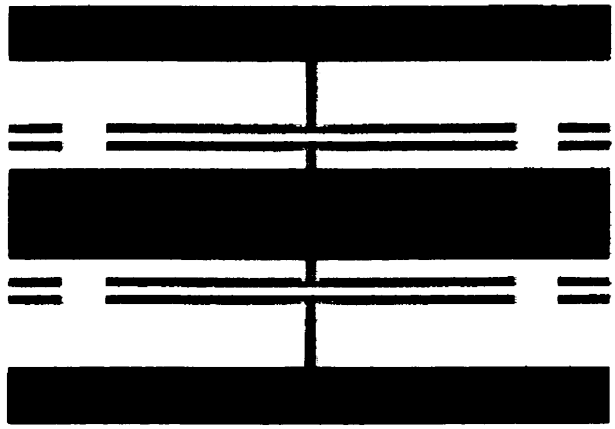

Figure 3.5 Charge distribution along a slow wave electrode. High charge density is shown by red color.

electrode and ground electrode of the unloaded transmission line, *G*. So, while the RF electric field intensity is determined by the gap between the pads, S, shown in Figure 2.17, the microwave loss are determined by the distance between the centre electrode and ground electrode of the unloaded transmission line, *G*. Figure 3.4 illustrates the current distribution along the slow wave electrode using *Sonnet* EM simulator [75]. The main current is flowing along the inner edge of the main signal and ground electrodes. Small width of fins and pads causes the current flow into the loading capacitive elements to be minimal.

This large distance between the main currents significantly reduces the microwave loss of the electrode that in turns increases the bandwidth of the modulator. Periodically loading uniform planar electrodes with capacitive elements such as fins and pads enables designer to simultaneously reduce S, and increase G. Moreover, the small gap, S, increases the electric field in the optical waveguide region. Figure 3.5 shows charge distribution on a typical slow wave electrode. This clearly illustrates the charge density variation on one period of a slow wave electrode. The maximum charge density occurs in the gap area where the distance between the signal and ground electrode is minimum. Therefore, it is expected that the horizontal and vertical components of electric field reach their maximum in the interelectrode gap and under the pad regions, respectively. Figure 3.6 and 3.7 show the quasi-static electric field components parallel and normal to the surface of the substrate, respectively. The results were obtained by quasi-static finite difference program developed in our lab. Therefore, the optical waveguide is positioned under the pads to exploit the vertical component of the electric field and between the pads to exploit the horizontal electric field component. Some experimental results will be presented on this subject.

This type of the structure enables us to design electrodes with small S and large G

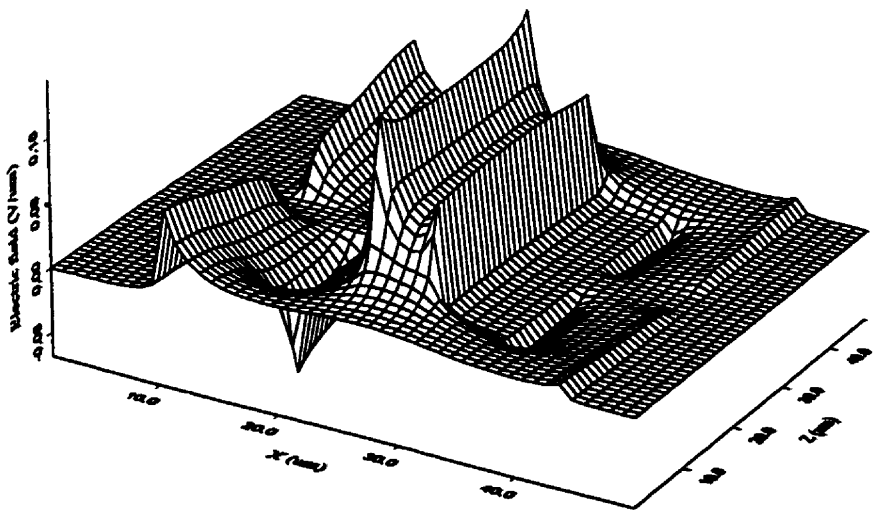

Figure 3.6 Electric field distribution of the component parallel to the substrate surface. The field is calculated at 0.5 μm below the substrate surface.

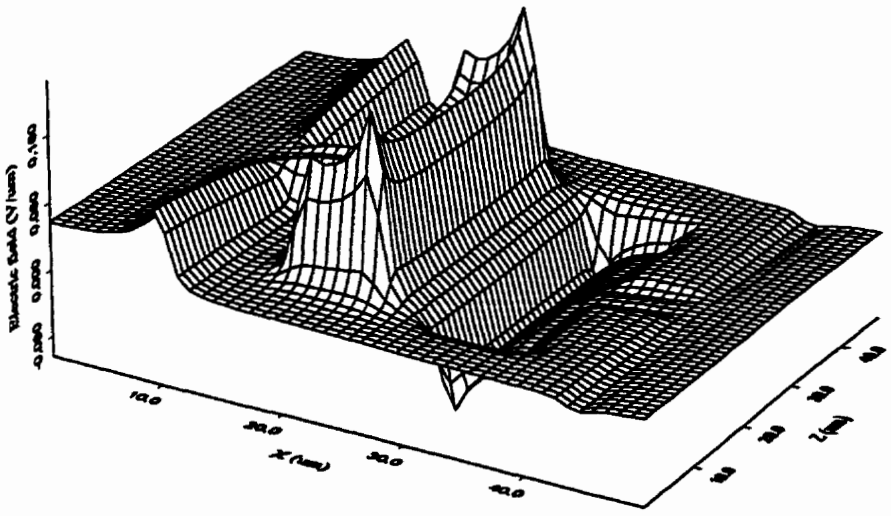

Figure 3.7 Electric field distribution of the component normal to the substrate surface. The field is calculated at 0.5 μm below the substrate surface.

to reduce the microwave loss and increase the electric field intensity in the area between and under the pads. Therefore, employing slow wave electrodes in high-speed electro-optic modulation serves the following purposes. a) velocity match, b) increasing electric field amplitude in the optical waveguide region, and c) reducing the microwave loss of the electrode.

According to the quasi-static approximation, the phase velocity of a microwave signal propagating along thin conventional coplanar waveguide electrodes over a semi-infinite substrate is constant, regardless of the waveguide dimensions. In this case, the effective dielectric constant is:

$$\varepsilon_{eff} = \frac{\varepsilon_r + 1}{2} \tag{3.6}$$

where ε_r is the dielectric constant of the substrate, SI-GaAs or SI-InP, (ε_r = 13.1 for GaAs). So, as mentioned earlier, the microwave phase velocity propagating along a uniform coplanar waveguide is $V_{ph(nl)} = c/\sqrt{\varepsilon_{eff}}$ = 11.3 cm/nsec. The capacitance and inductance of the slow wave structures can be calculated using the following standard transmission line equations:

$$C_{sw} = \frac{1}{Z_{nl} \cdot V_{ph(sw)}} \tag{3.7}$$

$$L = \frac{Z_{0l}}{V_{ph(sw)}} \tag{3.8}$$

where Z_{0l} is the characteristic impedance of the slow wave structure, 50 Ω, and $V_{ph(sw)}$ is the phase velocity of the slow wave structure, 8.5 cm/nsec.

The following procedure was used to estimate the initial values for the characteristic impedance of the uniform coplanar waveguide (before adding load fins and pads) and the load capacitance per unit length produced by the fins and pads for the first optical waveguide structure on GaAs. From Equations 3.7 and 3.8, C_{sw} is 0.2353 fF/μm and L is 0.5882 pH/μm. Since introducing narrow fins and pads to the conventional coplanar waveguides does not change the inductance per unit length of the line significantly, it can be assumed to be constant. The capacitance per unit length of the corresponding uniform coplanar waveguide is found to be $C_{nl} = 0.1331$ fF/μm, calculated from $V_{ph(nl)} = c / \sqrt{\varepsilon_{eff}} = 1 / \sqrt{LC_{nl}}$, where $V_{ph(nl)}$ is the microwave phase velocity propagating along the uniform coplanar waveguide, 11.3 cm/nsec. Therefore, the characteristic impedance of the uniform coplanar waveguide (before fins and pads are added) can be calculated as $Z_{0nl} = \sqrt{L / C_{nl}}$ which gives $Z_{0nl} \cong 66.5\ \Omega$.

In order to design the slow wave structure with the above parameters, one has to periodically load a uniform transmission line with characteristic impedance of 66.5 Ω with fins and pads of capacitance C_l. At frequencies of interest, where the periodicity, T_s, of the load capacitance, C_l, is much less than the electrical wavelength, i.e. $T_s << \lambda$, the loaded line behaves as an electrically smooth transmission line with a capacitance of $C_{sw} = C + C_l / T_s$. For $C = 0.1331$ fF/μm, the ratio C_l / T_s is calculated to be 0.1022 fF/μm. Then, for example for T_s equal 100 μm, $C_l = 10.22$ fF. The signal electrode width and the gap between the signal and ground electrodes of the uniform transmission line can be adjusted to the desired values while the characteristic impedance is kept constant at about 66 Ω.

The slow wave electrodes have been modeled and designed using a multilayered EM simulator for planar circuits [75]. This simulator does not allow the effects of optical ridge waveguides to be taken into account in the design model. The first generation of mask was initially used to estimate the effect of the presence of ridge waveguide under and between electrodes. Slow-wave electrodes were fabricated on SI-GaAs with and without ridges. The results were used to calculate the effect of ridges on the electrode responses. Therefore the subsequent masks were biased in the electrode design to accommodate for the ridge waveguides. The results will be presented in Chapter 5. Since *Sonnet* software considers metal electrode with zero thickness, the same procedure was also used to take into account the effect of nonzero thick metal electrodes. In the model, we have considered a 0.2 μm SiO_2 layer between the electrodes and GaAs substrate. The design goals were to achieve a phase velocity equal to that of optical signal, and characteristic impedance of 50 Ω for all the slow wave electrodes. The effects of the optical ridge waveguide and the 0.2 μm SiO_2 layer on the microwave performance of the slow wave structures are experimentally investigated. The results are presented in the next chapter. This simulator provides the *S*-parameters at a specific frequency for a given structure. It also provides the lumped circuit spice model for the structure under study. Transmission line parameters such as characteristic impedance, phase velocity, and microwave loss can be obtained from *S*-parameters as discussed below.

The ABCD matrix of the entire transmission line is expressed as a function of the s-parameters as follows [76] (see also appendix V):

$$\begin{bmatrix} A & B \\ C & D \end{bmatrix} = \begin{bmatrix} \dfrac{(1+s_{11})(1-s_{22})+s_{12}s_{21}}{2s_{21}} & Z_{0r}\dfrac{(1+s_{11})(1+s_{22})-s_{12}s_{21}}{2s_{21}} \\ \dfrac{1}{Z_{0r}}\dfrac{(1-s_{11})(1-s_{22})-s_{12}s_{21}}{2s_{21}} & \dfrac{(1-s_{11})(1+s_{22})+s_{12}s_{21}}{2s_{21}} \end{bmatrix} \tag{3.9}$$

where Z_{0r} is the reference characteristic impedance of the measuring system, 50 Ω. The characteristic impedance, Z_0, the propagation constant, γ, and the phase velocity, V_{ph}, of the CPW can thus be found using the following expressions:

$$Z_0 = \frac{2B}{D - A \pm \sqrt{(A+D)^2 - 4}} \tag{3.10}$$

$$\gamma = \alpha_m + j\beta_m = \frac{1}{l}\left[\left(\frac{A+D}{2}\right) \pm \sqrt{\left(\frac{A+D}{2}\right)^2 - 1}\right] \tag{3.11}$$

$$V_{ph} = \frac{2\pi f}{\beta_m} \tag{3.12}$$

where l is the length of the transmission line, α_m is the attenuation constant (Np/unit length), and β_m is the phase constant (rad/unit length) of the transmission line. Equations 3.10 and 3.11 yield two solutions for both Z_0 and γ. The physically meaningful value of Z_0 has a positive real part and the physically meaningful value of γ has a positive α_m. The positive value for α_m translates into a real loss in the transmission line.

3.3 Slow Wave Electro-Optic Modulator Design

Three sets of masks, LIT-1, LIT-2, and LIT-3, with different possible configurations of slow wave electrodes and optical structures suitable for electro-optic modulators were designed and fabricated. The layouts of the coplanar waveguides (CPW) and coplanar strips (CPS) and optical structure under study are given in Appendix I.

In LIT-1, five different kinds of coplanar waveguide structures, CPW, CPWA, CPWB, CPWC, and CPWD, with various design variations provide a total of 30 distinct coplanar waveguide structures. The design goal for LIT-1 consists of a characteristic impedance of 50 Ω and a phase velocity of 8.9 cm/nsec or effective index of 3.37 which was the effective index of an in-stock wafer. Due to the poor quality of the wafer for which the masks had been designed for, including highly carbon contamination in all epitaxial, no guided optical signal could be observed. This set of mask consists of four

layers, including first level of metal (FLME), air-bridge via, air-bridge metal, and waveguide. The last layer contains different optical structure. The first three layers are used to pattern the slow wave electrodes. The purpose of using air-bridge via and air-bridge metal layers was to increase the thickness of the signal and ground electrodes and therefore to reduce the microwave loss due to metallization. This mask was mainly used to evaluate the microwave performance of the different slow wave electrodes. The measurement results using this mask were used in the design of second set of masks.

The second set of mask, LIT-2, consists of two different coplanar strips, CPSD, and CPSD-id, and three different coplanar waveguides, CPW, CPWD, CPWD-as for a total of 24 electrodes. The electrodes on LIT-2 mask sets were designed to have a characteristic impedance of 50 Ω and a phase velocity of 8.606 cm/nsec, which is the group velocity of the optical signal in the optical structure shown in Figure 3.1. All the slow wave electrodes on this mask were loaded using T-rail capacitive elements which enables the designer to achieve higher longitudinal overlap factor with smaller interelectrode gap. Interelectrode gaps are 3, 4, 5 μm and longitudinal overlap factor, Γ_l, as high as 80% was obtained. Coplanar strip electrodes offer higher Γ_l for the same load capacitance over coplanar waveguide electrodes due to the introduction of smaller amount of capacitance per unit length. This can be compensated partially by making an asymmetric version of coplanar waveguide, CPWD. In an asymmetric Coplanar waveguide, CPWD-as, the length of the fins and pads extending from the signal electrodes is shorter than the length of the fins and pads extending from the ground electrodes, $L_{ss}<L_{sg}$. The asymmetric capacitive elements offer smaller capacitance than the symmetric element with the same gap, S. LIT-2 consists of two layers of mask, first level of metal and waveguide.

The design tendency in the three sets of masks was to reduce the interelectrode gap, S, reduce the optical mode size, increase the overlap factor between the optical and microwave signals and increase the longitudinal overlap factor, Γ_l, that result in lower modulation voltage. These issues were accommodated in the third design by further reducing the width of the fins and pads, W_s and l_p, and also increasing the periodicity, T_s.

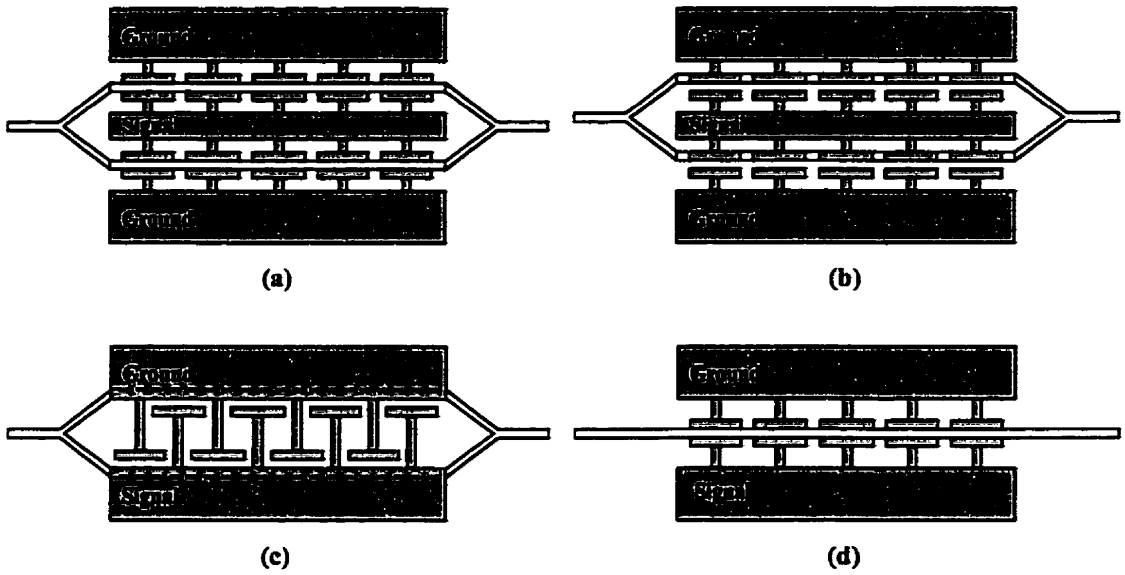

Figure 3.8 Layout of electro-optic modulators, slow wave electrodes integrated with optical structures. (a) optical waveguides placed between the pads of CPW slow wave electrodes. (b) optical waveguides placed under the pads of the signal and ground electrodes of CPW slow wave structure. (c) optical waveguides are under the inner edge of the signal and ground electrodes of an interdigitated CPS slow wave structure. (d) electrodes of a slow wave CPS are on either side of an straight optical waveguide.

W_s and l_s are as small as 2 μm and the periodicity is 100 μm. This enabled us to design slow wave electrodes with gap, S, of 2.5 μm and Γ_l of as high as 96% without overslowing the microwave signal. The width of the optical ridge waveguide is 2 and 2.5 μm. In this design, all coplanar waveguides are of CPWD-as type. Fabrication process in the Microelectronic facility at Communications research centre (CRC) requires minimum electrode width and gap of 2 μm. Fabrication of slow wave electrodes with extreme large and small dimensions on the same mask poses the problem of over or under developing some parts of the mask. Normally the fins and pads width, W_s and l_s, are over-developed and therefore the resultant gap, S, is smaller than the designed value. This results in higher load capacitance and overslowing the microwave signal. LIT-3 has been designed to compensate this problem. This mask has also two layers.

All masks fabricated using E-Beam fabrication process with 0.1 μm writing address and 0.5 μm defect inspection. The physical dimensions of the designed electrodes and optical structures are given in Appendix II. Figure 3.8 all electro-optic modulator

configurations studied on the three sets of mask when a slow wave electrode is integrated with an optical structure. CPWD in Figure 3.8(a) and (b) can be replaced with all other CPWs to generate all configurations.

Interdigitated electrodes have already been used extensively in other applications [77]. Here, a slight modification to the conventional interdigitated electrodes is proposed. This design will enhance the performance of the electro-optic modulators that normally require long effective interaction length and small gap to reduce the modulation voltage. Besides, this is the only configuration that a coplanar strip (CPS) electrode loaded with T-railed capacitive elements can be integrated with MZI.

3.4 Discussion

In this section, we have discussed the design issues of heterostructure epitaxial layers, ridge optical waveguide, and coplanar slow wave electrodes.

Two optical structures were designed for to be employed in two generations of traveling wave electro-optic modulators. We also presented new techniques in the design of heterostructure epitaxial layers to modify the optical mode tail, reduce the thickness of top and bottom cladding layers suitable for traveling wave electro-optic modulations and also other applications that require mode tail engineering. Different slow wave electrode configurations were presented to be integrated with optical structures. Three sets of masks have been designed that consists different combinations of slow wave electrodes with optical structures.

In the next chapter, we will discuss the characterization techniques that have been applied for the fabrications of slow wave electro-optic modulators. We will also present the fabrication process and measurement techniques that were used in this work.

CHAPTER 4

Characterization, Fabrication, and Measurement Techniques

The quality of a product in general and of an integrated electro-optical device in particular depends on the quality of the materials and fabrication process used. This chapter describes the techniques that were used to characterize the epitaxial optical structures to be used in the fabrication of the traveling wave electro-optic modulators. Then it proceeds with the fabrication process of these devices.

Finally, we will present the measurement techniques to evaluate the performance of the traveling electro-optic modulators. It includes the techniques to measure the optical waveguide loss, to evaluate polarization sensitive and insensitive Mach-Zehnder modulator and polarization/mode converter.

4.1 Material Characterization

The improvement of growth techniques for semiconductor structures, such as liquid phase epitaxy (LPE), molecular beam epitaxy (MBE), and metal-organic chemical vapor deposition (MOCVD), have been of crucial importance for the improvement of III-V semiconductor technology. Especially for optoelectronic integrated circuits (OEIC), where both the electric and optical properties have to be optimized, high quality material is a prerequisite for high quality components. Special characterization techniques have therefore been used to determine the material properties of the heterostructure epitaxial optical layers. From all the existing III-V semiconductor characterization techniques, we only describe the ones that were used to characterize the wafer on which the modulators were fabricated.

4.1.1 Photoluminescence Technique

Photoluminescence is a very powerful technique to characterize the quality of the semiconductor materials such as GaAs/AlGaAs epitaxial layers. Photoluminescence (PL) is the optical radiation emitted by a physical system resulting from excitation to a nonequilibrium state. The radiative transition originates on some excited electronic state, and after the emission of a photon (radiative recombination), a lower electronic level is occupied. The photon wavelength is $\lambda(\mu m) = hc/\Delta E = 1.24 / \Delta E$ where ΔE is the transition energy of the excited atom to a lower energy level in eV. The spectral distribution of these emitted photons shows a peak around the fundamental bandgap energy. Figure 4.1 shows the schematic diagram of the system that was used.

The pump light is a He-Ne laser source at a power level of about 50-100 mW. Then the light filtered by a bandpass filter and then divided by a splitter. Part of the light is passed through a chopper at 400 Hz used for lock-in detection of the luminescence signal. The light is then focused on the sample to be analyzed. The sample is kept at 10° K to reduce the strong background noise and therefore increase the signal to noise ratio.

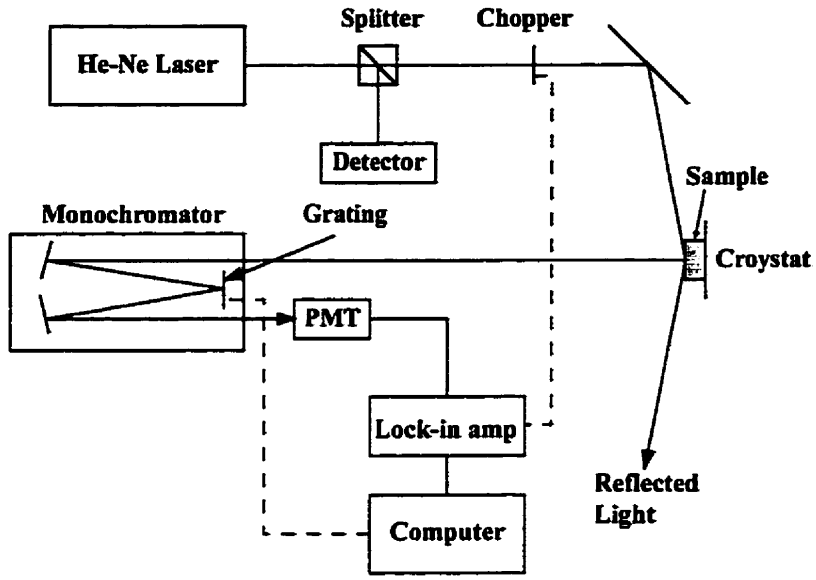

Figure 4.1 Schematic diagram of a photoluminescence measurement setup.

There is a grating in the monochromator whose angle is controlled by the computer. The output of the monochromator is then the light at different wavelengths that is amplified by a photomultiplier tube (PMT). The signal to noise is generally very low, and therefore the chopped pump and the lock-in technique are used to extract the very weak signal from the strong noise. Figure 4.2 shows the measured photoluminescence spectrum of an in-stock GaAs/AlGaAs sample for which the LIT-1 set of masks was designed.

The position of the maximum corresponds to the fundamental bandgap energy and the full width at half maximum gives an indication of the quality of the material. PL measurements carried out over the whole wafer surface are used to determine the uniformity of the epitaxial layers. In the measurement shown here, the peak at 830 nm corresponds to GaAs and the peak at 817 nm does correspond to carbon. It clearly shows that the sample was heavily contaminated by carbon most probably during the layer growth. This high level of carbon contamination changes the crystal properties and refractive index of the material. The sample was tested for optical guiding and no optical waveguide could be established using this substrate. Therefore, this sample could not be used for any electro-optical measurements or even simple optical loss measurement.

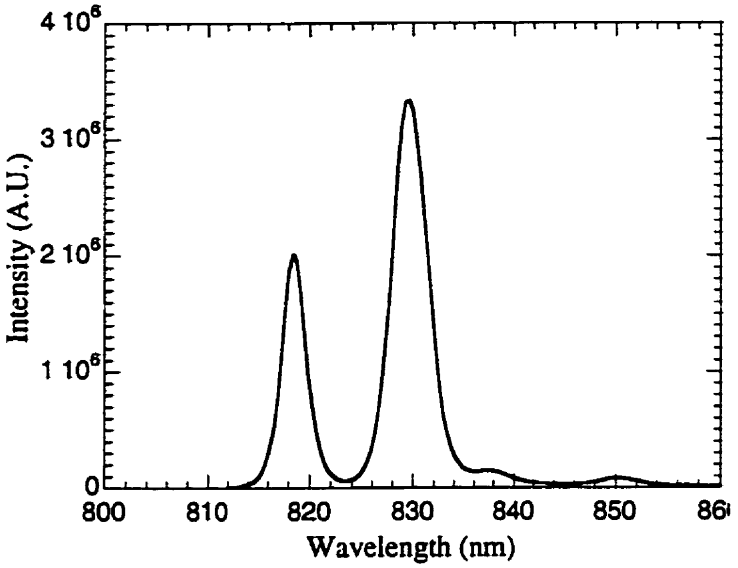

Figure 4.2 Photoluminescence spectrum of an in stock GaAs/AlGaAs substrate.

4.1.2 Capacitance-Voltage Technique

The capacitance-voltage or (CV) technique is used to determine the carrier concentration depth profiles in semiconductor materials with a measurement range of approximately 10^{15}-10^{19} cm^{-3}. The profile can, in principal, be measured to unlimited depth by using etch steps in between the measurements. Figure 4.3 shows a schematic diagram of the core of the CV-profiler used to study the doping profile of semiconductor materials in this research.

This teflon cell is filled with an electrolyte containing positive and negative ions. The test sample is brought in contact with the electrolyte. This electrolyte-semiconductor interface can be described in a similar way as the *pn*-junction. Provided that the electrolyte is fairly concentrated, the depletion of the electrolyte is negligible and the depth x_d of the depleted semiconductor layers can be expressed as:

$$x_d = \left(\frac{2\varepsilon_0 \varepsilon_r (V_0 - V)}{eN} \right)^{\frac{1}{2}} \tag{4.1}$$

where the V_0 is the built-in potential between the electrolyte-semiconductor interface, V is the applied voltage, N and ε_r are the carrier concentration and dielectric constant of the

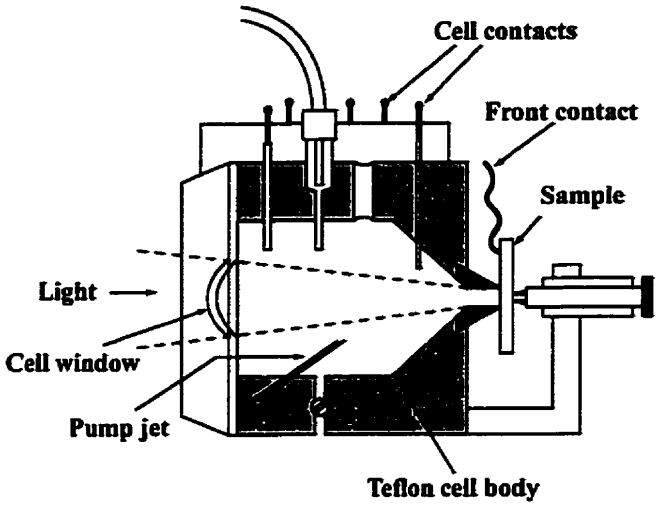

Figure 4.3 Schematic diagram of the electrochemical (teflon) cell of a CV-profiler.

semiconductor sample, respectively. Typical values of the depletion depth x_d at reverse bias of 1 V are about 1, 0.1, and 0.01 μm for carrier concentration of 10^{15}, 10^{17}, 10^{19} cm^{-3}, respectively. The depletion depth can also be given as:

$$x_d = \frac{\varepsilon_0 \varepsilon_r A}{C} \tag{4.2}$$

where A is the contact area between the semiconductor and electrolyte, and C is the small signal capacitance of the depleted layer. From this equation, it follows that the average carrier concentration within a depletion layer can be determined via a simple capacitance measurement. In fact this is what the CV-profiler does. The CV-profiler modulates the reverse bias voltage by an AC signal, normally 0.14 V_{p-p} at 40 Hz, to measure the small signal capacitance of the depleted region. The carrier concentration in the depleted layers can be obtained from the above equations as given by:

$$N(x_e - x_d) = -\frac{C^3}{e\varepsilon A^2}\left(\frac{1}{\frac{dC}{dV}}\right) \tag{4.3}$$

where x_e is the etch depth, e is the elementary charge, and $\Delta C/\Delta V$ is the differential capacitance measured at a given frequency and modulating signal. In between the carrier concentration measurements, a thin layer of semiconductor is etched away. The etch

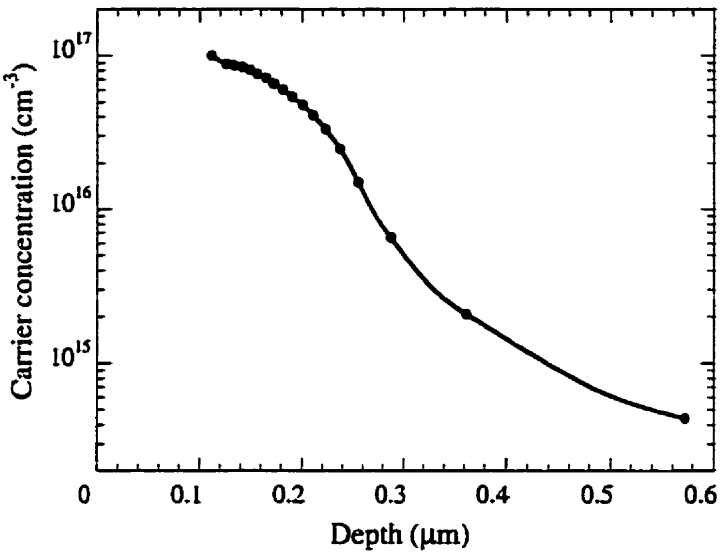

Figure 4.4 Carrier concentration profile of a GaAs substrate implanted with Si_{29}.

depth is calculated via Faraday's law of electrolysis for the total charge transfer by integrating the etch current I_e.

Figure 4.4 shows an example of the carrier density profile of an ion implanted semi-insulating GaAs substrate. The substrate is implanted with Si_{29} at 120 KeV with a dosage of 2.33×10^{12} cm^{-2}.

4.2 Fabrication Process

In addition to the design, the performance of a traveling wave electro-optic modulator strongly depends on the fabrication process. The performance of these devices vary as a function of ridge height and width, interelectrode gap, relative position of the electrode and ridge including a relative angle between the optical waveguide and the electrode. Some of the problems that may occur during fabrication are illustrated in Figure 4.5. Variation in the ridge width and height affects the single mode propagation as well as the optical mode size and the modulation voltage. Special attention must be paid during fabrication to maintain all device parameters the same over its long length ($\geq$ 1 cm) and to minimize any degradation from the design values.

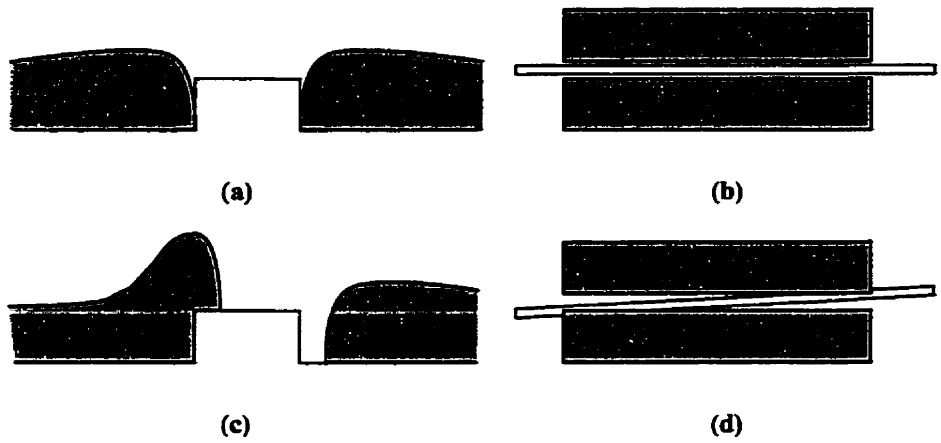

Figure 4.5 Schematic diagram of ridge waveguide and electrode in different situations. (a) and (b) show the ideal cases and (c) and (d) are the corresponding potential problems.

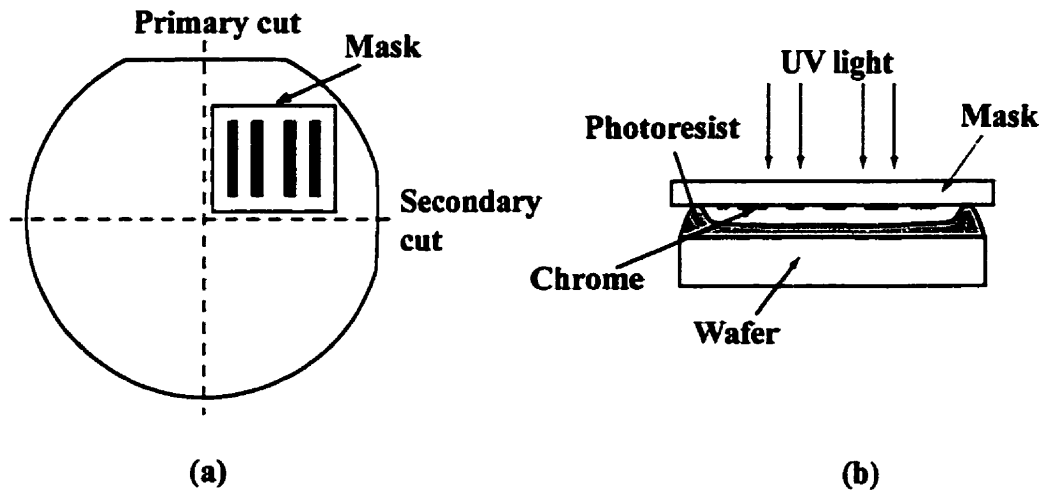

Figure 4.6 (a) Relative size and position of the mask and 3" wafer. (b) cross section of the wafer during standard lithography.

The modulators were fabricated on quarters of 3" wafers using standard lithography. The wafers are [100] flat substrates. The electrodes and optical waveguides (direction of propagation) are perpendicular to the primary flat, $[0\bar{1}1]$ direction. The digitized area of the mask is almost 25×25 mm^2. The relative mask size and its position on a quarter of a 3" wafer is given in Figure 4.6 (a). Due to the photoresist built-up on the wafer edges, a margin of least 2 mm on all sides of the wafer was left. Therefore the devices are fabricated in the centre of the wafer where the photoresist is uniform. The

other problem that may arise from nonuniform photoresist on the wafer is illustrated in Figure 4.6 (b). The quality of the edges of the ridge optical waveguide is mainly determined by the airgap between the mask and photoresist. This airgap causes the diffraction of the UV light, which reduces the sharpness of the ridge optical waveguides. To define the mask pattern, a layer of photoresist is spin coated on the sample. The thickness can be chosen by controlling the rotation speed of the rotating plate. The resist is developed by bringing the chrome side of the mask in close contact with the sample and illuminating it by ultraviolet light for 10 Seconds. Then depending upon positive or negative photoresist, the exposed or masked areas will be solved in the solvent, respectively.

The following is a brief description of the fabrication process performed at the Microelectronic facility of Communications Research Centre (CRC). First, the sample is standard cleaned. Then the sample is coated with a thin layer of positive photoresist, 2 μm. Next, lithography of the resist is carried out using the waveguide (WAGD) mask. Then, ridge optical waveguides are defined by reactive ion etching (RIE) of the wafer for a specific depth, 0.9 μm for LIT-1 and 0.25 μm for LIT-2 mask set. The sample is then coated with a SiO_2 layer of 0.2 μm using plasma deposition. This layer is intended to reduce the optical loss due to proximity to electrode metallization. The sample is again spin coated with the positive photoresist and the same procedure is performed to define electrode (FLME) mask pattern into the resist. Titanium (Ti), Platinum (Pt) and gold (Au) are evaporated on the sample and then a standard lift-off technique is used remove the photoresist and the metal. Ti is being used for adhesion to the semiconductor substrate. Due to large ridge height in LIT-1 design, 0.9 μm, the metal electrode has to be thick enough to keep the electrode continuity on the ridge. This forced us to choose metal thickness of 1.5 μm that consist of 0.2 μm of Ti, 0.3 μm of Pt and 1 μm of Au. In LIT-2 design, the ridge height is 0.25 μm and therefore the metal electrode could be thinner. The metal in this design consists of 0.1 μm of Ti and 0.9 μm of Au. The basic building blocks of the fabrication process of the traveling wave modulator is illustrated in Figure 4.7.

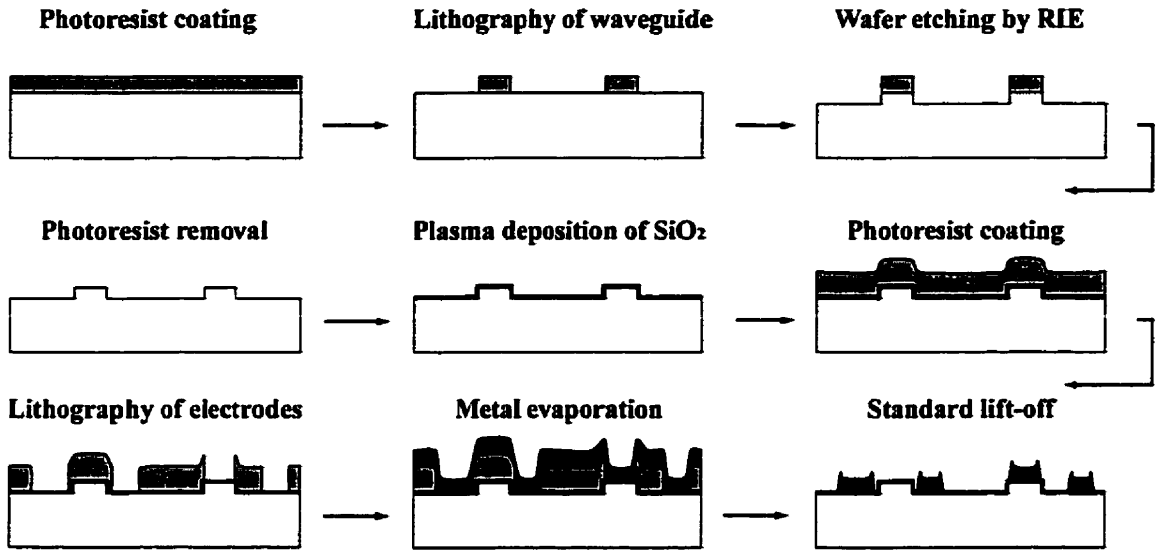

Figure 4.7 Cross section of a mode converter and a phase modulator during the fabrication process steps. Dark area is SiO_2, dark gray is metal, and light gray is photoresist.

Figure 4.8 SEM photograph of the cross section of a ridge optical waveguide.

Figures 4.8 and 4.9 are the SEM photograph of the cross section of a ridge optical waveguide and an its position in an interdigitated coplanar strip MZ modulator. The roughness on the sidewalls of the ridge optical waveguide, caused by RIE, is visible in the former. This causes an increase in the optical loss due to scattering. In the later, the need to have a relatively thick metal electrode to maintain the electrode continuity for

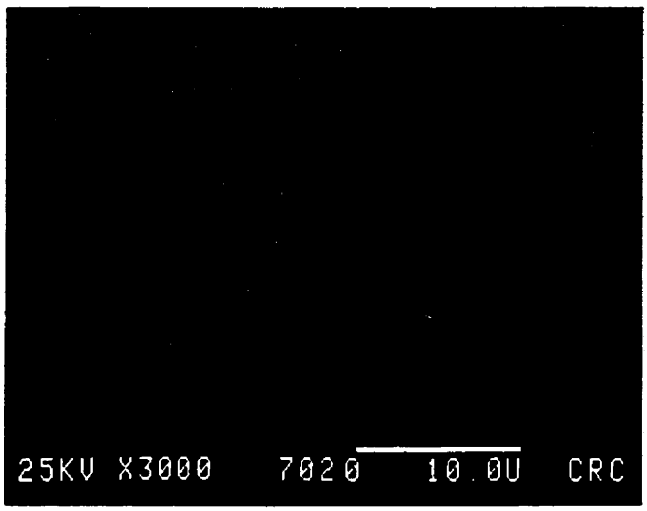

Figure 4.9 SEM photograph of the cross section of an interdigitated MZ modulator showing optical waveguides under the inner edge of the main signal and ground electrodes.

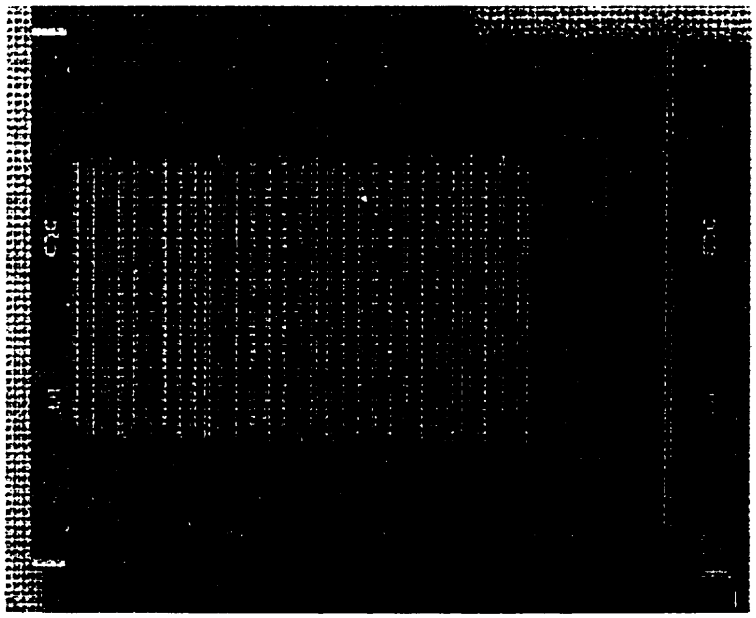

Figure 4.10 Photograph of the GaAs/AlGaAs chip fabricated using LIT-1 mask set.

devices in which the ridge optical waveguide is positioned under the electrode is evident. The electrode has to be thicker than the ridge height to satisfy that requirement. Finally, a fabricated GaAs substrate chip using LIT-2 set of masks is given in Figure 4.10.

4.2.1 Self-Align Technique

This technique was developed to enhance the performance of the polarization/mode converters and polarization insensitive MZ modulators which exploit the electric field component parallel to the surface of the [100] flat substrate. In these devices the optical waveguide is positioned between the electrodes. The ideal case is to have the electrode right to the side-walls of the ridge optical waveguide as illustrated in Figure 4.5(a). Electric field intensity in the substrate, E_s, and ridge, E_r, regions is much higher than the electric field in the air, E_a, due to the higher dielectric constant of the substrate. Since a major part of the optical mode tail still exist in the ridge region, the electric field in that area, E_r, has a significant effect on the half wave voltage of the modulator. If there is an air gap between the electrode and the ridge side walls, the electric field intensity significantly drops in the ridge region, see Figure 4.11(a). This, in turn, reduces the half wave voltage of the modulator. Figure 4.11(b) shows an equivalent circuit for the ridge optical waveguide with the electrodes on either sides. C_s and C_a represent the capacitance in the substrate and air, respectively. The capacitance due to E_r is represented by a series of three capacitors, C_{ag} for air gap and C_r for ridge region. If V is the applied voltage across the electrodes, the voltage drop across the ridge optical waveguide, V_d, is given as:

$$\frac{V_r}{V} = \frac{1}{1 + 2\varepsilon_r\left(\frac{a}{d}\right)} \tag{4.4}$$

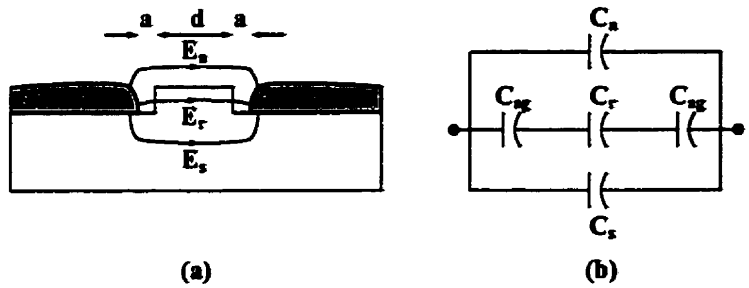

Figure 4.11 (a) Simplified electric field distribution in a ridge waveguide with an airgap between the electrode and the ridge. (b) the simple equivalent circuit model.

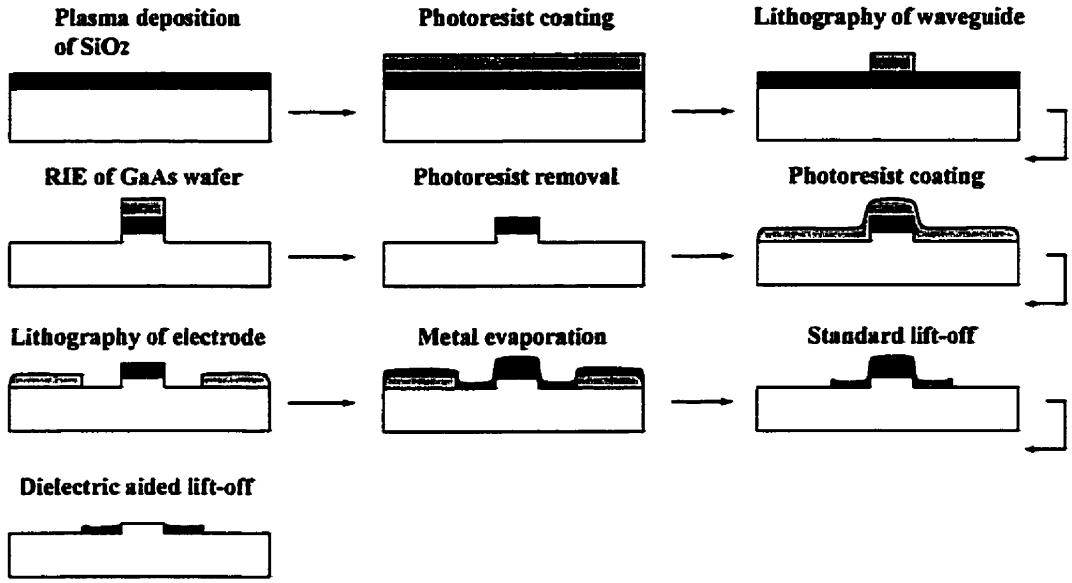

Figure 4.12 Cross-section of a mode converter during the steps of self-align fabrication process. Dark area is SiO_2, dark gray is metal, and light gray is photoresist.

where ε_r is the substrate dielectric constant (13.1 for GaAs), a is the air gap, d is the ridge width. This equation shows how fast the electric field in the ridge region drops as the air gap increases. The electric field is also a strong function of the dielectric constant of the substrate. For example, for $\varepsilon_r(a/d)$ of 1, V_d/V is equal to 0.33. Therefore, 66% of the available electric field is dropped across the air gap that does not have any contribution to modulation. This translates to an air gap to ridge width ratio of about 7.6%. Maintaining the ratio of a/d to 0.076, the voltage drop across airgaps is only 10% of the applied voltage for glass substrate ($\varepsilon_r = 1.5$). Therefore, traveling wave modulators on substrate with high dielectric constant have to be designed with no or minimum possible air gap between the side electrodes and the ridge optical waveguide.

A self-align technique was developed to fabricate the mode converter and polarization independent MZ modulators with no air gap. Figure 4.12 illustrates the most important steps in the fabrication process. The only modification to be made to the FLME mask is that the interelectrode gap is part of the digitized data. This process is very similar to the fabrication process described earlier in this section with the exception that there is a dielectric assisted lift-off. The GaAs sample is deposited with a layer of SiO_2

using plasma deposition. Then it is spin coated with a 2 μm thick positive photoresist layer. The optical waveguides are defined using standard lithography technique that is followed by a RIE of dielectric and GaAs materials to the specific depth. Next the residual photoresist is removed and then again covered by another layer of photoresist. Lithography of the electrode is followed by metal evaporation of 1 μm thickness. Using a standard lift-off technique the metal electrode is defined on the GaAs substrate with the ridge optical waveguide covered by metal. To open the interelectrode gap, the metal on top of the ridge is removed using a dielectric aided lift-off technique. This process assures that the metal electrodes are in close contact with the side-walls of the ridge waveguide and there is symmetrically placed on either side of the ridge.

Figure 4.13 and 4.14 illustrate the SEM photographs of the cross section of the optical waveguide before and after the final step of dielectric assisted lift-off. As seen in these Figures, the electrodes are in a very contact with the side-walls of the optical waveguide. This method practically eliminates the problem of angular misalignment as shown in Figure 4.5(d).

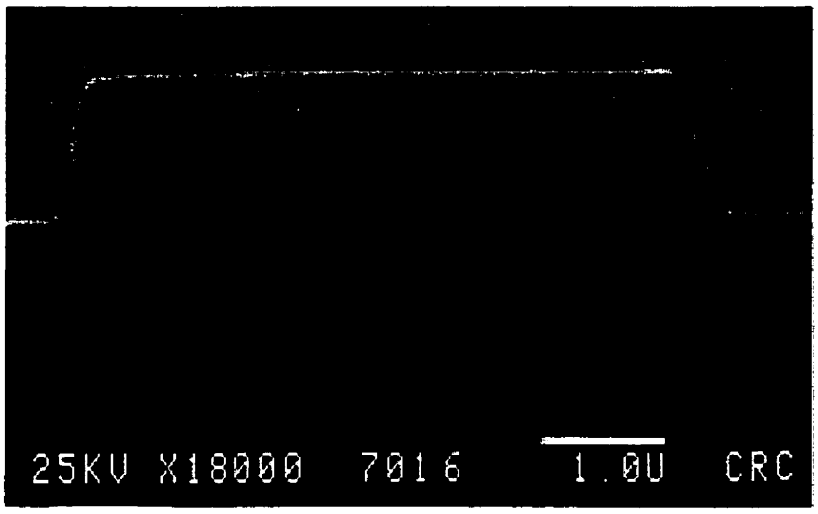

Figure 4.13 SEM photograph of the cross section of an optical waveguide of a mode converter using self-align fabrication process before dielectric assisted lift-off.

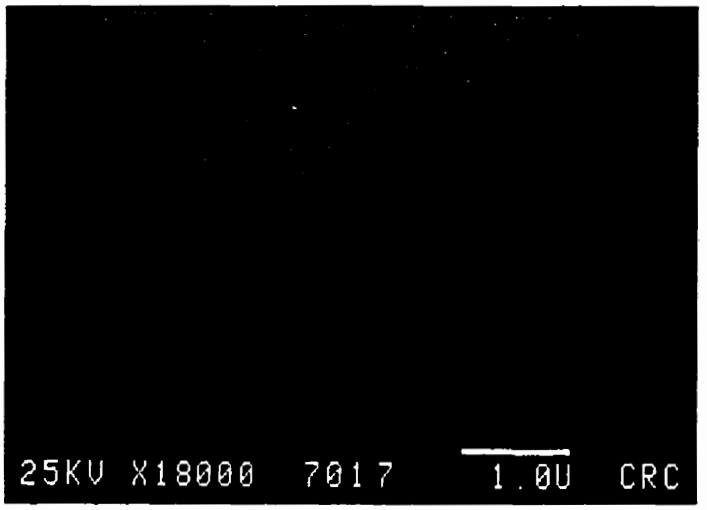

Figure 4.14 SEM photograph of the cross section of an optical waveguide of a mode converter using self-align fabrication process after dielectric assisted lift-off step.

4.3 Measurement Techniques

In this section, the techniques and setups that were used to measure the microwave, optic and electro-optic performance of the traveling wave electro-optic modulators are described. These devices have to be characterized from almost DC to very high frequency. Low frequency measurement consists of low frequency transfer function of the device. High frequency measurements are used to obtain the modulation spectrum of the modulator and possibly the 3- dB roll-off in the modulation response. Optical loss per unit length is also required to evaluate the on-chip loss. The other parameter of interest is the coupling loss between the single mode optical fiber and the semiconductor optical waveguide.

4.3.1 Optical Measurement

Optical loss measurement is a very delicate and time-consuming experiment especially for low loss optical waveguide. The most important source of error in this

experiment is the coupling in and out of the fiber. There are mainly two techniques to measure the optical loss of the semiconductor waveguides.

The first technique is called cut-back technique which is a destructive method. In this method, the optical waveguide is cut into pieces with different length. For a given and constant optical source, the optical signal power is measured at the output of each waveguide. The optical output power is a linear function of the waveguide length provided that the input and output coupling are maintained the same for all pieces. This assumption introduces some error into the calculations. To minimize this error, the goal has to be to maximize the output optical power by fine tuning the fiber position relative to the waveguide. This technique can also provide the coupling loss between the fiber and optical waveguide. The slope of the measured data with respect to the waveguide length provides the loss per unit length of the waveguide.

Fabry-Perot cavity method is a nondestructive technique that calculates the optical loss of the waveguide using the characteristic of the cavity created with the optical waveguide and its end-facets [78]-[79]. Figure 4.15 shows the building blocks of the measurement setup. A tunable laser is used to sweep the optical wavelength and the output power is measured as a function of wavelength. The optical signal is launched to and collected from the waveguide using tapered fiber. Due to the internal reflection, in the cavity, an interference pattern is created at the waveguide output. The maximum and minimum of this interference pattern is utilized to calculate the optical loss of the

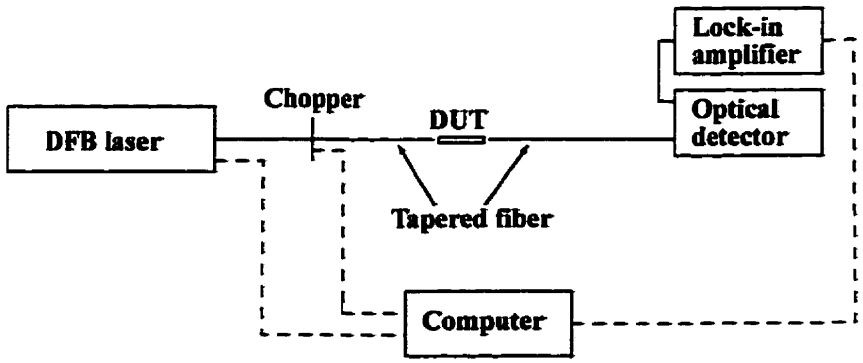

Figure 4.15 Schematic diagram of the optical loss measurement using Fabry-Perot technique.

waveguide. In this experiment, it is assumed that the end-facets of the waveguides are perfectly flat. The samples have to be thinned down to about less than 150 μm to achieve a cavity with practically flat end-facets. Any degradation from this assumption introduces additional error to the loss measurements. The other source of error is the cavity interference in the air cavity between the fiber and the waveguide. Using tapered fiber reduces this error to some extent. Under a perfect cavity assumption, the loss per unit length of a waveguide is calculated from:

$$\alpha = \frac{8.686}{2l} \ln\left(R \frac{\sqrt{I^t + 1}}{\sqrt{I^t - 1}} \right) \tag{4.5}$$

where l is the length of the optical waveguide, R is the reflectivity of the cavity facets, $I^t = I^t_{max} / I^t_{min}$, and I^t_{max} and I^t_{min} are the maximal and minimal of the interference pattern at the waveguide output, respectively. In addition to the sources of error mentioned earlier, this measurement technique is sensitive to the length of the sample. Theoretically, the measurement is less sensitive for longer samples. On the other side, the interference pattern is denser for long samples which causes practical limitations in terms of wavelength accuracy. For short samples, some optical power might be detected directly through air. We selected optical waveguide length between 2 and 10 mm. The error in our measurement was estimated to be ±0.3 dB.

4.3.2 High Frequency Measurement

The first step in the characterization of the traveling wave electro-optic modulators is the s-parameter measurement of the electrodes. S-parameters can be used to extract the phase velocity of microwave signal, microwave insertion loss, and characteristic impedance of the slow wave electrode. This measurement was performed using an HP8510C network analyzer and a Cascade Probe station.

The schematic layout of the measurement setup is depicted in Figure 4.16. This setup was used to measure the modulation spectrum of the traveling wave electro-optic modulators. A DFB laser at 1553 nm wavelength with linewidth of less than 0.08 nm is

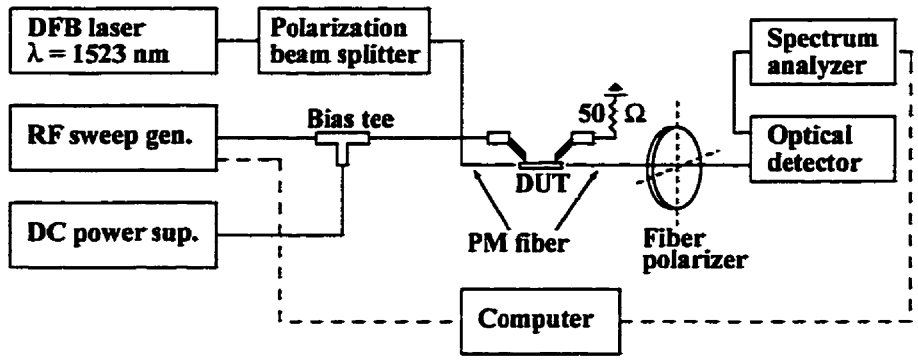

Figure 4.16 Block diagram of the system used in the high-speed modulation measurement.

used as the laser source. The laser output power is about 7.5 dB_m. The optical signal is but-coupled into the input optical waveguide with a polarization maintaining (PM) single mode fiber whose slow and fast axis are parallel and normal to the substrate flat, respectively. The polarization extinction ratio at the output of the beam splitter is over 18 dB. This enables us to evaluate the performance of the device under test (DUT) for both states of polarization and characterize its polarization insensitivity. The output optical signal is collected with another PM fiber with its axis along parallel to the axis of the input PM fiber. The polarization beam splitter is used in combination with mode converter to transform the mode conversion into intensity modulation. This device is not needed for the measurement of MZ intensity modulators and is removed. In this case, the output PM fiber can also be replaced with a standard single mode fiber.

An HP70951B optical spectrum analyzer along an HP70810B lightwave section is used as the optical detector. The HP70951B optical spectrum analyzer has a range of 600-1700 nm with 0.08 nm resolution. The HP70810B lightwave section, an amplified optical detector, has the ability to detect both DC optical signal and modulated signal from 100 KHz to 22 GHz. The frequency response after 20 GHz is questionable. The frequency response is not calibrated and has to be corrected by a correction factor. The maximum frequency of operation for this setup is limited by the bandwidth of optical detector. The RF sweep generator consists of HP8350A sweep oscillator with HP83594A RF plug-in that provide a frequency range of 2-26.5 GHz. As shown in Figure 4.16, the output of the optical detector is given to a spectrum analyzer to display the modulation

spectrum as a function of frequency. An HP8565E spectrum analyzer with frequency range of 30 Hz to 50 GHz was used for this purpose.

Two picoprobes, by GGB Industries Inc., were used to apply the RF signal to the modulators under test. The probes demonstrate a maximum insertion loss of less than 1 dB at 40 GHz and return loss in excess of 20 dB all over frequency range. This correction factor has also to be considered in the calibration of the modulation spectrum. Another correction factor that has to be taken into account is the frequency response of the bias tee and the cables.

The transfer functions of the modulators were measured by applying a 5-50 KHz ramp signal. An amplified photodetector, AD-300/DC-FC, with a frequency range of DC-2.5 GHZ and conversion gain of over 200 V/W was used to measure the low frequency modulation. An oscilloscope displayed the transfer function of the modulator.

4.3.3 Heterodyne Measurement Technique

As mentioned in the last subsection, the conventional method of measuring modulation spectrum of the modulator is limited by the photodetector bandwidth. This bandwidth was 20 GHz. Heterodyne method is an appropriate way to enhance the bandwidth of the measurement setup [80]. A block diagram for this technique is given in Figure 4.17. A tunable laser is used to down-convert the modulation frequency so that it falls into the photodetector bandwidth. The modulated optical signal (E_1) is combined with the signal of a tunable laser (E_2) with slightly different wavelength. These signals are detected by a photodetector (nonlinear device) to generate different harmonics. The detector output is then amplified and passed to the spectrum analyzer. Signals at the input of the combiner in Figure 4.17 are represented as:

$$E_1 = E_{10} Cos(\varphi_m(t)) Cos(\omega_1 t) \tag{4.6}$$

$$E_2 = E_{20} Cos(\omega_2 t + \Delta\phi) \tag{4.7}$$

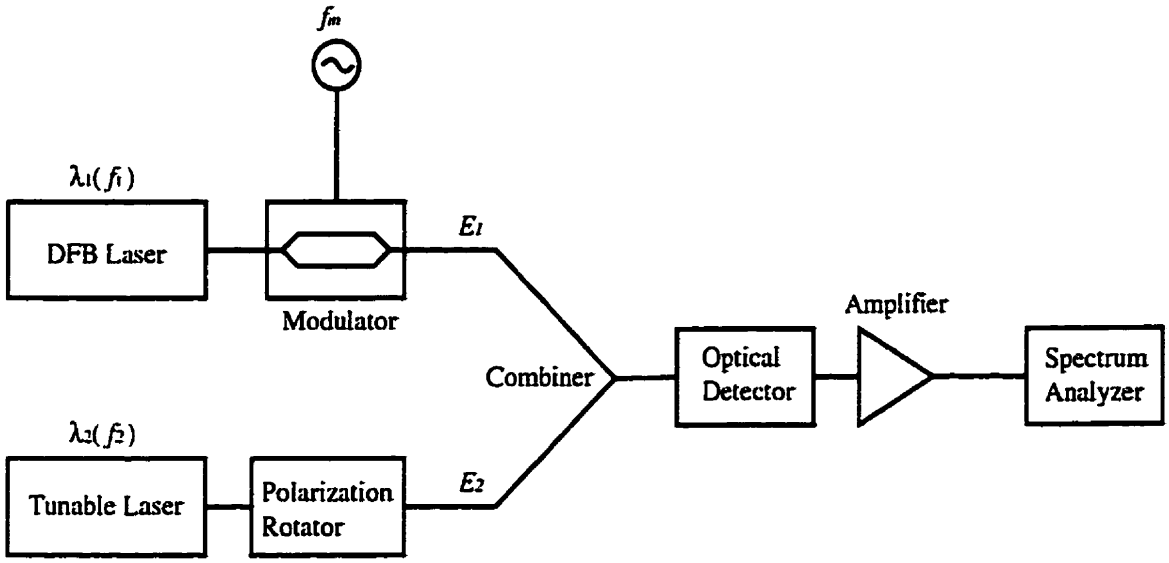

Figure 4.17 Block diagram for heterodyne measurement technique.

where ω_1 (= c/λ_1) and ω_2 (= c/λ_2) are the frequency of DFB laser and tunable laser, respectively, $\Delta\phi$ is the phase difference, and $\varphi_m(t)$ is the modulating signal, biased on the linear part of the transfer function, represented as:

$$\varphi_m(t) = \frac{\pi}{4} + KCos(\omega_m t) \tag{4.8}$$

ω_m is the modulation frequency, and K is the modulation index. The power of the modulated optical signal is:

$$P_1(t) = \frac{1}{2} P_{01}\left(1 - Sin(2KCos(\omega_m t))\right) \tag{4.9}$$

where P_{01} is the CW power of DFB laser at the output of the modulator. The total power at the input of the optical detector depends upon the angle between the polarization states of two incoming signals (ϕ_p) and is given by:

$$P_{opt}(t) = P_1(t) + P_2 + 2\sqrt{P_1(t)P_2}Cos(\Delta\omega t + \Delta\phi)Cos(\phi_p) \tag{4.10}$$

where P_2 is the CW power of tunable laser source, and $\Delta\omega$ is the beat frequency between the two laser source. ϕ_p was adjusted using polarization rotator to maximize total optical power. The following assumptions were made to simplify the output current of the photodetector

$$Cos(KCos(\omega_m t)) \approx 1 \tag{4.11}$$

$$Sin(KCos(\omega_m t)) \approx KCos(\omega_m t) \tag{4.12}$$

which means that the modulation index was very small. The total and RF current of photodetector is then given as:

$$i_{PD} \approx R\left(\frac{P_{01}}{2} - KP_{01}Cos(\omega_m t) + P_2 + \sqrt{2P_{01}P_2}(1 - KCos(\omega_m t))Cos(\Delta\omega t + \Delta\phi)Cos(\phi_p)\right) \tag{4.13}$$

$$i_{PD.rf} \approx R\left\{-KP_{01}Cos(\omega_m t) + \sqrt{2P_{01}P_2}Cos(\phi_p)(Cos(\Delta\omega t + \Delta\phi) - KCos(\omega_m t)Cos(\Delta\omega t + \Delta\phi))\right\} \tag{4.14}$$

The Rf current includes four frequency components: ω_m, $\Delta\omega$, $\Delta\omega+\omega_m$, and $\Delta\omega-\omega_m$. As mentioned earlier, this method is used for frequencies exceeding the bandwidth of our photodetector. Therefore, the first three components are normally outside the photodetector bandwidth. The wavelength of the tunable laser can be adjusted so that the fourth component, $\Delta\omega-\omega_m$, can be detected by the photodetector. For example, for $\Delta\omega-\omega_m$ = 18.5 GHz and modulation frequency of 19 GHz, the beat frequency ($\Delta\omega$) is adjusted to 48.5 GHz. This corresponds to a wavelength difference of almost 0.388 nm. Figure 4.18 shows the results of a measurement. The modulating signal at 19.5 GHz looks like a sharp delta function while the converted signal is broadened due to limited linewidth and phase noise of laser sources.

The conventional method for spectrum measurement was used for frequencies up to 20 GHz while heterodyne technique was used for frequencies between 20 to 40 GHz. In this case the bandwidth measurement is limited by the bandwidth of cables, probes, and signal generators. The bandwidths of all these components were limited to 40 GHz.

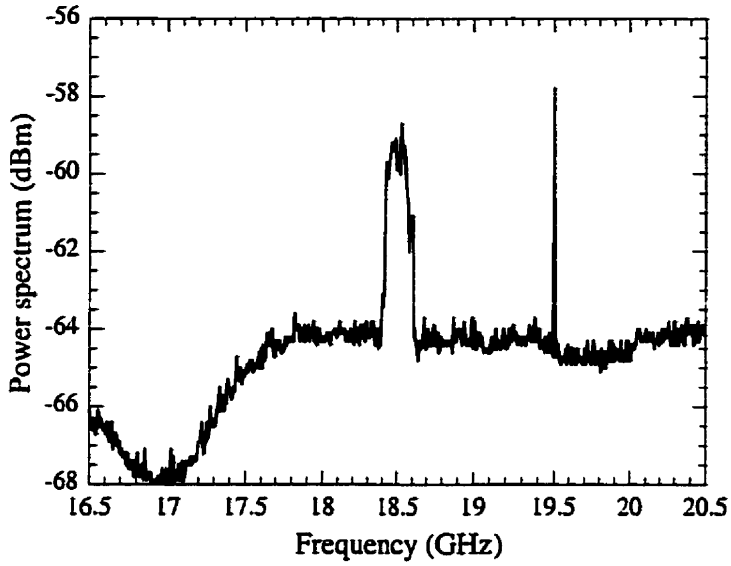

Figure 4.18 Measured frequency response of a modulated optical signal at 19.5 GHz using heterodyne technique.

4.4 Discussion

In this chapter, we described different techniques that were used to characterize semiconductor traveling electro-optic modulators. This includes photoluminescence and CV-measurement techniques to characterize the semiconductor materials. These enable the designer to verify the material composition, substrate uniformity, and the carrier concentration of the substrate. We also discussed the fabrication process including a self-align technique that enhances the performance of these modulators. Finally, measurement setups were presented that were used to characterize the optical waveguide properties, low frequency transfer function, and high frequency modulation.

The next chapter contains measurement results for different devices. First, the optical and microwave measurement results will be presented. The results of our investigation on microwave performance of electrodes as a function of substrate doping density are given next. The device performances, including modulation frequency, half-wave voltage, extinction ratio, are given for different modulators at the end.

CHAPTER 5

Measurement Results

This chapter describes the optical, electrical and electro-optical measurement results on different traveling wave electro-optic modulators. The measurements are performed on polarization sensitive and insensitive MZ modulators with slow wave CPW electrodes, polarization sensitive modulator with slow-wave interdigitated CPS electrodes, and slow wave CPS mode/polarization converters. We will also present the material characterization results on ion implanted and doped epitaxially grown materials.

5.1 Optical Properties

First we present the measurement results on wafer #3, #4 and #5. As described earlier, these optical structures were designed and fabricated to evaluate the effect of the insertion of the thin layers of AlAs or AlGaAs with high aluminum concentration or a combination of them. Three different wafers corresponding to the three layer structures were grown by conventional Organo-Metallic Vapor Phase Epitaxy (MOVPE). The epitaxial layers were unintentionally doped. Optical waveguides of 3, 4 and 5 μm ridge

Table 5.1 Measured optical loss for three optical structures wafer #3, #4, and #5, inserted with thin layers of AlAs. Losses are in dB/cm.

Ridge width (μm)	Wafer #3	Wafer #4	Wafer #5
3	1.3	1.5	1.6
4	1.3	1.4	1.4
5	1.3	1.4	1.4

width with about 1 μm etch depth were defined by standard optical lithography and Reactive Ion Etching (RIE) process. The waveguides were single mode in all cases. The waveguides were cleaved and single mode fibers were used to couple the light from a 1.55 μm wavelength tunable laser into and out of the samples to measure the propagation loss of the waveguides. In each case both the non-destructive Fabry-Perot waveguide resonant cavity method and cutback method is used. Both measurement techniques yielded consistent results, as given in Table 5.1. These optical waveguides did not demonstrate significant polarization dependent loss (PDL). These results indicates that, within the experimental error ±0.3 dB/cm, the two samples with thin $Al_xGa_{1-x}As$ inserts, wafer #4 and #5, do not show additional losses compared to the control sample, wafer #3. The deviation in loss of the fundamental mode between the control and the test samples in Table 5.1 is qualitatively consistent with the differences found in during modeling of the waveguides. Waveguide losses are mainly due to the ridge roughness caused by RIE etching, absorption introduced by residual carrier concentration, and material non-uniformity.

The loss measurement results carried out on the optical waveguides fabricated on wafer #1 and #2 are given in Table 5.2. The coupling loss was estimated from the actual input and output measured optical power, taking into account the optical loss of the waveguide. The waveguides on wafer #2 demonstrated large PDL. Measured PDL was ranging between 7 dB/cm to 10 dB/cm. High propagation loss for TM polarization severely degrades the performance of polarization converters and polarization insensitive modulators. As mentioned in chapter 2, these devices are operation based on coupling between the two polarization states. In this specific case, the power in the TM polarization is strongly attenuated so that there is no coupling from TM to TE mode. In

Table 5.2 Typical propagation and coupling loss values for the optical structures wafer #1, and #2, used in the fabrication of traveling wave modulators.

Wafer No.	Propagation loss (dB/cm)		Coupling loss (dB)
	TE	TM	
1	1.2	1.7	3-3.5
2	1.5	8.5	6-6.5

other words, there is a distributed analyzer built into the waveguide. The device under this condition is not properly functioning. A discussion on the transfer function of mode converters will also come to the same conclusion.

One source of PDL could be scattering loss due to the roughness on the walls and surface of ridge waveguide. An infrared camera was mounted on top of the sample to capture the scattered lights from these waveguides. The scattered light for both polarization states and the difference between the two cases were negligible. To examine the mode profiles, infrared camera was placed in front of the waveguide to collect the light through an objective. Mode profiles for TE and TM states of polarization in on waveguide on wafer #2 are given in Figure 5.1(a) and 5.1(b). Although numerical results suggest that TM mode is more confined than TE mode, Figure 5.1 shows that TM mode profile is weaker, less confined and there is some slab guiding. The slab guiding is not seen in TE mode. Numerical simulation was performed with the actual physical dimension of the waveguide and no slab guiding was observed for either polarization state. To compare, the mode profiles for the two polarization states in a waveguide fabricated on wafer #1 are given in Figure 5.1(c) and 5.1(d). The two modes are similar and there is no slab guiding in either case. This type of propagation pattern (mode profile) causes the high propagation loss for TM mode. It is believed that this is mainly due to impurities in the dielectric layer (2000 Å of SiO_2) deposited after RIE. Some evidence of this impurity will be presented in the future.

The relatively high coupling loss compared to the devices fabricated on $LiNbO_3$ is due to the small optical mode size. A small optical waveguide is required to enable the designer to simultaneously reduce the interelectrode gap for high electric field and to increase the overlap factor between the optical and electrical field. The coupling loss has

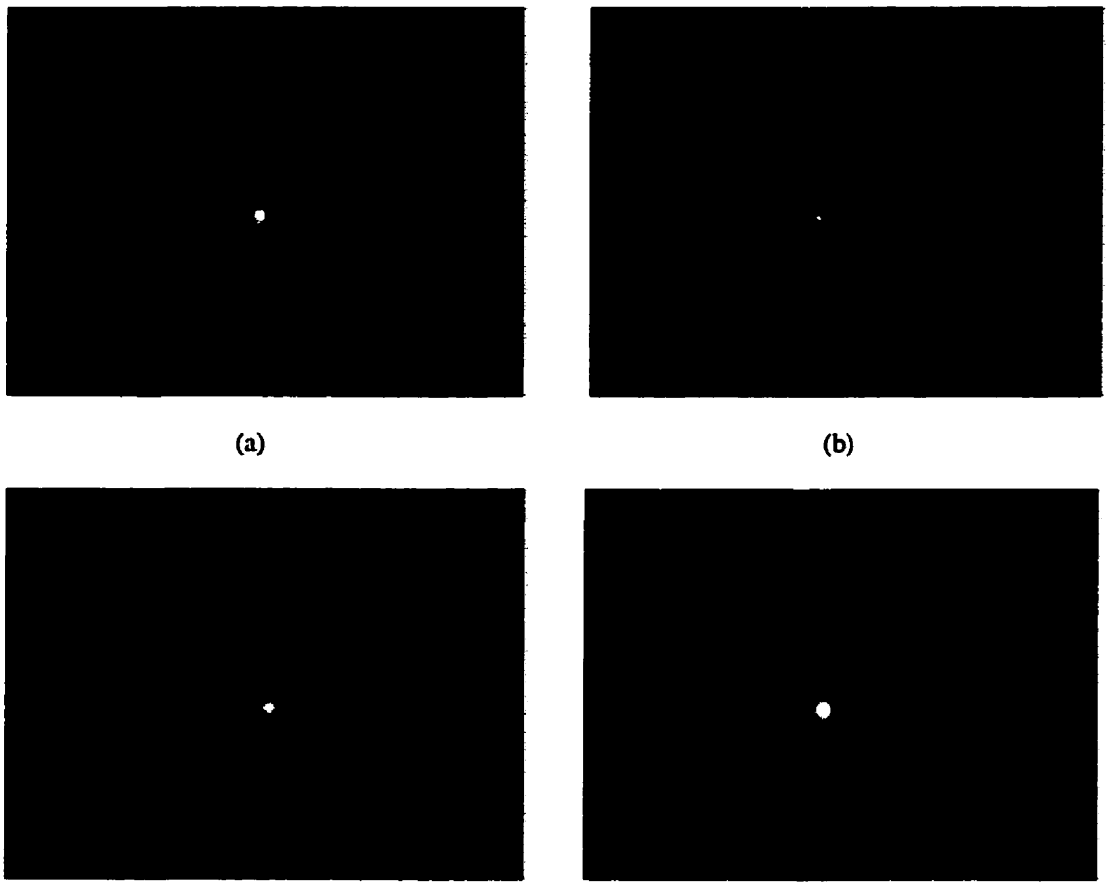

Figure 5.1 Mode profiles taken by an infrared camera at the output of a 2.5 μm wide waveguide on wafer #2 for a) TE polarization, b) TM polarization, and at the output of a 3 μm wide waveguide on wafer #1 for c) TE polarization, d) TM polarization.

to be lowered by different techniques such as spot size transformation if this device is to be used as a discrete element in an optical communication system.

5.2 Electrical properties

The s-parameters of the electrodes were measured from 45 MHz to 40 GHz using a Cascade Probe Station and a HP8510 network analyzer. The measured s-parameters were then used to obtain the ABCD matrix of the coplanar slow wave structures. The line

parameters such as phase velocity, characteristic impedance, and microwave loss can then be calculated from this matrix.

5.2.1 Slow Wave Structures on SI-GaAs Substrate

In this section, we will present a comparative study on the microwave performance of different planar electrodes on LIT-1, LIT-2 and LIT-3 mask sets. LIT-1 consists of 30 different slow wave CPW electrodes. Different slow wave structures such as CPW, CPWA, CPWB, CPWC, CPWD were included on this set of masks to establish design rules and to evaluate the performance of different structures (see Appendix I). The design goals for all the structures are to achieve characteristic impedance of 50 Ω, phase velocity equal to that of optical waveguide, and low microwave insertion loss. The slow wave structures designed on LIT-1 have the interelectrode gap, S, of 5-10 μm and longitudinal overlap factor, Γ_l, of 0.25-0.75. An efficient electro-optic modulator will employ an electrode with a small S and large Γ_l. In fact, $(\Gamma_s.\Gamma_l)/S$ has to be maximized in all electro-optic modulators. The other important parameter in this comparative study is the microwave insertion loss. All the structures designed on LIT-1 have achieved the required slowing of the microwave signal. Appendix IV contains the measured data for slow wave electrodes on LIT-1 mask set as well as on LIT-2 and LIT-3 mask sets. The characteristic impedance and phase velocity are almost flat over the entire frequency range and therefore the average value is given for each structure. The microwave loss is given at the maximum value over the frequency range. Some physical dimensions of the electrodes are also given that are believed to affect the microwave loss and modulator performance.

Slow wave electrodes on LIT-1 mask demonstrate an average phase velocity, V_{phavg}, of 8 to 9 cm/nsec, average characteristic impedance, Z_{0avg}, of 40 to 50 Ω, and microwave insertion loss, α_m, of 4 to 6.5 dB/cm measured at 35 GHz. Here, we present the measured results for CPWB13 and CPWD18 slow wave structures on LIT-1 mask. The other structures on this mask are slowly different from these two. The major

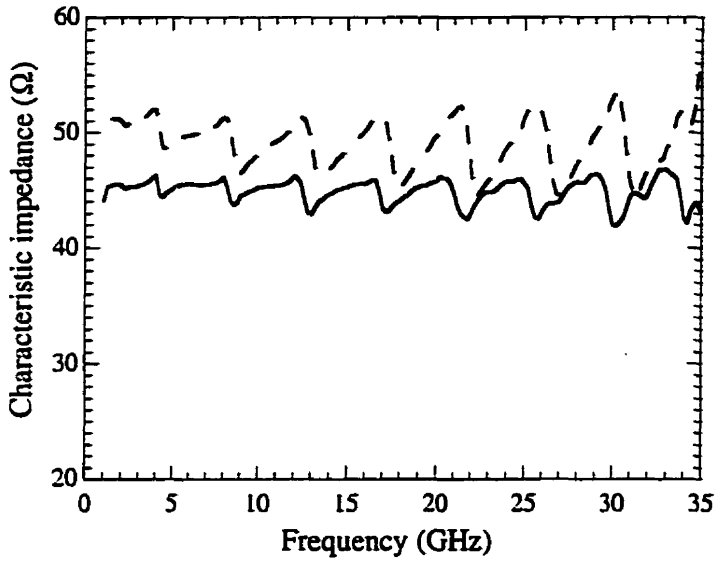

Figure 5.2 Characteristic impedance of CPWB13 (dashed) and CPWD18 (solid) electrodes on LIT-1 mask set fabricated on SI-GaAs substrate.

difference between CPWB13 and CPWD18 structures is that the capacitive elements in the former are fins extending from signal and ground electrodes to the interelectrode region while the latter employs T-railed capacitive elements. The characteristic impedances of the electrodes are given in Figure 5.2. The average Z_0 is 45 Ω and 49 Ω for CPWD18 and CPWB13, respectively. This Figure also illustrates a periodic ripple in the characteristic impedance of the electrodes. The periodicity is related to the electrode length. This phenomenon was observed in the measured data for all electrodes. The large ripple in characteristic impedance is at frequencies where the s_{11} and s_{22} are very small. In such a case, the accurate measurement of these parameters is not possible. If the device under study is considered as a symmetric and reciprocal system, Equation 3.10 is simplified to $Z_0 = \sqrt{B/C}$. From Equation 3.9, it is seen that in a low loss transmission line, the numerators of both parameters, B and C, consist of a subtraction of two very close values. So, any small inaccuracy in s_{11} and s_{22} measurement will result in a relatively large error in the calculation of Z_0. The errors in s_{11} and s_{22} can be caused by any small impedance mismatch limited by the measurement accuracy. Since only A and D parameters are used in the calculation of microwave loss, α_m, and phase velocity, V_{ph},

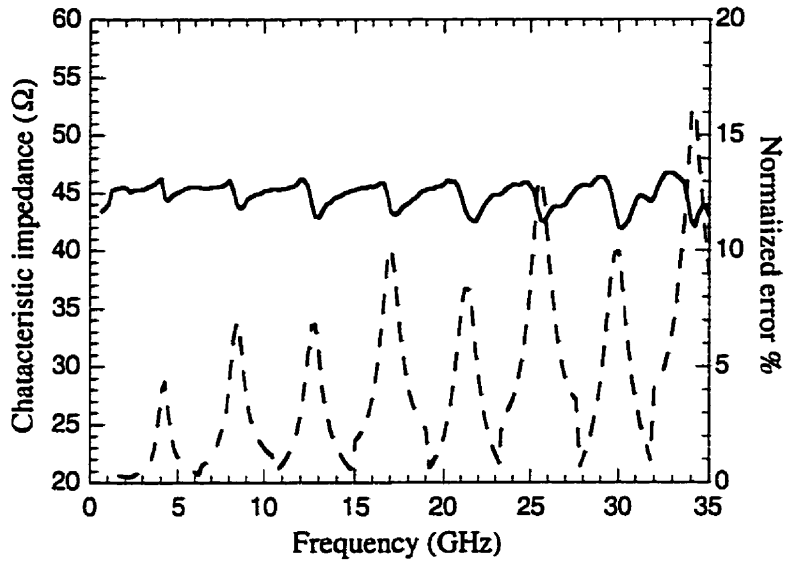

Figure 5.3 Characteristic impedance of CPWD18 (solid) and normalized impedance error (dashed). An error of 0.1% was considered in the measurement of s-parameter phase and magnitude.

the above discussion shows clearly the reason these ripples are observed only in Z_0. The sensitivity of characteristic impedance, ΔZ_0, as function of error in the s-parameters are analyzed. The results are given in Appendix V. Figure 5.3 gives the characteristic impedance for CPWB13 as well as its calculated normalized error where a 0.1% error was assumed in the measurement of both magnitude and phase of the s-parameters. A small measurement error in the magnitude and phase of the s-parameters, 0.1%, translate to a much larger error, as high as 16% at 35 GHz in the calculation of characteristic impedance. The error curve also shows a periodic ripple whose magnitude increases with frequency. The error ripples, impedance ripples, and the s_{11} and s_{22} minimums are all occurring at the same frequencies. This is in good agreement with the ripples observed on the characteristic impedance. Therefore, one can discard the data where the s_{11} and s_{22} are very small and their accurate measurement is difficult and use some polynomial curve fitting or data averaging to get the actual characteristic impedance of the slow wave structure.

The microwave phase velocities and insertion losses of these two electrodes are also given in Figure 5.4. The phase velocity of the microwave signal on both electrodes

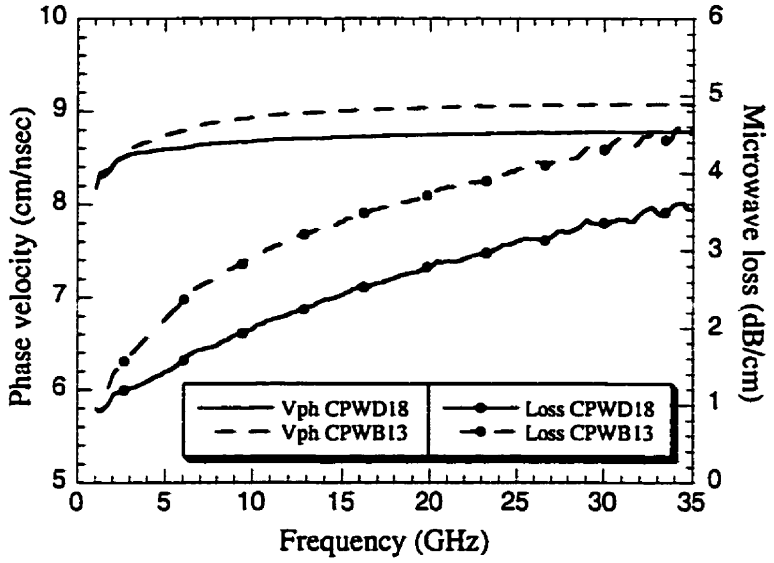

Figure 5.4 Measured phase velocity and microwave loss for CPWD18 and CPWB13.

looks almost flat over the entire frequency range. This means that there is practically no microwave dispersion on these lines. Therefore, the phase and group velocities of microwave signal are the same. This velocity has to be matched to the group velocity of optical signal propagating along the optical waveguide. A more careful observation reveals that CPWD18 reaches its saturation speed at almost 3 GHz while CPWB13 does that at about 7 GHz. Microwave losses of 3.5 dB/cm and 4.5 dB/cm are measured for CPWD18 and CPWD13, respectively. Microwave losses are proportional to $\sqrt{GHz}$ for all electrodes. Although both electrodes can achieve velocity match to the optical signal, CPWD18 electrode in particular, and all CPWD in general, demonstrate lower microwave loss, smaller interelectrode gap, S, and higher longitudinal overlap factor, Γ_l. For example, Γ_l is equal to 0.5 and 0.75 for CPWB13 and CPWD18, respectively. In conclusion, CPWD electrode structure outperforms other planar structures designed on LIT-1 mask set for traveling wave electro-optic modulation applications.

In the following, the electrode structures on LIT-2 mask set are analyzed. CPWD electrode structure was chosen as the base electrode and some modified versions were added. This includes T-railed coplanar strip (CPSD), interdigitated T-railed coplanar strip (CPSD-id), and asymmetric T-railed coplanar waveguide (CPWD-as), see Appendix I.

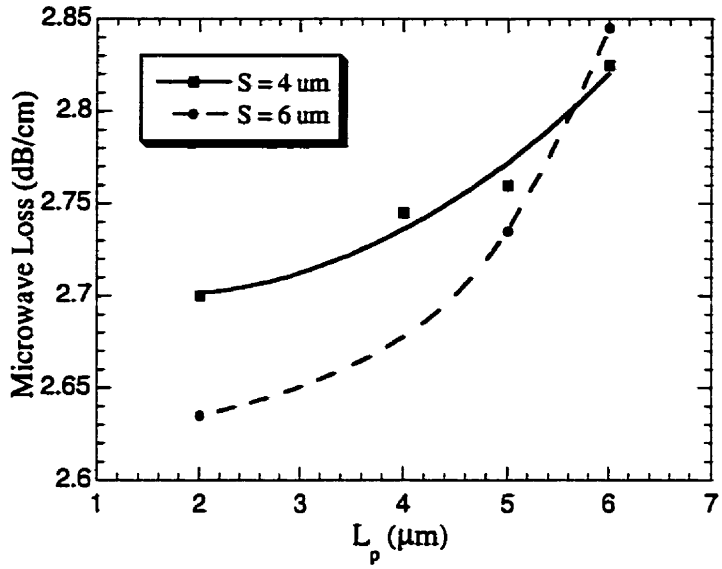

Figure 5.5 Microwave insertion loss as a function of L_p with S as parameter for CPWD electrodes (see Appendix I).

Figure 5.5 illustrates the results for CPWD insertion loss as a function of L_p with S as parameter. As L_p increases from 2 to 6 μm with $S = 4$ μm, the microwave loss increases by only 0.21 dB/cm. T_s was also changed from 44 to 55 μm to meet the design phase velocity and characteristic impedance. These results show that changes in the L_p and S parameters in the above mentioned range do not significantly affect the microwave loss of the slow wave structures. It is worth mentioning that for all the structured analyzed in Figure 5.5 the distance between centre electrode and ground electrode of the unloaded transmission line, G, is kept constant at 34 μm. If G increases, W has to increase to meet the design phase velocity and characteristic impedance. We have increased G from 34 μm to 48 μm, and therefore W has increased from 20 μm to 30 μm. The microwave loss variations as a function of G are shown in Figure 5.6. The microwave loss for a uniform coplanar waveguide with the 10 μm centre electrode width and 6 μm gap is also included in this figure. As the gap between the centre electrode and ground electrode, G, increases the microwave loss decreases significantly. The width of fins and pads, are small enough to to prevent the current from flowing into these capacitive elements and therefore keep most of the current flowing along the edges of the main ground and signal electrodes. The

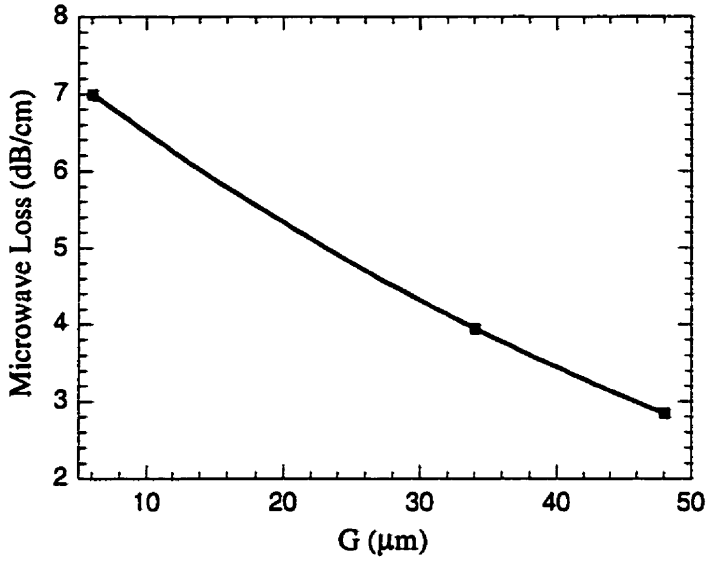

Figure 5.6 Microwave insertion loss as a function of distance between the main signal and ground electrodes, *G*, (see Appendix I).

microwave insertion loss is strongly dependent upon the separation between these currents and therefore the gap between the centre electrode and ground electrode of the unloaded transmission line, *G*. The microwave loss is reduced for almost 1.1 dB/cm when *G* is increased from 34 μm to 48 μm. Allowing the current to flow into fins and pads will increase the effective length of the device and therefore increase the electrode resistance. It also reduces the effective gap between the currents flowing along the signal and ground electrodes, G_{eff}, which will increase the insertion loss. Finally, currents flowing along fins and pads will encounter higher resistance due to smaller width compare to the width of main signal and ground electrodes. These facts become more clear by examining the measured results on LIT-1 given in Appendix IV. For example, CPWA6 and CPWA14 both have $W = 50$ μm and $G = 65$ μm, but the fin width of the former is half of that of the latter. The microwave insertion losses for CPWA6 and CPWA14 are 3.8 dB/cm and 4.7 dB/cm, respectively. Needless to say that the other main parameter that affects the insertion loss is the width of the main signal electrode, *W*. Since this electrode carries the highest current density, an increase in W will reduce the insertion loss as seen by CPWD18 and CPWD30 on LIT-1 mask set.

The effect of W_s variations was also studied. W_s was changed from 2 μm to 4 μm and the microwave loss was reduced by less than 0.1 dB/cm. This again suggests the importance of G parameter in the design of low loss planar slow wave structures.

The asymmetric CPWD slow structures were also experimentally investigated. In these structures the length of the fins extending from the centre electrode, L_{ss}, is smaller than the length of the fins extending from the ground electrodes, L_{sg}. The asymmetric structure has some advantages over the symmetric structure. These include: 1) a smaller arm separation of the optical MZ interferometer and therefore an overall shorter device; 2) a higher longitudinal overlap factor and therefor longer effective interaction length. The physical dimensions of one of the symmetric device, CPWD12, under study are: W_s = 4, $L_{ss} = L_{sg}$ = 14, W_p = 30, L_p = 2, W = 20, S = 6, L = 300, G = 34, and T_s = 39, all dimensions in μm. The corresponding asymmetric device, CPWD-as22, has the following dimensions different from the above: L_{ss} = 7, L_{sg} = 21, and T_s = 32, all dimensions in μm. The arm separation of the MZ optical interferometer for the asymmetric structure can be as low as 40 μm while this value for the symmetric structure is 54 μm. The longitudinal overlap factor is 0.94 and 0.77 for the asymmetric and symmetric structure, respectively. This comparison shows that the asymmetric structure outperforms the symmetric structure, but the microwave loss has increased by about 0.25 dB/cm. The characteristic impedance, phase velocity, and microwave loss for these two structures are shown in Figures 5.7 and 5.8.

Slow wave electrodes on LIT-3 mask are slight modification of electrodes on the previous mask. The length of electrodes vary from 2 cm to 2.3 cm. Longitudinal overlap factor, Γ_l, ranges from 0.75 to 0.95. Interelectrode gap, S, has been reduced to as small as 2 μm. The width of the main section of CPSD-id electrodes have been increased to reduce the microwave insertion loss. It is noteworthy to mention that the metallization thickness on LIT-3 electrodes has been 0.85 μm compare to 1.5 μm metallization thickness on LIT-1 and LIT-2 masks. Physical electrode dimensions such as W_s, L_p, and S are as small 2 μm. To maintain the lithography resolution to such small values, the thickness of photoresist had to be reduced. The reduction in photoresist thickness resulted

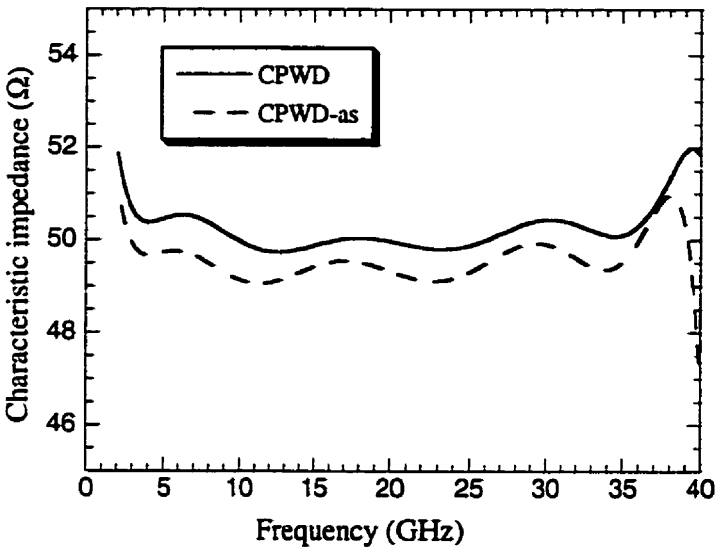

Figure 5.7 Characteristic impedance of symmetric (CPWD) and asymmetric (CPWD-as) coplanar waveguide on SI-GaAs substrate.

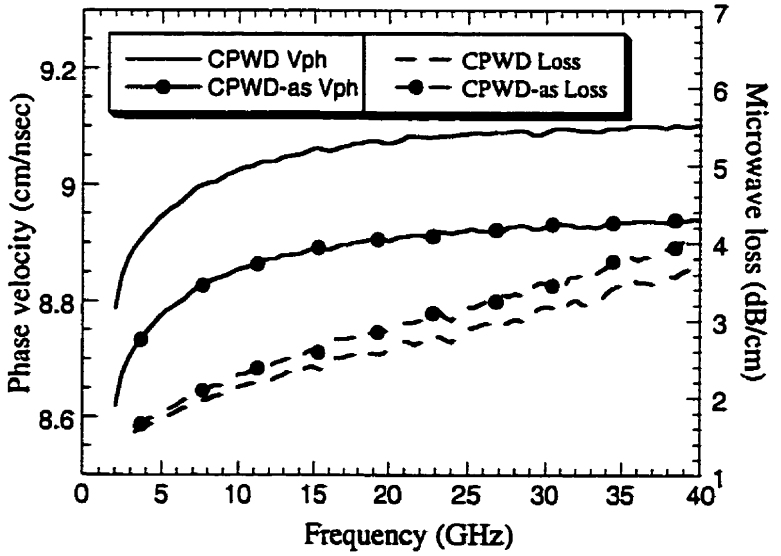

Figure 5.8 Phase velocity and microwave insertion loss of symmetric (CPWD) and asymmetric (CPWD-as) coplanar waveguide on SI-GaAs substrate.

in reduction in metallization thickness. This certainly caused an increase in microwave insertion loss. This fact can be seen by comparing the insertion loss of CPWD and electrodes on LIT-3 and LIT-2 mask sets. CPWD electrodes on these two masks have

similar *W* and *G* and all have very narrow fins and pads. CPSD electrodes demonstrated similar microwave insertion loss as CPSD electrodes on LIT-2 mask and achieved velocity and impedance match condition. The width of the main signal and ground electrodes on CPSD-id structures compare to those on LIT-2 have been increased to reduce the microwave insertion loss. The insertion loss on this type of electrode has been reduced from 7.5 dB/cm to 5.5 dB/cm.

The effects of the optical ridge waveguide and dielectric layer between the metal electrode and substrate are experimentally investigated. To simulate the optical ridge waveguide on GaAs/AlGaAs heterostructure optical layers, see Figure 3.1(a), LIT-2 mask set was used to develop ridge waveguide of 0.9 deep on SI-GaAs wafers. Although the devices are fabricated on SI-GaAs, we also study the effect of a thin layer of SiO_2 (0.2 μm) between the metal electrodes and substrate on the slow wave electrode performance. These structures will eventually be integrated with the optical ridge waveguides in a heterostructure GaAs/AlGaAs substrate.

The slow wave structures have been modeled and designed using a multilayered EM simulator for planar circuits. This simulator does not allow the effects of optical ridge waveguides to be taken into account in the design model. In the model, we have considered a 0.2 μm SiO_2 layer between the electrodes and GaAs substrate. The design goal was to realize a planar structure on GaAs with characteristic impedance of 50 Ω and phase velocity of 8.5 cm/nsec that is about the group velocity of optical signal in GaAs/AlGaAs optical structure wafer #2 with a free space wavelength of 1.55 μm. The following are the different conditions under analysis: slow wave structures on SI-GaAs a) without ridge and without SiO2 layer; b) without ridge and with SiO2 layer; c) with ridge and without SiO2 layer; and d) with ridge and with SiO2 layer. For the cases where ridges are in between the electrode pads, the ridge is filling the whole gap leaving no air space. The physical dimensions of the slow wave structures on LIT-2 mask set are given in Appendix II.

5.2.1.1 Ridge under the pads of slow wave structures

This situation is employed where the normal component of the electric field is to be exploited for phase modulation. The ridge optical waveguides are placed under the pads of the capacitive elements. The presence of the SiO_2 layer reduces the effective dielectric constant of the substrate and therefore reduces the capacitance per unit length of the line. Since both phase velocity and characteristic impedance are function of $1/\sqrt{C}$, C is the capacitance per unit length of the line, it is expected that phase velocity and characteristic impedance of the line increase. The presence of 0.2 μm SiO2 layer, cases (b) and (d), has increased the phase velocity and characteristic impedance of the line by 0.35–0.5 cm/nsec and 2–3 Ω, respectively. The addition of the ridges under the pads of the slow wave structures for case (d) causes an increase in the phase velocity by less than 0.1 dB/cm and the increase in characteristic impedance is negligible. For case (c), the presence of the ridges under the pads decreases the phase velocity by less than 0.1 cm/nsec and reduces the characteristic impedance by less than 1 Ω. Therefore, the effect of the presence of ridges under the pads is negligible and below the precision accounted for during design modeling and fabrication. The presence of the dielectric layer and ridge optical waveguide did not contribute to a significant change in the microwave loss.

5.2.1.2 Ridge between the pads of slow wave structures

Figure 3.6 depicts the relative magnitude of the electric field components parallel to the surface of the substrate at 0.5 μm beneath the substrate interface. The electric field in the area between the pads of the slow wave structure reaches its maximum magnitude. The insertion of a ridge between the pads of the slow wave structure will result in confining more electric field lines through a medium with higher dielectric constant, substrate dielectric constant, rather than air. This increases the line capacitance and therefore will reduce the phase velocity and characteristic impedance of the line.

It is expected that the presence of the ridge between the pads have significant effect on line parameters. The results show that for cases (c) and (d), the insertion of ridges between the pads reduces the phase velocity and the characteristic impedance by 0.4~0.5 cm/nsec and 2~3.5 Ω, respectively. The reduction in characteristic impedance for case (d) is less than case (c). The microwave losses can be estimated as [81]:

$$\alpha_m \propto \frac{R}{Z_0} \tag{5.1}$$

where R is the total resistance and Z_0 is the characteristic impedance of the transmission line. So, when the presence of the SiO_2 layer increases the characteristic impedance of the line, the microwave insertion loss reduces and where the insertion of optical ridges reduces the characteristic impedance, the insertion loss increases. The microwave losses increased by 0.3~0.4 dB/cm when the ridges are inserted between the pads. As these results show the effects of ridges between the pads are more significant than the ridges under the pads.

5.2.2 Slow wave structure on SI-InP substrate

Although significant research has already been carried out for the characterization of slow wave structures on GaAs substrates, the performance of slow wave structures on InP is also of great interest because of the advantages offered by integrating external modulators with InP/InGaAsP lasers operating at 1.55 μm. Here, the performance of coplanar slow wave structures fabricated on semi-insulating InP is presented. These structures are the slow wave electrodes on LIT-1 mask set which were initially designed for operation on SI-GaAs substrates. Since the dielectric constant of SI-GaAs and SI-InP are approximately the same, these structures were then fabricated on both SI-GaAs and SI-InP. The design parameters used for the slow wave electrodes were characteristic impedance, Z_0, of 50 Ω and velocity match of the optical signal.

S-parameter measurements were performed on all slow wave structures. Although all the slow wave structures demonstrated the slowing of the microwave signal and

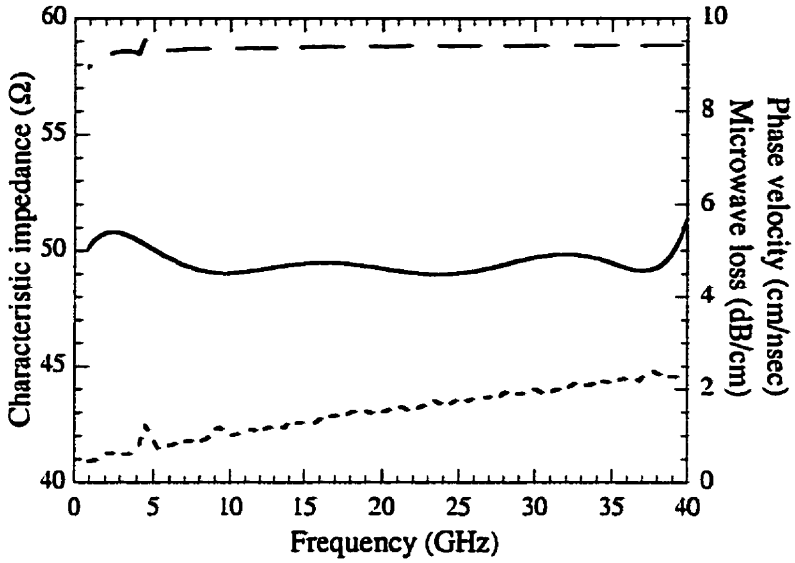

Figure 5.9 Measured characteristic impedance (solid), phase velocity (dashed), and Microwave loss (dotted) as a function of frequency for CPWD18 on SI-InP.

matching to 50 Ω characteristic impedance, the CPWD structures showed the lowest loss measured for all the structures fabricated on both GaAs and InP. The calculated characteristic impedance, phase velocity and microwave loss for the CPWD18 (one of CPWD structures) slow wave structure fabricated on SI-InP are shown in Figures 5.9. These parameters for CPWD18 structure on SI-GaAs are depicted in Figures 5.2 and 5.4. The insertion losses measured on the InP substrate are 1 to 1.5 dB lower than on the GaAs substrate at the high frequency end. This difference is also observed for the other structures, although they do not exhibit the lowest overall insertion loss. The measured phase velocity and characteristic impedance on InP are also in close agreement with the original design parameters for GaAs. This is due to the small difference between the InP and GaAs dielectric constants.

These results indicate that InP is a good candidate for electro-optic modulation application at 1.55 μm.

5.3 Material characterization

The bulk of the research investigating the design and the performance of traveling wave electro-optic modulators is carried out on semiconductor material such as GaAs and InP. The bandwidths of these modulators are strongly dependent upon the microwave loss of the electrodes in a velocity match condition. The integration of these designs with ridge optical waveguide heterostructures was successfully carried out on so called unintentionally doped substrates and small-signal modulation demonstrated by a small number of researchers [82]-[84]. As mentioned earlier, unintentional doping can mean a residual carrier concentration, n, between 1×10^{14} cm^{-3} and 5×10^{16} cm^{-3}, depending on the epitaxial material and growth technique used. The main purpose of this section is to examine the behaviour of slow wave electrodes fabricated on doped substrates to determine an upper limit to the substrate carrier density suitable for traveling wave electro-optic modulation applications.

We present the microwave loss measurements of a variety of planar electrodes, i.e. CPWs and CPSs, defined on epitaxial and ion implanted GaAs as a function of substrate carrier density. The doping range under study is between 1×10^{8} cm^{-3} (suggested by the manufacturer) and 2×10^{18} cm^{-3}. The loss measurements can be modeled using the effect of the free carrier interaction with the RF electric field present in the semiconductor material at the interelectrode gap. The measurements were carried out as a function of frequency from 45 MHz to 40 GHz. This dependence of the RF loss on the carriers is also a function of frequency. The results are consistent with the model. In addition, the loss measurements obtained are independent of the nature of the substrate material, whether epitaxial or ion implanted SI-GaAs and the electrode geometry used.

A number of coplanar waveguides designed on LIT-1 mask set were used to investigate the performance of traveling wave structures on a number of epitaxial substrates (see Table 5.3). The material used was either grown by liquid phase epitaxy (LPE) or by metal-organic chemical vapor deposition (MOCVD). One substrate consisted of a (Ga,Al)As based, unintentionally doped, optical waveguide heterostructure grown by

Table 5.3 Doped layer specifications for samples used for the RF loss measurements on epitaxial and single crystal substrates.

Material	Growth	Type	Dopant	n (cm^{-3})	Doped layer thickness(μm)
GaAs	LEC	SI	Si	1×10^{8}	350
GaAs	MOCVD	p	Si	5×10^{14}	
GaAs	MOCVD	n	Si	1×10^{16}	0.914
GaAs	LPE	n	Si	6.5×10^{16}	0.988
GaAs	MOCVD	n	Si	2×10^{17}	
InP	LEC	p	Cd	2×10^{18}	400

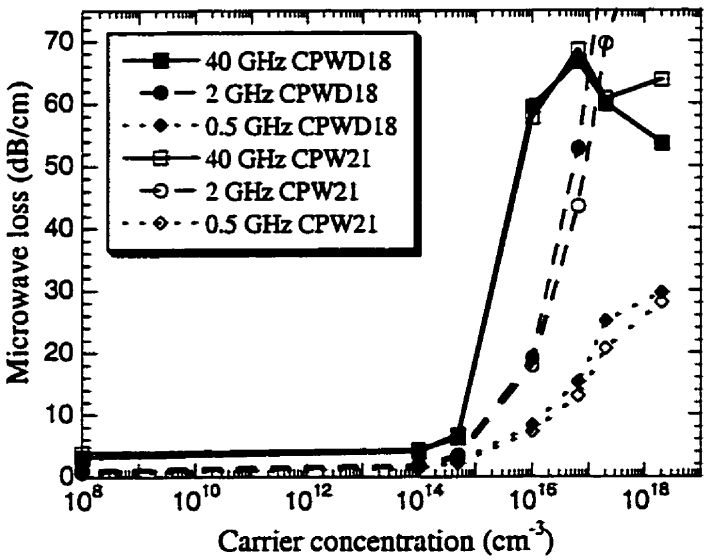

Figure 5.10 Measured microwave loss for two coplanar waveguides (a uniform and a loaded CPW) on epitaxially grown structures as a function of active layer doping at different frequencies.

MOCVD at the Communications Research Center (CRC). The epitaxial layer thickness varied from sample to sample. As a first approximation, it was assumed that the microwave loss would be a weak function of the active layer thickness. The loss was obtained from s-parameter data as a function of frequency up to 40 GHz. Figure 5.10 shows the microwave losses obtained for these samples at 0.5, 2, and 40 GHz as a

function of active layer carrier density. The results shown are for two different structures, CPWD and CPW. CPWD consists of a periodically loaded traveling wave structure that was designed to minimize RF losses due to sheet resistance of the electrode metallization (see Appendix I). CPW is a plain coplanar waveguide without fins or pads. The 60-70 dB/cm microwave loss saturation is the limitation imposed by the measurement system. For substrates with carrier density below 5×10^{14} cm^{-3}, the low microwave loss is mainly due to electrode metallization. Substrate free carrier absorption is believed to be the major contributor to microwave loss for substrate carrier density above 5×10^{14} cm^{-3}. The measured losses for the samples with n higher than 1×10^{16} cm^{-3} are all around 60 dB/cm. Substrates with doping density between 5×10^{14} cm^{-3} and 1×10^{16} cm^{-3} were not available. Therefore the straight line in that region of Figure 5.10 is a linear interpolation. The microwave loss for the two different structures, CPW and CPWD, at different frequencies are also very similar, which indicates that the microwave losses due to excess carriers are independent of the electrode geometry. This Figure also shows that the RF loss at high frequency increases rapidly for carrier density in excess of 5×10^{14} cm^{-3}. This result suggests that semiconducting material used for the fabrication of traveling wave electro-optic modulators must not exceed carrier density levels of approximately 5×10^{14} cm^{-3}. From loss measurements at different frequencies, it is observed that the rate of increase in microwave loss is frequency dependent. The onset of RF loss is found to be independent of frequency.

This relationship was verified more systematically by fabricating the CPWs on [100] flat ion-implanted SI-GaAs substrates. The wafers were implanted with Si_{29} using a GA-3204 Ion Implanter, at 90 KeV at a 10° tilt to minimize channeling effects. The substrates were coated with 300 Å of Si_3N_4 prior to implantation. Approximately 87% activation was achieved with an anneal at 960 °C for 6 seconds resulting in an active layer thickness of about 0.2 μm. The implant doses were chosen by using the software PROFILE which models the carrier density as a function of depth. Figure 5.11 compares the carrier density profile as a function of depth as determined by CV-technique and as modeled using PROFILE at a dose of 2.33×10^{12} cm^{-2}. At dosages below 1.4×10^{12} $/cm^2$,

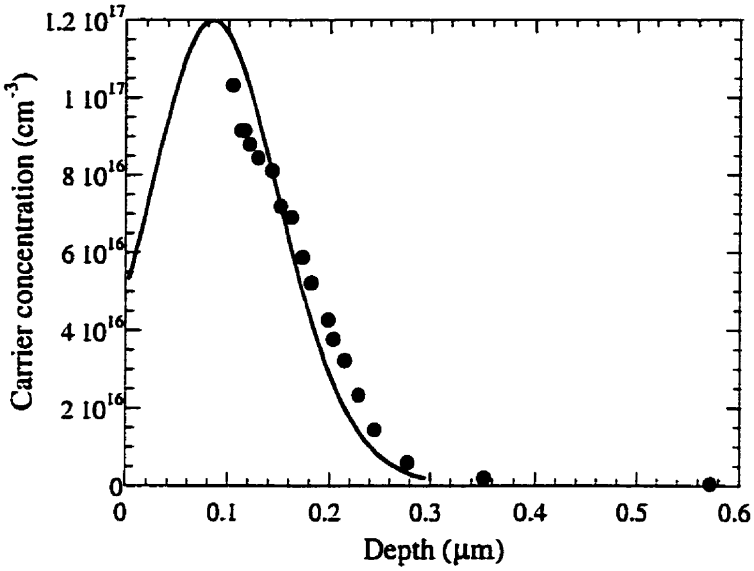

Figure 5.11 Measured (circles) and simulated 87% activated (solid) carrier density profiles, as a function of depth of an implanted sample with SiO_{29} at a dosage of 2.33×10^{12} cm^{-2} as obtained from C-V measurements.

which corresponds to $n \sim 7.21\times10^{16}/cm^3$, the C-V technique fails to accurately determine the carrier density. n in ion implanted substrates corresponds to the peak of the carrier density profile.

Having determined the precision of the implant model from Figure 5.11, PROFILE was used to predict the values of n at lower implant doses. As it will be seen below, the theoretical model requires n as an explicit input parameter. For this reason it is important to relate the values of the ion implant dose, D_{ii}, to n. In this work, it had to be assumed that the activation is independent of dose. Although this is only an assumption, no previous reference was found in the open literature invalidating this approximation at these low doping levels. The doping of the samples with D_{ii} over 1.8×10^{12} cm^{-2} were accurately measured and were used to extrapolate the doping of the substrates with lower level of dosage. The relationship between the implant dose D_{ii} and the values of n as obtained from C-V measurements (full circles), and those extrapolated from implant dose values assuming an activation independent of dose (open circles) is illustrated in Figure 5.12. The equation fitted to the data in the Figure 5.12 is used to obtain the thickness of a uniform active layer with doping density equal to the peak of the corresponding profile.

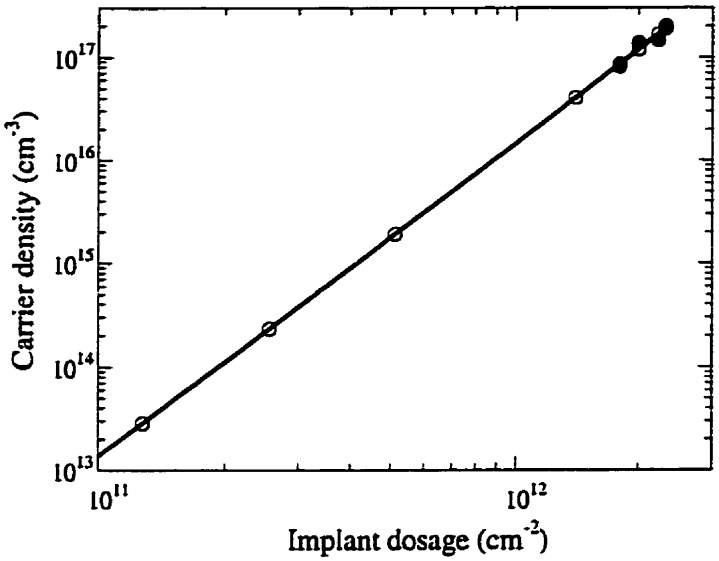

Figure 5.12 Relationship between substrate carrier density, n, and implant dosage, D_{ii}. Closed circle data are obtained from C-V measurements; open circles are extrapolated assuming a linear relationship between the log of dosage and the log of carrier density.

This method results in 0.17 μm thick uniform doped layer that is in good agreement with the data in Figure 5.11.

Figure 5.13 depicts the measured microwave loss variation with substrate doping as a function of frequency for the CPWD18 slow wave electrode fabricated on ion implanted substrates. The onset density for this graph is 7×10^{16} cm^{-3}. This loss dependence on doping is observed for all the other slow wave structures studied. The results in Figure 5.13 confirm the general findings obtained in Figure 5.10. Figure 5.10 and 5.13 clearly show that the loss rate as a function of doping varies with frequency. The slope of this loss rate is dependent upon the frequency of operation. As Figure 5.13 shows, the onset density of the loss curve is independent of frequency, as it was the case for epitaxial materials.

Figure 5.14 shows the evolution of the microwave loss as a function of frequency at a fixed doping level for the CPWD18 structure fabricated on ion implanted substrates. The loss in dB/cm is a linear function of the square root of the frequency [85], where the slope depends upon the electrode and substrate conductivity and electrode geometry.

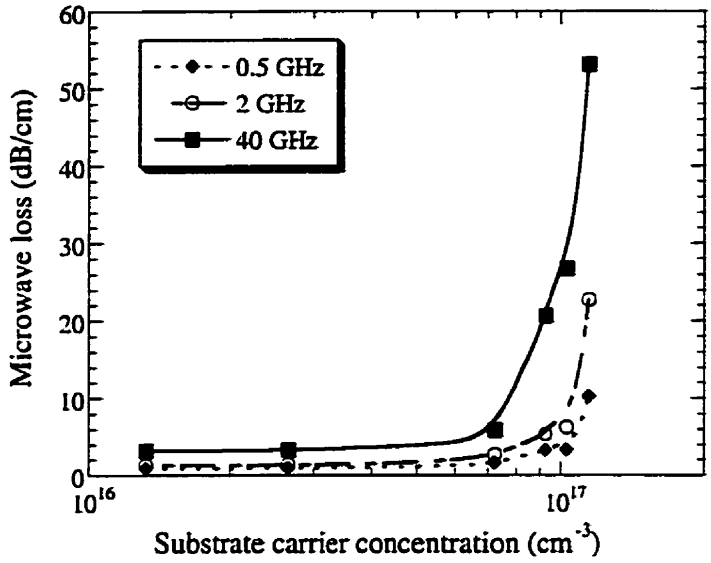

Figure 5.13 Measured microwave insertion loss for CPWD18 electrode as a function of substrate carrier concentration of ion-implanted wafers with Si_{29} at different frequencies.

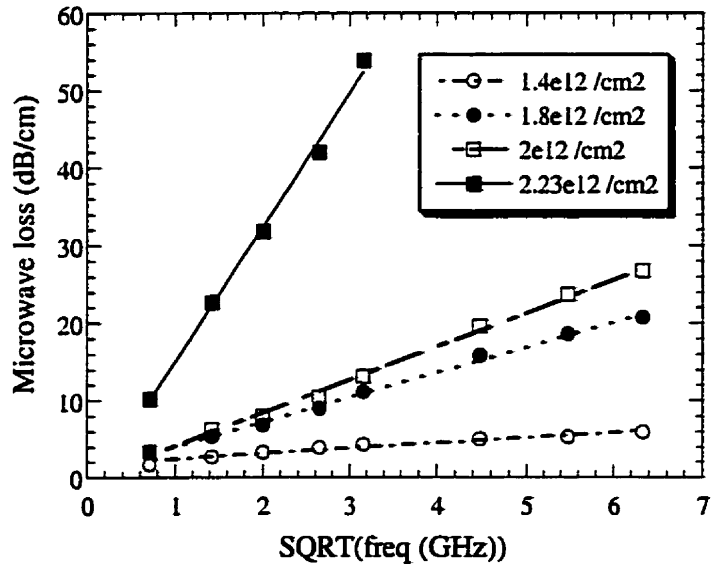

Figure 5.14 Measured microwave insertion loss for CPWD18 electrode as a function of square root of frequency for ion-implanted substrates at different dosage.

The behavior of free charge carriers under the influence of a periodic RF field can be described in terms of the complex conductivity:

$$\sigma = \sigma_0 \omega_0 \frac{\omega_0 - j\omega}{\omega_0^2 + \omega^2} \tag{5.1}$$

where $\sigma_0 = nq\mu_e$ and $\omega_0 = 1/\tau$, where τ is the average time between electron-phonon collisions and ω is the RF frequency. Here, the mobility μ_e is a function of the carrier concentration n. q is the electronic charge. From Equation 5.1, the real and the imaginary parts of the conductivity are expressed as:

$$\sigma_i = \frac{\sigma_0 \omega}{\omega_0} \tag{5.2}$$

$$\sigma_r = \sigma_0 \tag{5.3}$$

when $\omega << \omega_0$. Since $\sigma_i << \sigma_r$, the loss tangent of the substrate can be expressed approximately as:

$$\tan\delta = \frac{\sigma_r}{\varepsilon_0 \varepsilon_r \omega} \tag{5.4}$$

The loss tangent in Equation 5.4 was calculated as a function of n and frequency ω. S-parameters for the CPW structures under study were calculated for each loss tangent using the *Sonnet*™ EM simulation software. In the model, a thermal equilibrium depletion layer was considered below the substrate interface. The thickness of the depletion layer was calculated from the carrier density of the doped layer. For ion implanted substrates, since the doping in the active layer is not uniform, as shown in Figure 5.11, the doped layers were modeled by a step function with step as thin as 0.05 μm. The s-parameters were then used to calculate the RF loss as a function of frequency. The RF loss curve was obtained as a function of the substrate carrier concentration n at different frequencies. The simulated loss curves for the CPWD18 structure on ion implanted substrates as a function of n at various frequencies are given in Figure 5.15. The experimentally measured losses for the ion-implanted samples are also shown for comparison. Given that the theoretical calculation is from first principles, and no free parameters were used to carry out the calculations, the agreement with experimental measurements is found to be quite reasonable. A good agreement is obtained, considering the fact that the activation was assumed independent of dose and the percent activation may have been slightly overestimated. As shown in Figure 5.15, theoretical simulation has underestimated the onsets of the loss curves compared to the experimental results.

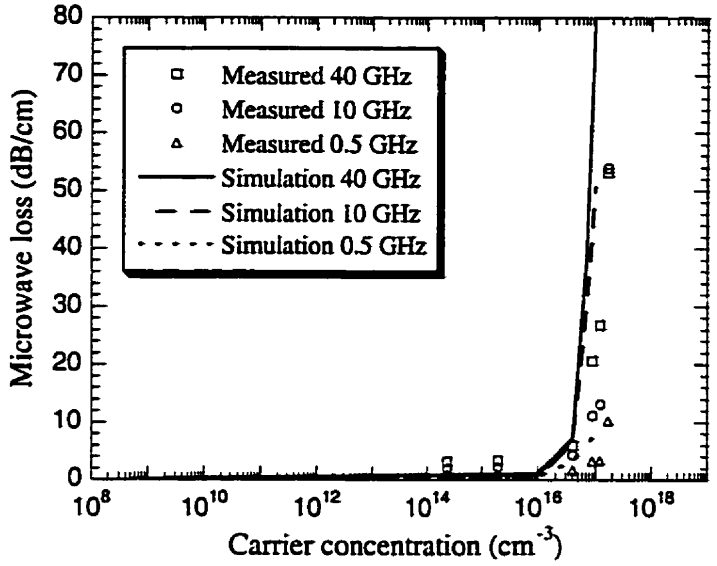

Figure 5.15 Measured and simulated microwave loss variation with substrate carrier density at different frequencies.

Therefore, substrate carrier concentration may be slightly higher than what simulation predicts as the loss curve onset.

It is clear by now that the integration of slow wave planar structures with ridge optical waveguides requires semiconductor heterostructure material with doping below a critical value in the vicinity of 5×10^{14} cm^{-3}. To verify the validity of the results, the heterostructure optical waveguide given in wafer #1, NORTELTECH MBE 2287, was designed with epitaxial layers carrier density of almost 1×10^{14} cm^{-3}. The parameters of this heterostructure optical waveguide to be used for traveling wave electro-optic modulators are given in Figure 3.1. This results in 6 μm of doped layer under the CPW electrodes. The model developed in this work was used to study the microwave loss variation with substrate doping for this kind of epitaxial material. For the purpose of the model, the doping in the active layer is considered to be uniform. The combination of the active layer and the depletion layer was taken to be 6 μm. As mentioned earlier, since the onset of the loss curve is independent of frequency, this simulation was performed only at one frequency, 40 GHz, shown in Figure 5.16. The microwave loss measured for CPWD18 on this substrate is close to 5 dB/cm, almost 2 dB/cm higher than for SI-GaAs

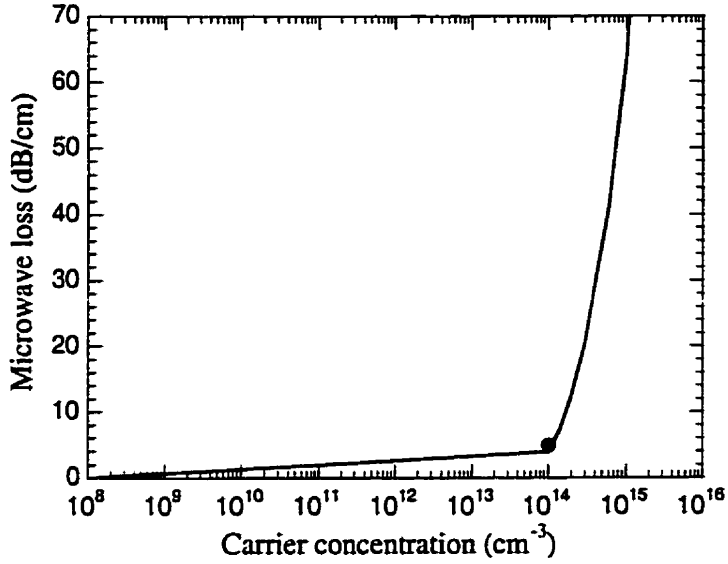

Figure 5.16 Measured and simulated results showing microwave loss variation with substrate carrier density at 40 GHz for 6 μm thick doped epitaxial material.

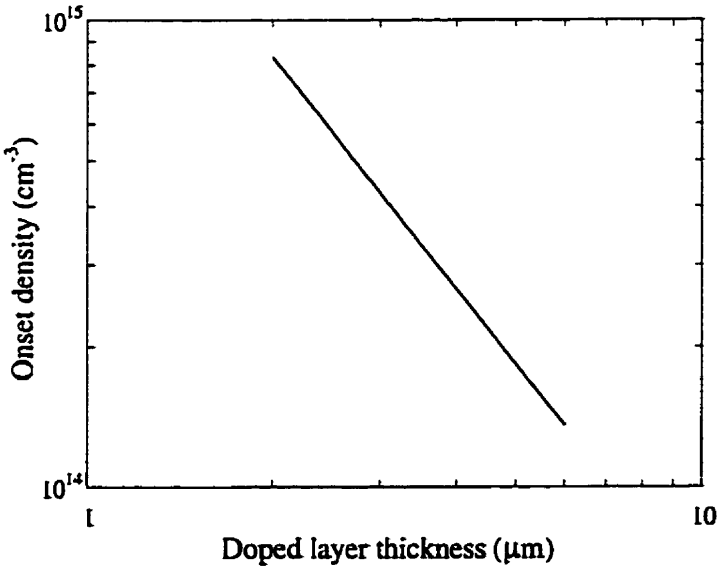

Figure 5.17 Simulation results for the relationship between the thickness of the uniform doped layer and the onset density.

substrates. This is in good agreement with the predictions of our model. This point is shown in Figure 5.15 to compare with the simulation results. Figure 5.17 shows the simulation results for the relationship between the thickness of a uniform doped layer and

the onset density of the loss curve. As the doped layer gets thinner, the onset density increases exponentially.

We have investigated the theoretical and experimental relationship between the microwave insertion loss in planar electrodes as function of substrate carrier concentration. This study was performed for both epitaxial grown materials and ion implanted substrates using Si_{29}. It was observed that there is a critical value in the microwave loss curves as a function of substrate doping after which the microwave insertion loss increases rapidly with doping. It was also shown that the onset is frequency independent, but the rate of increase in loss is a function of frequency. It was found that the carrier concentration of the substrate used in electro-optic modulation applications must not exceed 5×10^{14} cm^{-3}.

5.4 Electro-optical properties

The electro-optical properties of modulators are presented in three subsections. Each subsection describing a specific type of modulator, e.g., polarization/mode converter, and polarization sensitive modulator, contains measurement results on device transfer function and frequency response.

5.4.1 Polarization sensitive modulators

As discussed in chapter 2, polarization sensitive devices are only modulating the TE polarized optical signal propagating in a waveguide along $[0\bar{1}1]$ direction. The modulating electric field is in [100] direction, perpendicular to the substrate surface. Therefore, a TE polarized input optical signal is launched into the input optical waveguide of the device and the output signal is directly detected by an optical detector. In the following measurements, a TE polarized signal with polarization extinction ratio of 25 dB is used as input signal. Two different types of slow wave structures, CPW, CPWD-

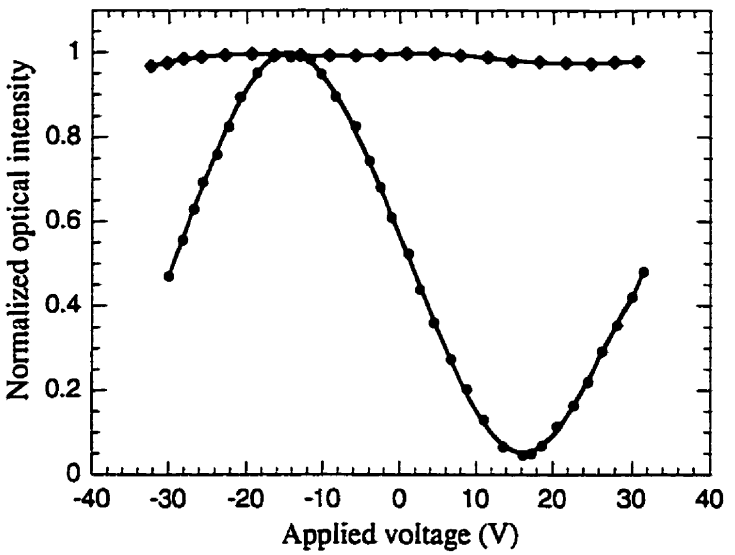

Figure 5.18 Normalized transfer function of the intensity modulator with CPWD-as21 electrode structure on LIT-2 mask fabricated on wafer #1 for TE (circle) and TM (diamond) input signals.

as, and CPSD-id, designed and integrated with optical MZ interferometer. These two electrode types are discussed separately.

5.4.1.1 CPWD and CPWD-as slow wave structures

These two electrode structures are very similar. CPWD-as is a modified version of CPWD to enable the designer to increase the longitudinal overlap factor, Γ_l, of the modulator. Therefore, results are given only for CPWD-as structures. LIT-2 mask set contained one CPWD-as electrode, CPWD-as21, with Γ_l of 0.6 and interelectrode gap, S, 0f 4 μm. The Transfer functions for this device as a function of applied voltage are given in Figure 5.18. The modulator half-wave voltages, the voltage difference between on and off state, is about 30 V. This high switching voltage is mainly due to three factors, low Γ_l and Γ_s and high S. The other modulators with CPWD electrode structure demonstrated switching voltage of 32 V to 35 V. This figure also shows the device transfer function when the input optical signal is TM polarized. The output signal is not modulated over the entire voltage scanning range. As mentioned earlier, LIT-3 mask set was designed to

improve the modulator performance by increasing (Γ_l. Γ_s) / S. The transfer function of a modulator with CPWD-as8 electrode structure on LIT-3 is depicted in Figure 5.19. The half-wave voltage is significantly reduced by a factor of 3.5 to 8.5 V. The on-off extinction ratio is 13 dB. Considering the increase in the length of the device and Γ_l / S and improved optical waveguide design for smaller mode size, a half-wave voltage of much less than 8.5 V is expected for devices on LIT-3 mask set. Therefore, the transversal overlap factor, Γ_s, has not changed from LIT-2 to LIT-3 design.

There are two main factors in limiting the on-off extinction ratio of the polarization sensitive modulators. First, any degradation in polarization extinction ratio of the input optical signal will reduce the total on-off extinction ratio. There is no analyzer between the output waveguide and the detector, and TM polarized signal is not modulated. Residual TM polarization in the optical signal could be due to low polarization extinction ratio of the laser source, fiber connectors, and any coupling between the two polarization states. The other factor that affects the on-off extinction ratio is the asymmetry in the input Y-junction. If the input optical signal is not equally divided into two arms of the MZ interferometer, a complete destructive recombination

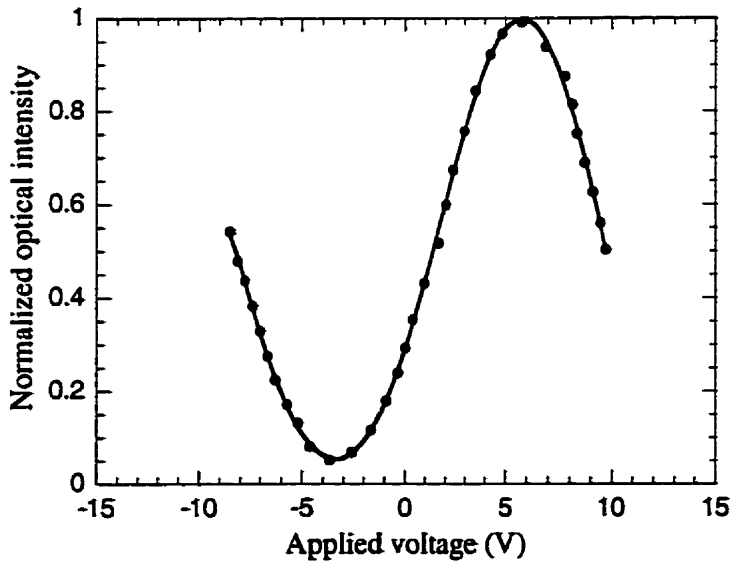

Figure 5.19 Normalized transfer function of the intensity modulator with CPWD-as8 electrode structure on LIT-3 mask fabricated on wafer #2.

will not occur at the output Y-junction that will also limit the on-off extinction ratio.

It is also worth mentioning that if the MZ interferometer is completely symmetric, equal optical path length for the two arms of MZ interferometer, the transfer function maximum occurs at zero bias voltage due to constructive recombination of power at the output Y-junction. However if there is any optical path length difference between the two arms, the maximum shifts to another point. Free space optical wavelength of 1.55 μm in equivalent to 0.47 μm in GaAs/AlGaAs material. An optical path length difference of as low as 0.235 μm can instead shift a minimum point to the zero bias voltage. This small difference can easily happen on these long devices, over 1 cm. Material and processing quality and parameters vary over the large piece of substrate. Examining Figures 5.18 and 5.19 and other measured transfer functions demonstrates the difficulty of achieving equal optical path length for the two arms of MZ interferometer. This asymmetry does not impose any problem on this type of modulators other than shifting the dc bias voltage for a given device. This, however, impose a major problem in the design of polarization insensitive modulators. As mentioned in chapter two, any phase difference between two arms of MZ interferometer in polarization independent modulator severely degrades the polarization insensitivity of the device. As Γ_i increases, the on-off switching voltage of these modulators declines. For example, CPWD-as11 demonstrated on-off switching voltage of 11 V, an increase of almost 30%.

The modulation frequency spectrums of these modulators were measured using conventional method up to 20 GHz and heterodyne method from 20 GHz to 40 GHz. The modulation frequency response of CPWD-as8 on LIT-3 is depicted in Figure 5.20. As mentioned in the last chapter, the measured frequency response is the electrical spectrum of an optical signal measured using an electrical spectrum analyzer. Therefore, 3-dB optical modulation frequency roll-off is equivalent to 6-dB electrical roll-off. The response is quite flat over the frequency range and the 6-dB frequency roll-off was not observed. Figure 5.21 shows the microwave measurement results on this modulator. The velocity match is better than 5% over the entire frequency range. Characteristic impedance of the device is about 43 and almost flat. The Microwave insertion loss is 7

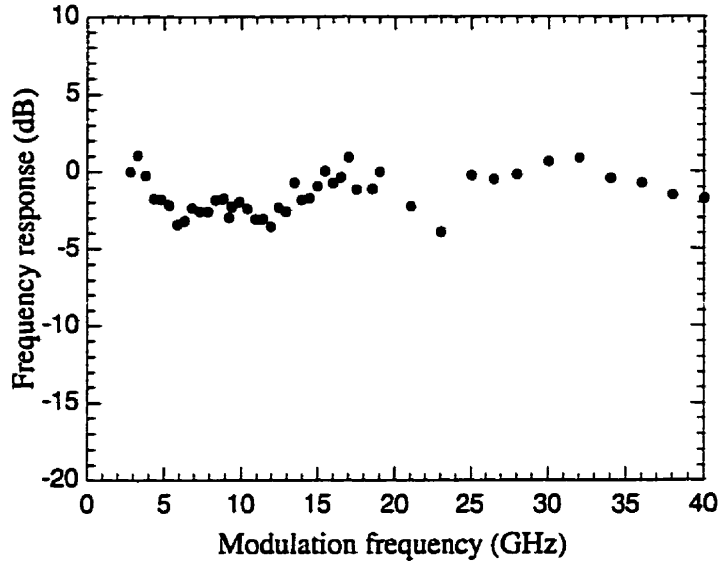

Figure 5.20 Normalized modulation frequency spectrum of CPWD-as8 modulator as a function of frequency.

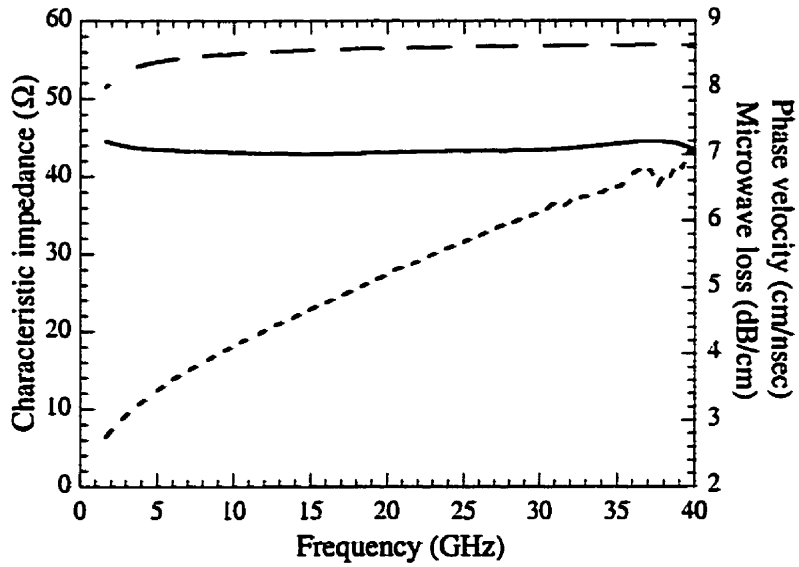

Figure 5.21 Measured characteristic impedance (solid), phase velocity (dashed), and Microwave loss (dotted) as a function of frequency for CPWD-as8 on LIT-3 mask fabricated on wafer #2.

dB/cm at 40 GHz, about 2 dB/cm higher than on SI-GaAS substrate, see Appendix IV. As mentioned in section 5.2, metal thickness of 0.85 μm on LIT-3 rather than 1.5 μm on LIT-2 has contributed to the rather high insertion loss.

5.4.1.2 CPSD-id slow wave structures

The main advantage of CPSD-id slow wave electrode over CPWD-as electrodes is the absence of a narrow signal electrode in the centre. The narrow width of signal electrode in CPWD-as structure helps the designer to increase the longitudinal overlap factor, Γ_l, while maintaining a narrow interelectrode gap, S. The high current density on this narrow signal electrode, as shown in Figure 3.4, increases the microwave insertion loss and that in turns reduces the modulation bandwidth. On the other hand, signal electrode in a CPSD-id structure has the same width as the ground electrode. This results in lower microwave insertion loss. LIT-2 mask set contained only two CPSD-id electrodes. The normalized transfer function for CPSD-id23 electrodes fabricated on wafer #1 is presented in Figure 5.22. The electrode has a Γ_l of 0.83 and interelectrode gap, S, of 4 μm. The measured half-wave voltage is 19.5 V with on-off extinction ratio of 17 dB. The measured transfer function also suggests that the two arms of the MZ interferometer are not symmetric and there is an optical path length difference between the two arms. The transversal overlap factor, Γ_s, is estimated at 0.5. LIT-3 mask set contained 8 CPSD-id structures with of Γ_l 0.8 to 0.9 and interelectrode gap of 2 to 3 μm.

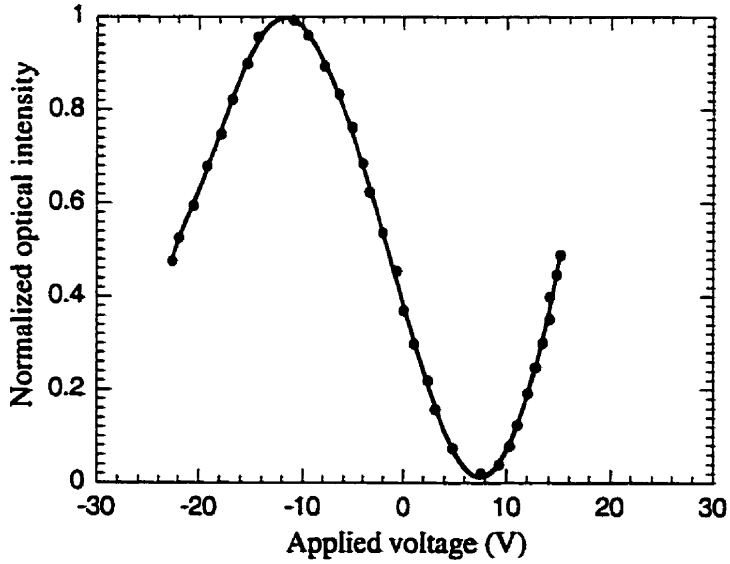

Figure 5.22 Normalized transfer function of the intensity modulator with CPSD-id23 electrode structure on LIT-2 mask fabricated on wafer #1.

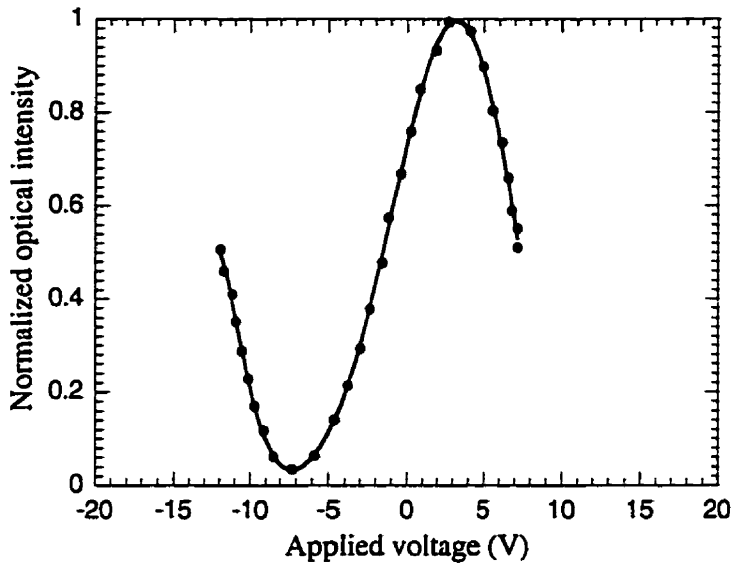

Figure 5.23 Normalized transfer function of the intensity modulator with CPWD-id24 electrode structure on LIT-3 mask fabricated on wafer #2.

Figure 5.23 illustrates the normalized transfer function of CPSD-id24. The half- wave voltage and on-off extinction ratio of the device are 9.5 V and 15 dB, respectively. The other devices demonstrated half-wave voltage of 9.5 V to 11.5 V. The extinction ratio did not vary significantly among different CPSD-id structures. Modulation spectrum of this modulator is given in Figure 5.24. The frequency response is mainly flat and the 6-dB roll-off was not observed up to 40 GHz. The theoretical bandwidth of this device considering its velocity mismatch and microwave insertion loss is close to 60 GHz. The contra-directional propagation, in which optical and microwave signals are traveling in opposite direction, is also investigated. This simulates the largest possible velocity mismatch between two signals. This case results in lowest modulation bandwidth. The modulation spectrum of the modulator under this situation is depicted in Figure 5.25. This results in modulation bandwidth of less than 3.5 GHz. The microwave measurements including characteristic impedance, phase velocity, and insertion loss of this electrode is given in Figure 5.26. The device demonstrates close impedance match to 50 Ω, velocity mismatch of less than 5% over the entire frequency range, and microwave loss of 6 dB/cm at 40 GHz. This loss is about 1 dB/cm less than CPWD-as8 given in Figure 5.21.

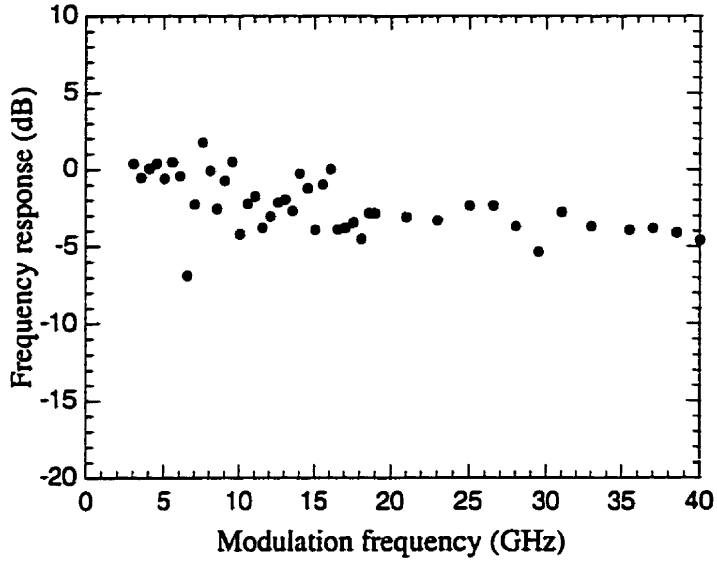

Figure 5.24 Normalized modulation frequency spectrum of CPSD-id24 modulator as a function of frequency.

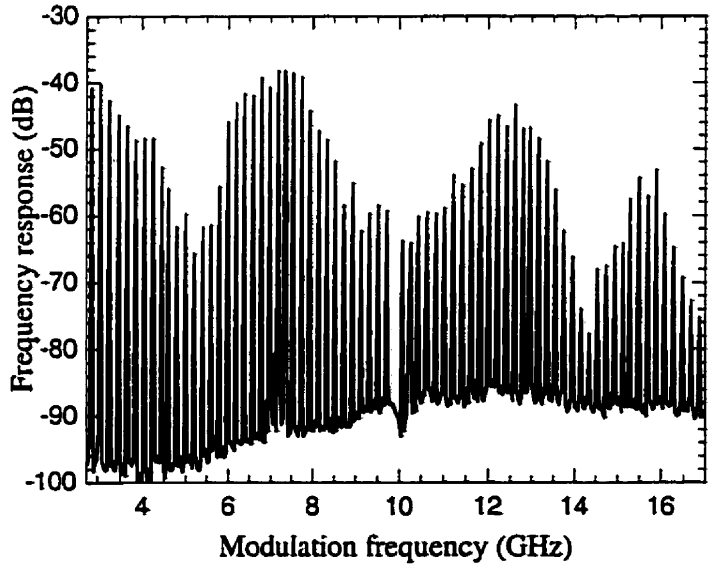

Figure 5.25 Modulation frequency spectrum of CPSD-id24 modulator for contra-directional propagation.

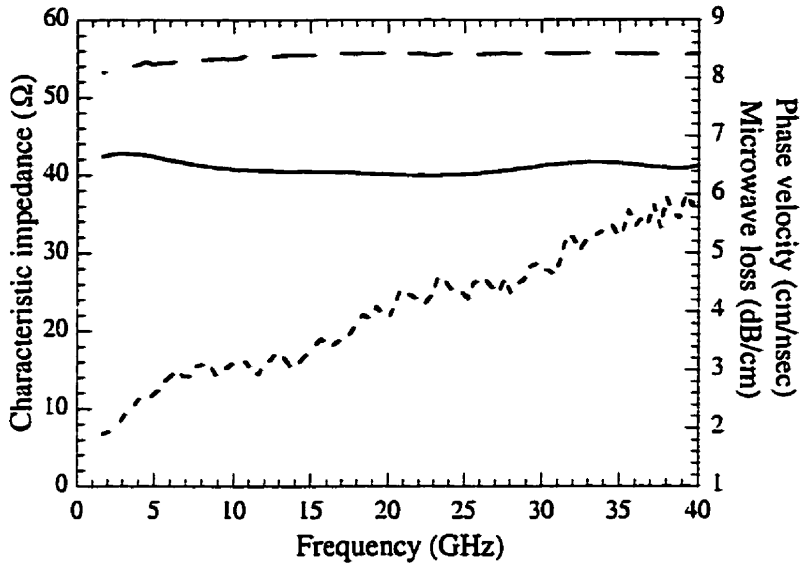

Figure 5.26 Measured characteristic impedance (solid), phase velocity (dashed), and Microwave loss (dotted) as a function of frequency for CPSD-id24 on LIT-3 mask fabricated on wafer #2.

5.4.2 Polarization/mode converters

Polarization/mode converters in conjunction with an output analyzer can be utilized as intensity modulators. These devices consist of a coplanar strip integrated with a straight waveguide. CPSD electrode structures designed for these devices offer very low microwave loss with high longitudinal overlap factor, Γ_l, and small interelectrode gap, S. Unfortunately, the mode converters on LIT-3 mask fabricated on wafer #2 were not functioning properly due to high polarization dependent loss observed in the waveguide. The following measurement was performed to reconfirm this point. A TE input optical signal was launched into a mode converter on wafer #2 and an electrical signal was applied to the electrode. A polarization mean splitter was used at the output to measure the transfer functions for TE and TM modes as a function of applied voltage. The transfer function for total output power was also measured with polarization beam splitter removed. Theoretically, there should be no variation in total output power as a function of applied voltage in mode converters. The power simply should be exchanged

between the two modes while the total power remains constant. Output TE and TM modes should demonstrate complementary transfer function as discussed in Chapter 2. However, the TM transfer function was almost flat across the scanning voltage range with very low power. The transfer functions for TE and total power were very similar in behavior and power level. It is believed that this phenomenon is due to high polarization dependent loss in waveguide that heavily attenuates one mode and passes the other mode unattenuated. A charge discharge affect was also observed in particular in the measurement of polarization independent modulators. When a bias voltage was applied to the electrode, the change in the transfer function was instantaneous. When the bias was removed, the change in the transfer function was gradual. This is believed to be due to impurities in the dielectric layer deposited between semiconductor and metallization. This would not have significant effect on the operation of polarization dependent modulators, since they are only operating on TE mode. The other effect would be a shift in the transfer function of the device to the right or left.

The responses of these modulators vary depending upon input polarization and output analyzer. A TE optical signal is launched into the device and the output signal is detected after passing through a TM analyzer. Figure 5.27 shows the normalized transfer

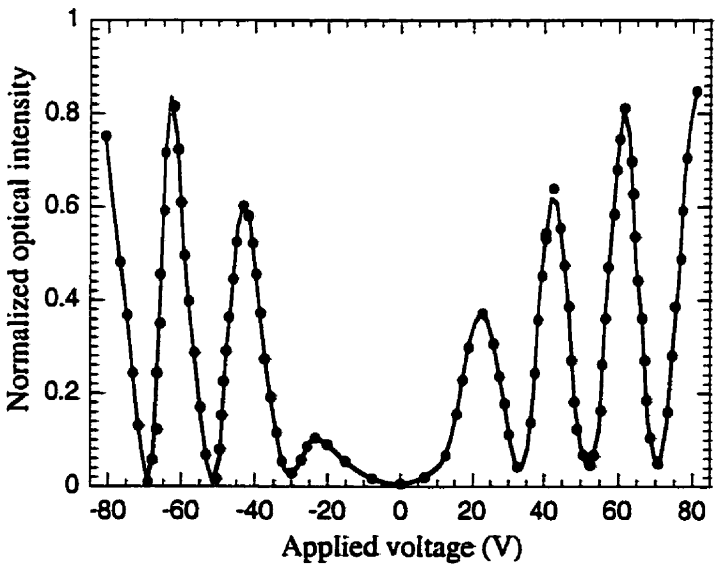

Figure 5.27 Normalized transfer function of the intensity modulator with CPSD5 electrode structure on LIT-2 mask fabricated on wafer #1.

function of CPSD5 on LIT-2 fabricated on wafer #1. CPSD5 slow-wave electrode has an interelectrode gap, S, of 4 μm and Γ_l of 0.83. A half-wave voltage of 9 V was achieved at the bias voltage of +65 V. A similar situation exists for negative bias point. It is instructive to compare these results with the one for CPSD-id23 given in Figure 5.22. Both structures have the same S and Γ_l. and fabricated on the same substrate. The waveguide width for both modulators is 3 μm. However, CPSD-id23 modulator would demonstrate a half-wave voltage of 13 V if its length was equal to the length of CPSD5 electrode, 1.5 cm. In other words, CPSD mode converters offer lower half-wave voltage than CPSD-id modulators. This is mainly due to the push-pull effect between the two polarization states given by Equation 2.9. Provided that transversal overlap factors of two modulators are similar, this effect reduces the half-wave voltage of CPSD mode converters by a factor of 2 compared to CPSD-id modulators. On the other side, there is only 80% coupling efficiency between the two polarization states at 65 V bias. This is equivalent to 1 dB optical insertion loss. One of the main disadvantages of these devices is very low coupling efficiency for birefringent waveguides at low bias voltage. Therefore, efficient performance of these modulators occurs at very high bias voltage. The on-off extinction ratio is better than 12 dB.

The modulation frequency spectrum of CPSD5 is depicted in Figure 5.28. This device also shows a modulation bandwidth in excess of 40 GHz. Characteristic impedance, phase velocity, and microwave insertion loss of this modulator up to 40 GHz are given in Figure 5.29. Again, characteristic impedance and phase velocity are well matched to the design values over the entire frequency range. The microwave insertion losses of CPSD electrodes at 40 GHz are about 1 dB/cm smaller than CPSD-id electrodes both fabricated on wafer #2. The difference is mainly due to the difference in the gap between the main signal and ground electrode, G, between the two electrode structure.

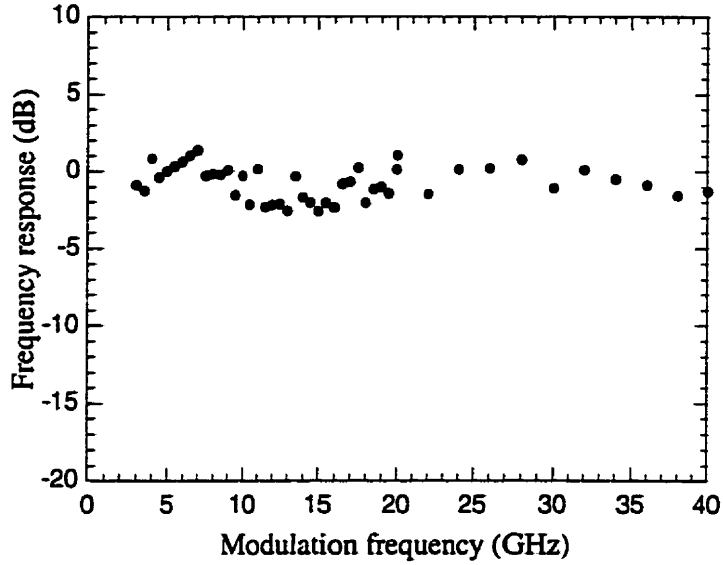

Figure 5.28 Normalized modulation frequency spectrum of CPSD5 modulator on LIT-2 mask fabricated on wafer #1.

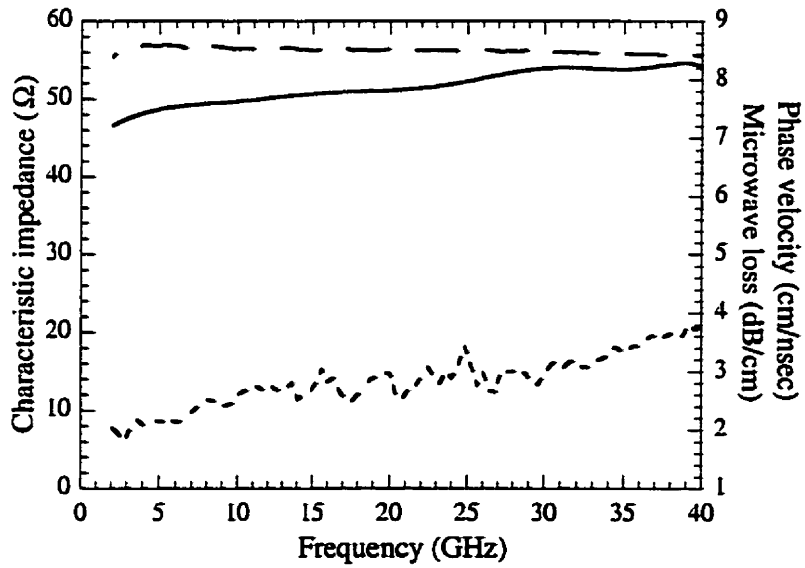

Figure 5.29 Measured characteristic impedance (solid), phase velocity (dashed), and Microwave loss (dotted) as a function of frequency for CPWD-as8 on LIT-3 mask fabricated on wafer #2.

5.4.3 Polarization independent modulators

CPWD-as electrodes were used in the design of polarization independent modulators. The optical ridge waveguide was placed between the signal and ground electrode pads to exploit the transversal electric field in the optical waveguide region. In this modulator, each arm of this MZ interferometer functions as a TE-TM mode converter. Polarization independent modulators on LIT-3 mask fabricated wafer #2 were not operational due to the same reasons mentioned in the last subsection. Therefore, the modulators on LIT-2 mask fabricated on wafer #1 are reported in this section. CPWD-as13 has longitudinal overlap factor, Γ_l, of 0.83 and interelectrode gap, S, of 6 μm.

The calculated effective refractive indices of the optical waveguide for TE and TM modes are 3.3232 and 3.3230 at 1.55 μm, respectively. This results in a modal birefringence of $n_{TE} - n_{TM} \cong 0.0002$. Although the amount of this modal birefringence in our optical waveguide is very small, it degrades the performance of the device from the ideal case.

The slow-wave CPW shows a characteristic impedance of 47 Ω, microwave loss of 5.6 dB/cm at 40 GHz, and a phase velocity mismatch of less than 5% over the measured frequency range.

A 1.55 μm TE or TM mode optical signal is launched into the optical waveguide of the device through a single mode polarization maintaining (PM) fiber. The output optical signal of the modulator is then collected by another PM fiber and is detected by the optical detector. A 5 KHz signal is applied to the CPW in three different biasing configurations to obtain the modulator transfer functions.

1. The signal is applied to the center electrode and the two side electrodes are grounded. Figure 5.30 shows the measured transfer function for TE and TM polarized input optical signals. The device shows half-wave voltage of 16 and 15.5 V, and on-off extinction ratio of 8.8 and 11.2 dB for TE and TM input polarization states, respectively. The extinction ratio is mainly limited by the modal birefringence of the optical waveguide.

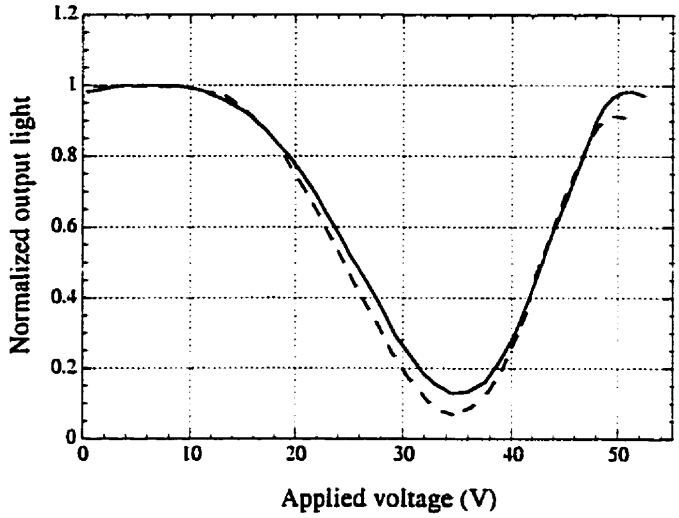

Figure 5.30 Normalized transfer function of CPWD-as13 modulator on LIT-2 mask fabricated on wafer #1 for TE (solid) and TM (dashed) polarized input optical signals. RF signal is applied to the centre electrode and side electrodes are grounded.

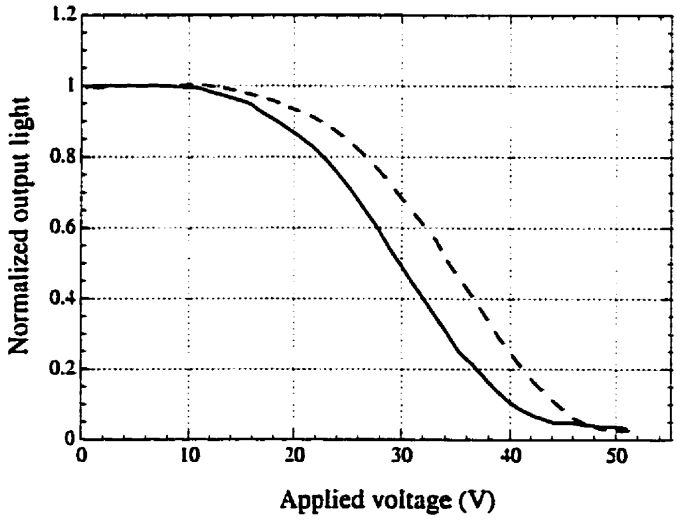

Figure 5.31 Normalized transfer function of CPWD-as13 modulator on LIT-2 mask fabricated on wafer #1 for TE (solid) and TM (dashed) polarized input optical signals. RF signal is applied to one side electrode and centre electrode and the other side electrode is grounded.

2. The center and one of the side electrodes are grounded and the signal is applied to the other side electrodes. The modulation is performed on one arm of the MZ and

therefore V_π is expected to increase by a factor of two. As shown in Figure 5.31, this configuration achieves half-wave voltage of 34 and 35 V, and on-off extinction ratio of 13 and 14 dB for TE and TM input polarization, respectively. As expected, half-wave voltage in this case is almost twice as much as the first case.

3. The signal is applied to the center electrode, one of the side electrodes is biased at 60 V, and the other side electrode is grounded. The modulator transfer function is shown in Figure 5.32. The device shows half-wave voltage of 20.5 and 21 V, and on-off extinction ratio of 20 and 13 dB for TE and TM polarization states, respectively. The 60 V bias point was obtained from modeling of the device.

The biasing configuration (1) and (3) achieve excellent polarization insensitivity while there is some polarization dependency in the second configuration. Considering the limited on-off extinction ratio in the first bias configuration and some polarization sensitivity and high half-wave voltage in the second configuration, the third configuration provides the lowest half-wave voltage for a given on-off extinction ratio. For example, for an on-off extinction ratio 10 dB, half-wave voltage is 14 and 16 V for TE and TM

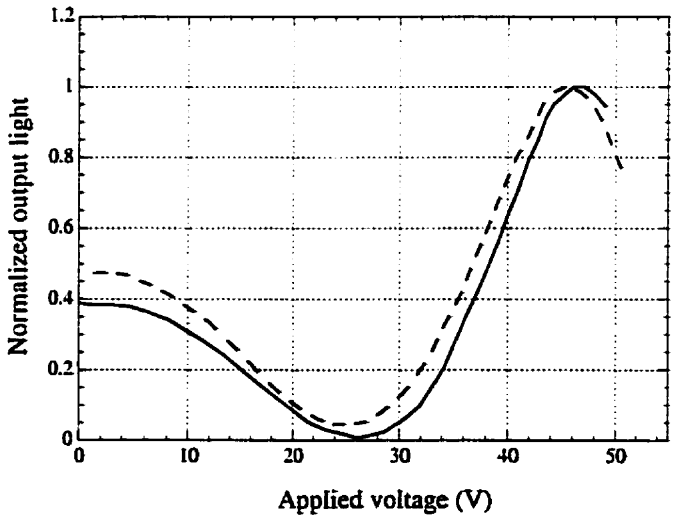

Figure 5.32 Normalized transfer function of CPWD-as13 modulator on LIT-2 mask fabricated on wafer #1 for TE (solid) and TM (dashed) polarized input optical signals. RF signal is applied to the centre electrode, one side electrode is biased at 60 V and the other side electrode is grounded.

polarization states, respectively. These values are the lowest reported for a polarization insensitive traveling wave electro-optic modulator.

The large signal optical modulation frequency response of the device is shown in Figure 5.33. Electro-optic modulation was performed only up to 22 and no significant roll-off was observed in this frequency range.

As discussed in the second chapter, this type of polarization independent electro-optic modulator is highly sensitive to the optical path length difference between two arms of the MZ interferometer. This results in polarization dependency for these modulators. It has been proved to be extremely difficult to fabricate a symmetric MZ interferometer with ridge waveguide on GaAs/AlGaAs material. For example, CPWD-as13 was the only modulator fabricated on wafer #1 that demonstrated to be polarization independent. All other modulators were polarization dependent. The problem of different optical path length for two arms of MZ interferometer was also explained in section 5.4.1. The other factor that affects the performance of the polarization independent modulators as well as polarization converters is that the conventional design of ridge waveguides results in birefringent waveguides. Zero-birefringent waveguides would significantly improve their performance, e.g. very low bias voltage, very high coupling efficiency, and lower half-

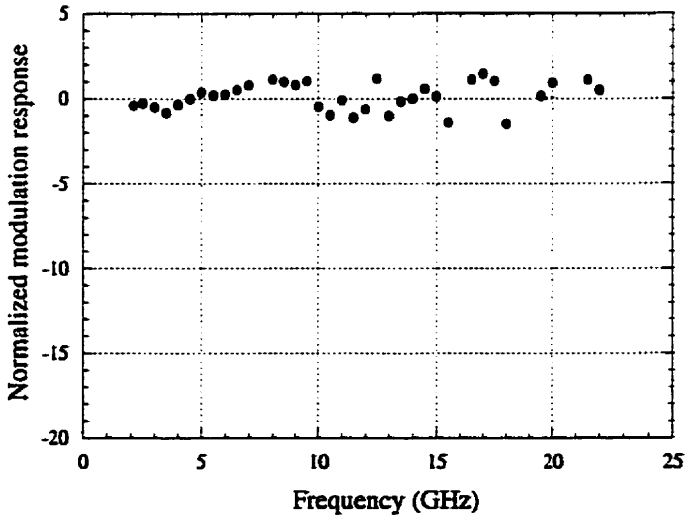

Figure 5.33 Normalized modulation frequency spectrum of CPWD-as13 modulator on LIT-2 mask fabricated on wafer #1.

wave voltage. Fabrication of zero-birefringent waveguides imposes very tight tolerances on the fabrication process such as ridge depth and width.

5.5 Discussion

In this chapter, optical properties of waveguides fabricated on wafer #1 through wafer #5 using LIT-2 and LIT-3 mask sets were presented. This included the optical insertion loss for TE and TM modes. Optical waveguides on wafer #2 demonstrated high polarization dependent loss that affected the performance of mode converters and polarization independent modulators. Electrical measurement was performed on both semi-insulating and epitaxially grown materials. The measurement results on the semi-insulating materials were used in the fine-tuning in the subsequent designs. Material characterization was a major part of this chapter. An upper limit on the carrier concentration of the substrate, 5×10^{14} cm^{-3}, was established to minimize its effect on the microwave insertion loss. Different modulators including polarization dependent and independent modulators and mode converters were measured for transfer function and modulation spectrum. Half-wave voltage of as low as 8.5 V, on-off extinction ratio of 13 dB, and modulation bandwidth of over 40 GHz were measured.

In the next chapter, a discussion on the results, advantages and disadvantages of each modulator, and their application in a high-speed optical network will be presented. We will also discuss the methods to improve the performance of these modulators. A discussion on the future work will be given at the end of next chapter.

Chapter 6

Discussion and Conclusion

This section presents a discussion about the extent to which the modulators described in this thesis meet the requirements as described in chapter 2, as well as recommendations on how the traveling wave electro-optic modulators can be improved. The purpose of the research described in this thesis was the development and characterization of large bandwidth semiconductor external laser modulators using slow wave electrode structures. The capacitively loaded planar electrode enables the designer to reduce the phase velocity of microwave signal traveling along the electrodes and therefore to match that to the group velocity of the optical signal propagating down the optical waveguide. Low microwave insertion loss of the electrode plays a critical role in extending the modulation bandwidth when the velocity mismatch is better than 5%. At larger velocity mismatch, the effect of microwave loss on modulation bandwidth is less severe. The use of coplanar structures also minimizes the microwave signal dispersion, which extends the velocity match to millimeter frequency range. Non-planar electrodes such as microstrip lines are not suitable candidates for these types of applications due to the large dispersion observed in the microwave signal. This is mainly due to the propagation of hybrid modes rather than Quasi-TEM modes. Semiconductor materials

such as GaAs and InP were chosen for their potential to be monolithically integrated with the laser sources.

The first problem encountered with the use of semiconductor materials as the substrate was the high carrier concentration of the epitaxially grown layers. This substantially increases the microwave loss of the electrode that in turn limits the modulation bandwidth of the modulator. A detailed study of the subject revealed that the carrier density of the substrate and epitaxial layers should not exceed a certain value in order to minimize the microwave loss. This was demonstrated with both epitaxially grown materials and ion implanted substrates. The carrier concentration of the substrate has to be less than the onset value of 5×10^{14} cm^{-3}. Previously, researchers have used "unintentionally" doped substrates for electro-optic modulation applications. The levels of carrier concentration in these materials have not been determined which could be in the 1×10^{14} cm^{-3} to 5×10^{16} cm^{-3} range. The onset value is a function of the doped layer thickness. The onset value decreases as the thickness of the doped layer increases. Ion implanted substrates with doped layer thickness of about 2000 Å show an onset value of about 7×10^{16} cm^{-3}. Substrate carrier concentrations in excess of these values cause an exponential increase in the microwave loss. Therefore, all epitaxially grown optical structures for this research satisfied this requirement.

Low microwave insertion loss and velocity match are the most important parameters of a slow wave electrode to be considered in the design of high-speed traveling wave electro-optic modulators. These parameters are the main factor in the determination of modulation bandwidth. Different sources including substrate carrier concentration and electrode metallization contribute to microwave insertion loss. Losses due to electrode metallization depend on the physical geometry of the electrode. The research started with the design of different slow wave electrodes to evaluate their performance in terms of microwave loss, slowing of the microwave signal, and transversal and longitudinal overlap factor. The LIT-1 mask set consists of five different slow wave electrode configurations including CPW, CPWA, CPWB, CPWC, CPWD (see Appendix I). It was concluded that CPWD outperforms other structures as it provides less microwave loss, α_m, narrower interelectrode gap, S, larger longitudinal overlap factor, Γ_l,

without overslowing the microwave signal. We also introduced asymmetric CPWD-as, and CPSD-id in the second generation of mask, LIT-2, along with CPSD electrodes. It was found that α_m is a function of the gap between the main section of signal and ground electrodes, G, along which major part of current is flowing. It is also a function of signal electrode width. LIT-3 mask set included the optimized design for CPSD, CPWD-as, and CPSD-id electrode structure. CPWD-as electrodes offer higher Γ_l for a given interelectrode gap than symmetric CPWD due to lower capacitance of the asymmetric T-railed elements. It can achieve Γ_l as high as 90-95% with S as low as 2.5 μm and α_m as low as 5 dB/cm on SI-GaAs substrate. CPSD electrodes demonstrated the least microwave insertion loss. They offer microwave loss of about 2 dB/cm less than CPWD-as electrodes with the same Γ_l and S. CPSD-id electrodes showed a modest microwave performance in terms of loss. They demonstrated microwave loss of about 1 dB/cm more than CPSD's. Proper design of CPSD-id electrodes would result in microwave losses as low as CPDS's. All our slow wave electrodes achieved excellent impedance and velocity matching conditions. Phase velocities were matched to about 5% of the target value over the entire frequency range. Characteristic impedance of the electrodes was mostly between 43 Ω to 53 Ω.

Optical waveguides fabricated on wafer #2 showed significant polarization dependent loss (PDL) of 7 to 10 dB. PDL for optical waveguides on wafer #1 was less than 1 dB. This is believed to be due to the impurities in the dielectric layer deposited between electrode and semiconductor. The presence of such high PDL prevented the proper operation of mode converters and polarization independent modulators.

Two types of electrode, CPWD-as and CPSD-id, were employed in the design of polarization dependent modulators. A polarization dependent modulator is obtained if the arms of the MZI are positioned under the electrode pads. The phase of the optical TE mode in each arm of the MZI is modulated while TM mode is unaffected. CPSD-id electrodes achieved half wave voltage of 9.5 V at on-off extinction ratio of 15 dB. The half-wave voltage and on-off extinction ratio for CPWD-as electrodes were measured to be 8.5 V and 13 dB, respectively. The half-wave voltage of these modulators increased to

11.5 V as Γ_l decreased from 0.9 to 0.75. These values are the lowest half-wave voltages ever reported for traveling wave electro-optic modulators on GaAs/AlGaAs material. The bandwidths of these modulators were measured up to 20 GHz using conventional methods and from 20 GHz to 40 GHz using heterodyne techniques. They demonstrated a relatively flat frequency response. The 6-dB bandwidth roll-off was not observed up to 40 GHz.

A CPSD electrode is integrated with a straight optical waveguide to operate as a polarization/mode converter. A polarizer and an analyzer have to be integrated at the input and output of the device, respectively, to modulate the intensity of the incoming optical signal. The operation of CPSD polarization/mode converter as intensity modulator is highly polarization dependent. This also increases optical insertion loss as well as the length of the device. The polarization extinction ratio of such device would be of some concern too. The normalized transfer function for TE and TM modes are complementary. A half wave voltage of 9 V at bias voltage of +65 V with an on-off extinction ratio of about 12 dB was measured for this device. The modal birefringence of optical waveguides severely deteriorates the performance of mode converters. It reduces the coupling efficiency between two modes and necessitates the application of a large bias voltage. Employing zero-birefringence optical waveguides in polarization/mode converter and MZ polarization independent modulators significantly lowers the bias voltage and increases the on-off extinction ratio. The coupling efficiency between TE and TM modes is 80% at +65 V bias point. Mode converters with larger interelectrode gap had higher half-wave voltage at a higher bias point with less coupling efficiency. CPSD mode converters demonstrated lower half-wave voltage than CPSD-id polarization dependent modulators by almost 30% for similar electrode physical dimensions. This is believed to be mainly due to the push-pull effect in mode conversion. Modulation bandwidth of mode converters exceeds 40 GHz, as shown in Table 6.1. Unfortunately mode converters on LIT-3 mask could not be tested due to high polarization dependent loss in optical waveguides.

Today's commercial lasers offer highly polarized output signal. We have used a DFB laser with polarization extinction ratio of over 25 dB. If such a laser is to be

Table 6.1 Specifications of some of the modulators tested for this research.

Modulator type	Polarization dependent		Mode converter	Polarization independent
Electrode Type	CPWD-as	CPSD-id	CPSD	CPWD-as
Half-wave voltage (V)	8.5	9.5	9	14
On-off extinction ratio (dB)	13	13	12	10
Measured bandwidth (GHz)	> 40	> 40	> 40	>22
Velocity mismatch	< 5%	< 5%	< 5%	< 5%
Microwave loss at 40 GHz (dB/cm)	6.9	5.9	3.8	5.6

integrated or connected using a PM fiber with one of the polarization sensitive modulators or mode converters, polarization sensitivity is not of great concern. Therefore, as long as modulators are used in the close vicinity of laser source, polarization sensitive modulators can perform as well as polarization insensitive modulators. However, applications of polarization independent devices are critical to network operation if they are to be used where the input polarization is random. As mentioned in the first chapter, spatial optical switches are modified version of MZ modulator. They are used as routers in the network and are required to be polarization independent. The techniques used in the development of polarization independent modulators can also be beneficial in the design of high-speed polarization independent electro-optic switches. It was shown that polarization insensitive modulation is only possible when a slow wave coplanar waveguide is integrated with a MZ optical interferometer with electrodes positioned on either side of the optical waveguide on a [100] flat substrate. The electric field component parallel to the substrate is exploited to modulate the polarization states in each arm of the MZI. It was also shown that the optical path length difference between the two arms of MZ interferometer severely affects the polarization insensitivity. We have demonstrated the operation of polarization insensitive modulators with half wave voltage of 14 V and on-off extinction ratio of more than 10 dB and modulation bandwidth of over 22 GHz. These are the best ever-reported values for a polarization independent traveling wave electro-optic modulator. One side electrode of the coplanar waveguide has to be biased to increase the on-off extinction ratio at lower half wave voltages. The challenge is

to fabricate symmetric MZ interferometer over such a long device. At 1.55 μm free space wavelength, 0.235 μm optical path length is equivalent to half a wavelength in GaAs/AlGaAs material. Enormous complexity on the fabrication process is required to achieve such an accuracy for such long devices. Therefore, considering the complexity of the fabrication process and low yield, the design and fabrication of this type of polarization independent modulator is not recommended if it is to be integrated with a polarized laser or to be used in its proximity.

CPSD-id polarization dependent modulators and CPSD mode converters are the modulators of choice for the following reasons: 1) low microwave insertion loss of less than 5 dB/cm on epitaxy materials, 2) excellent impedance and velocity matching over the entire frequency range, 3)very low half-wave voltage and high on-off extinction ratio. If optical waveguides were zero birefringent, CPSD mode converters outperform CPSD-id modulators in terms of half-wave voltage. CPSD mode converters suffer from high bias voltage and low coupling efficiency on birefringent waveguide.

6.1 Future work

It has been shown that traveling wave electro-optic modulators offer the large modulation bandwidth required for high-speed modulation applications. Future research work on this subject can be categorized into three major sections.

1) First is the improvement of devices proposed in this thesis. This includes the design of new electrode and optical structures, the reduction of fiber to waveguide coupling losses, and the design and fabrication of zero-birefringent optical waveguides. New electrode and optical structures are needed to reduce the half-wave voltage and microwave insertion loss. Metallic electrode can consist of two layers. First layer to deposit a thin layer of metal for whole electrode area. The second layer is used to electroplate (thicken) the main section of signal and ground electrodes. This method will reduce the microwave insertion loss and possibly increase transversal overlap factor without compromising the process resolution. The other issue of some concern is the

optical insertion loss. It consists of optical propagation loss and coupling loss between a single mode fiber and the ridge waveguide. Low Optical propagation loss of about 1 dB/cm was obtained by proper design of optical waveguide and material characteristics. Coupling loss of 3-3.5 dB and 6-6.5 dB were measured for wafer #1 and wafer #2, respectively. This off course depends upon the optical waveguide mode size. This results in total optical insertion loss of almost 15 dB for devices on wafer #2. The optical ridge waveguide is small to enable the designer to reduce the interelectrode gap and therefore increase the electric field in the optical waveguide region while maintaining the transversal overlap factor. Different optical mode spot size transformation can also be used to reduce the coupling loss. This can include the design of weakly guided optical waveguide, coupling from a large optical waveguide to the small modulator waveguide. The problem is of less importance if these modulators are to be integrated with the laser source and other electro-optic component on the same substrate. The design of zero birefringence optical waveguides has been shown for different optical waveguides including strip-loaded waveguides as used in this research. This can be achieved by controlling the aspect ratio of the ridge waveguide, the thickness of the core and cladding layers. Although theoretically this seems to be an easy task, it requires a more complex processing technique and optical structure including etch stop layer. It is very sensitive to the waveguide parameters and physical dimensions.

2) The development of new devices such as high-speed spatial switches based on this technology. Spatial switches are required to be polarization independent and therefore the development of symmetric MZ interferometer and zero-birefringent optical waveguide must take place first to lead to an efficient polarization independent modulator. This type of spatial switch would offer switching speed in excess of 40 GHz. This enables the manager of a 10 Gbit/s optical network to dynamically route the signal in less than the duration of a bit.

3) The use of the traveling wave concept in conjunction with the other physical phenomena, and microwave and optical structures to reduce the half-wave voltage of the modulator/switch to less than 5 V. Novel microwave and optical structures have to be developed to increase the longitudinal and transversal overlap factor between the optical

and microwave signals close to 1. We have measured transversal overlap factor close to 0.5. A novel structure that can address some of these problems is currently under investigation. The structure called planar microstrip line (PMS) employs a heavily doped layer under the bottom-cladding layer as the ground plane. This structure results in a transversal overlap factor of close to 1. A slow wave mode also propagates due to the presence of this doped layer. Therefore, a velocity match condition is achieved with uniform coplanar waveguide electrodes. Simulation results show a modulation bandwidth of about 40 GHz. The half wave voltage is less than 4 V in the case of bulk core layer.

Most of the limitations imposed on the design of semiconductor traveling wave electro-optic modulators are due to the very small linear electro-optic coefficient of GaAs and InP materials (r_{41} = 1.4×10^{-12} m/V). The electro-optic coefficient of $LiNbO_3$ is about 10 times larger than GaAs and InP, which makes it attractive for discrete electro-optic modulators.

REFERENCES

[1] T. H. Maiman,"Stimulated optical radiation in ruby masers," *Nature*, vol. 187, pp.493-494, 1960.

[2] F. P. Kapron, D. B. Keck, and R. D. Maurer,"Radiation losses in glass optical waveguides," *Appl. Phys. Lett.*, vol. 17, pp. 423-425, 1970.

[3] E. E. Basch *et al.*,"Introduction to coherent optical fiber transmission," *IEEE Commun. Mag.*, vol. 23, pp. 23-30, May 1985.

[4] T. Li,"Advances in lightwave systems research," *AT&T Tech. J.*, vol. 66, pp. 5-18, Jan/Feb. 1987.

[5] J. R. Barry and E. A. Lee,"Performance of coherent optical receivers," *Proc. IEEE*, vol. 78, No. 8, pp. 1369-1394, Aug. 1990.

[6] P.S. Henry,"Lightwave premer," *IEEE J. Quantum Electron.*, vol. QE-21, No. 12, pp. 1862-1879, 1985.

[7] J. Gowar , *Optical Communication Systems*, Prentice Hall, 1993.

[8] W. B. Jones, *Introduction to optical fiber communication systems*, Holt, Rinehart and Winston, Inc., 1988.

[9] K. Murashige, T. Miyakawa, H. Taga, S. Nakagawa, H. Tanaka, K. Goto, M. Suzuki, and S. Yamamoto,"Sixty 5.3 Gbit/s, 1650-km straight-line WDM transmission," *Optical Fiber Communication Conference*, vol.2, 1998, TUI1.

[10] K. Yonenaga, M. Yoneyama, Y. Miyamoto, K. Hagimoto, and K. Noguchi,"160-Gbit/s WDM transmission experiment using four 40-Gbit/s optical duobinary channels," *Optical Fiber Communication Conference*, vol 2, 1998, TUI2.

[11] A. C. Gossard,"Growth of microstructures by molecular beam epitaxy," *IEEE J. Quantum Electron.*, vol. QE-22, p. 1649, 1986.

[12] M. J. Ludowise,"Metalorganic chemical vapor deposition of III-V semiconductors," *J. Appl. Phys.*, vol. 58, vol. R31, 1985.

[13] S. Fujita *et al.*,"10 Gbit/s, 100 Km optical fiber transmission experiment using high -speed MQW DFB-LD and back illuminated GaInAs APD," *Electron. Lett.*, vol. 25, pp. 702-703, 1989.

[14] B. Wedding,"New method for optical transmission beyond dispersion limit," *Electron. Lett.*, vol. 28, No. 14, pp.1298-1300, July 1992.

[15] S. Weisser, J. D. Ralston, E. C. Larkins, I. Esquivitas, and J. Rosensweig,"Efficient high-speed direct modulation in p-doped $In_{0.35}Ga_{0.65}As$/GaAs multiquantum well lasers," *Electron. Lett.*, vol. 28, pp. 2141-2143, Nov. 1992.

[16] J. B. Georges, M. H. Kiang, K. Heppell, M. Sayed, and K. Y. Lan,"Optical transmission of narrow-band millimeter-wave signals by resonant modulation of monolithic semiconductor lasers," *IEEE Photon. Tech. Lett.*, vol. 6, pp. 568-570, 1994.

[17] C. Lawetz, J. C. Cartledge, C. Rolland, and J. Yu,"Modulation characteristics of semiconductor Mach-Zehnder optical modulators," *IEEE J. Lightwave Tech.*, vol. 15, No. 4, pp. 697-702, 1997.

[18] T. H. Wood,"Multiple quantum well (MQW) waveguide modulators," *J. Lightwave Tech.*, vol. 6, pp. 743-757, June 1988.

[19] S. Y. Wang and S. H. Lin,"High-speed III-V electro-optic waveguide modulators at $\lambda = 1.3$ μm," *J. Lightwave Tech.*, vol. 6, pp. 758-771, June 1988.

[20] G. E. Stillman, C. M. Wolfe, C. V. Bozler, and J. A. Rossi,"Electroabsorption in GaAs and its application to waveguide detector and modulator," *Appl. Phys. Lett.*, vol. 28, pp. 544-546, 1976.

[21] F. Stern, *Elementary theory of the optical properties of solides*, in Sloid State Physics, F. Seitz and D. Turnball Eds. New York: Academic, vol. 15, 1963.

[22] A. Alping and L. A. Coldren,"Electrorefraction in GaAs and InGaAsP and its application to phase modulators," J. Appl. Phys., vol. 61, No. 7, pp. 2430-2433, 1987.

[23] J. E. Zucker, K. L. Jones, B. I. Miller, and U. Koren,"Miniature Mach-Zehnder InGaAsP quantum well waveguide interferometers for 1.3 μm," *IEEE Photon. Tech. Lett.*, vol. 2, pp. 32-34, 1990.

[24] I. P. Kaminow, *An Introduction to Electro-optic Devices*, New York, Academic Press, 1974.

[25] S. K. Korotky, G. Eisenstein, R. S. Tucker, J. J. Veselka, and G. Raybon,"Optical intensity modulation to 40 GHz using a waveguide electrooptic switch," *Appl. Phys. Lett.*, vol. 50, pp. 1631-1633, 1987.

[26] I. P. Kaminow and E. H. Turner,"Electrooptic light modulators," *Proc. IEEE*, vol. 54, pp. 1374-1390. Oct. 1966.

[27] F. S. Chen,"Modulators for optical communications," *Proc. IEEE*, vol. 58, pp. 1440-1457, Oct. 1970.

[28] H. Takeuchi, Y. Hasumi, K. Kondo, and Y. Noguchi,"4x4 Directional coupler switch matrix with an InGaAlAs/InAlAs multiple quantum well structure," *Electron. Lett.*, vol. 29, No. 6, pp. 441-443, 1992.

[29] T. Aizawa, Y. Nagasawa, K. G. Ravikumar, and T. Watanabe," Polarization-independent switching operation in directional coupler using tensile-strained multi-quantum well," *IEEE Photon. Tech. Lett.*, vol. 7, No. 1, pp. 47-49, 1995.

[30] Z. Wanru, D. Jining, Z. Zhenzhong, Y. Peisheng, S. Zhiwen, S. Furong, and G. Junhua,"Total internal reflection optical switch with injection region isolated by ion implantation," *Fiber and Integrated Optics*, vol. 15, pp. 27-36, 1995.

[31] J. E. Zucker, K. L. Jones, T. H. Chiu, B. Tell, and K. Brown-Goebeler,"Strained quantum wells for polarization-independent electro-optic waveguide switches," J. Lightwave Tech., vol. 10, No. 12, pp. 1926-1930, 1992.

[32] N. Agrawal, C. M. Weinert, H. J. Ehrke, G. G. Mekonnen, D. Franke, C. Bornholdt, and R. Langenhorst,"Fast Mach-Zehnder optical space switches using InGaAsP/InP multiquantumwell structures," *IEEE Photon. Tech. Lett.*, vol. 7, No. 6, pp. 644-645, 1995.

[33] R. Alferness,"Waveguide electrooptic modulators," *IEEE Trans. Microwave Theory Tech.*, vol. MTT-30, pp. 1121-1137, 1982.

[34] T. Tamir, Ed., *Guided-Wave Optoelectronics*, Speringer Ser. In Electron. and Photon., vol. 26, Berlin Heidelberg: Speringer-Verlog, 1988.

[35] I. P. Kaminow and J. Liu,"Propagation characteristics of partially loaded two-conductor transmission line for broadband light modulators," *Proc. IEEE*, vol. 51, pp. 132-136, 1963.

[36] H. Haga, M. Izutsu, and T. Sueta,"$LiNbO_3$ traveling wave light modulator/switch with an etched groove," *IEEE J. Quantum Electron.*, vol. QE-22, pp. 902-906, 1986.

[37] K. Noguchi, O. Mitomi, and H. Miyazawa,"Milimeter-wave Ti:$LiNbO_3$ optical modulators," *IEEE J. Lightwave Tech.*, vol. 16, No. 4, pp. 615-619, 1998.

[38] S. Hopfer, Y. Shani, and D. Nir,"A novel, wideband, lithium niobate electro-optic modulator," *IEEE J. Lightwave Tech.*, vol. 16, No. 1, pp. 73-77, 1998.

[39] S. H. Lin, S. Y. Wang, and Y. M. Houng,"GaAs *p-i-n* electro-optic traveling-wave modulator at $\lambda = 1.3$ μm," *Electron. Lett.*, vol. 22, pp. 934-935, June 1986.

[40] S. Y. Wang, S. H. Lin, and Y. M. Houng,"GaAs traveling-wave polarization electrooptic waveguide modulator with bandwidth in excess of 20 GHz at $\lambda = 1.3$ μm," *Appl. Phys. Lett.*, vol. 51, pp. 83-85, 1987.

[41] M. R. Tan, I. Kim, J. Chang, and S. Y. Wang,"Velocity matching of III-V traveling-wave electro-optic modulator structures," *Electron. Lett.*, vol. 26, pp. 32-33, Jan. 1990.

[42] H. Hasegawa, M. Furukawa, and H. Yanai,"Properties of microstrip line on Si-SiO_2 system," *IEEE Trans. Microwave Theory Tech.*, vol. MTT-19, pp. 869-881, 1971.

[43] M. M. Mihailidi, J. E. Zucker, M. D. Feuer, M. N. Khan, T. Y. Chang, and N. J. Sauer,"Microwave properties of traveling-wave InGaAs/InGaAlAs quantum-well optical waveguide modulators," *Microwave Optical Tech. Lett.*, vol. 10, No. 4, pp. 204-207, 1995.

[44] K. S. Giboney, M. J. W. Rodwell, and J. E. Bowers,"Traveling-wave photodetector design and measurements," *IEEE J. Selec. Topics on Quantum Electron.*, vol. 2, No. 3, pp. 622-629, 1996.

[45] Y. J. Chiu, S. B. Fleischer, and E. Bowers,"Subpicosecond (570 fs) response of p-i-n traveling wave photodetector using low-temperature-grown GaAs," *Int. Topical meeting on Microwave Photonics* (MWP'97), Technical digest, pp. 295-297, 1997.

[46] G. W. Hughes and R. M. White,"Microwave properties of nonlinear MIS and Schottky-barrier microstrip," *IEEE Trans. Electron. Devices*, vol. ED-22, pp. 945-956, Oct. 1975.

[47] D. Jaeger,"Slow-wave propagation along variable Schottky-contact microstrip line," *IEEE Trans. Microwave Theory Tech.*, vol. MTT-24, pp. 566-573, Sept. 1976.

[48] Y. Fukuoka and T. Itoh,"Slow-wave coplanar waveguide on periodically doped semiconductor substrate," *IEEE Trans. Microwave Theory Tech.*, vol. MTT-31, pp. 1013-1017, Dec. 1983.

[49] R. D. Alferness, S. K. Korotky, and E. A. J. Marcatili,"Velocity-matching technique for integrated optic traveling wave switch/modulators," *IEEE J. Quantum Electron.*, vol. QE-20, pp. 301-309, March 1984.

[50] N. A. F. Jaeger and Z. K. F. Lee,"Slow-wave electrode for use in compound semiconductor electrooptic modulators," *IEEE J. Quantum Electron.*, vol. QE-28, pp. 1778-1784, Aug. 1992.

[51] R. Spickermann and N. Dagli,"Experimental analysis of millimeter wave coplanar waveguide slow wave structures on GaAs," *IEEE Trans. Microwave Theory Tech.*, vol. 42, pp. 1918-1924, Oct. 1994.

[52] S. R. Sakamoto, R. Spickermann, and N. Dagli," Narrow gap coplanar slow wave electrode for traveling wave electro-optic modulators," *Electron. Lett.*, vol. 31, pp. 1183-1185, July 1995.

[53] R. Spickermann, M. G. Peters, and N. Dagli,"A polarization independent GaAs-AlGaAs electrooptic modulator," *IEEE J. Quantum. Electron.*, vol. 32, pp. 764-769, May 1996.

[54] R. Spickermann, S. R. Sakamoto, M. G. Peters, and N. Dagli,"GaAs/AlGaAs traveling wave electro-optic modulator with an electrical bandwidth > 40 GHz," *Electron. Lett.*, vol. 32, pp. 1095-1096, June 1996.

[55] O. G. Ramer,"Integrated optic electrooptic modulator electrode analysis," *IEEE J. Quantum Electron.*, vol. QE-18, pp. 386-392, March. 1982.

[56] D. Marcuse,"Optimal electrode design for Integrated optics modulators," *IEEE J. Quantum Electron.*, vol. QE-18, pp. 393-398, March. 1982.

[57] S. Namba,"Electro-optic effect of zincblende," *J. Optical Soc. America*, vol. 51, pp. 76-79, Jan. 1961.

[58] K. Tada and N. Suzuki,"Linear electrooptic properties of InP," *JPN J. Appl. Phys.*, vol. 19, pp. 2295-2296, 1980.

[59] A. Yariv,"Coupled mode theory for guided-wave optics," *IEEE J. Quantum. Electron.*, vol. 9, pp. 919-933, Sept. 1973.

[60] H. F. Taylor, and A. Yariv,"Guided wave optics," *IEEE Proc.*, vol. 62, pp. 1044-1060, Aug. 1974.

[61] R. E. Collin, *Foundations for microwave engineering*, 2nd Ed., New York, McGraw Hill, 1992.

[62] A. F. Harvey,"Periodic and guiding structures at microwave frequencies," *IRE Trans. Microwave Theory Tech.*, vol. MTT-8, pp. 30-61, Jan. 1960.

[63] A. Djupsjobacka,"Residual chirp in integrated-optic modulators," *IEEE Photon. Tech. Lett.*, vol. 4, No. 1, pp. 644-645, 1992.

[64] R. J. Deri, and E. Kapon,"Low-loss III-V semiconductor optical waveguides," *IEEE J. Quantum. Electron.*, vol. 27, No. 3, pp. 626-640, March 1991.

[65] C. M. Kim, and R. V. Ramaswamy,"Overlap integral factors in integrated optic modulators and switches," *IEEE J. Lightwave Tech.*, vol. 7, No. 7, pp. 1063-1070, 1989.

[66] G. A. Vawter, C. T. Sullivan, J. R. Wendt, R. E. Smith, H. Q. Hou, and J. F. Klem," Tapered rib Adiabatic following fiber couplers in etched GaAs materials for monolithic spot-size transformation," *IEEE J. Selec. Topics on Quantum Electron.*, vol. 3, No. 6, pp. 1361-1371, 1997.

[67] H. Kogelnik and V. Ramaswamy,"Scaling rules for thin-film optical waveguides," *Appl. Optics*, vol. 13, pp. 1857-1862, Aug. 1974.

[68] J. V. Roey, J. V. D. Donk and P. E. Lagasse,"Beam propagation method: analysis and assessment," *J. Opt. Soc. America*, vol. 71, pp. 803-810, 1981.

[69] L. Thylen, and P. Granestrand,"Integrated optic electrooptic device electrode analysis: the influence of buffer layers," *J. Optic. Comm.*, vol. 7, No. 1, pp. 11-14, 1986.

[70] A. Carenco,"Semiconductor waveguides in III-V materials for integrated optics," *Tech. Dig. Eur. Conf. Integrated Optics* (Glasgow, Scotland), pp. 1-7, 1987.

[71] J. E. Zucker, K. L. Jones, B. I. Miller, M. G. Young, U. Koren, B. Tell, and K. Brown-Goebeler,"Interferometric quantum well modulators with gain," *IEEE J. Lightwave Tech.*, vol. 10, No. 7, pp. 924-932, 1992.

[72] J. E. Zucker,"High-speed quantum-well interferometric modulators for InP-based photonic integrated circuits," *Microwave and Optical Tech. Lett.*, vol. 6, No. 1, pp. 6-14, Jan. 1993.

[73] S. Adachi, *Physical properties of III-V semiconductor compounds*, John wiley & Sons, New York, 1992.

[74] *Prometheus*, BBV Software BV, Hengelosestraat 705, 7521 PA Enschede, The Netherlands.

[75] *Sonnet™ Em User's Manual*, Release 2.4, Sonnet Software, Inc., 135 Old Clover Rd, Liverpool, NY 13090-3773.

[76] G. Gonzales, *Microwave transistor amplifier*, Englewood Cliffs, NJ: Prentice Hall, 1984.

[77] E. H. Bottcher, H. Pfitzenmier, E. Droge, and D. Bimberg,"Millimeter-wave coplanar waveguide slow wave transmission lines on InP," *Elec. Lett.*, vol. 32, pp. 1377-1378, 1996.

[78] R. G. Walker,"Simple and accurate loss measurement technique for semiconductor optical waveguides," *Electron. Lett.*, vol. 21, No. 13, pp. 581-583, June 1985.

[79] D. F. Clark, M. S. Iqbal,"Simple extension to the Fabry-Perot technique for accurate measurement of losses in semiconductor waveguides," *Optics Lett.*, vol. 15, No. 22, pp. 1291-1293, 1990.

[80] R. T. Hawkins II, M. D. Jones, S. H. Pepper, and J. H. Goll,"Comparison of fast photodetector response measurements by optical heterodyne and pulse response technique," *J. Lightwave Tech.*, vol. 9, No. 10, pp. 1289-1294, Oct. 1991.

[81] K. C. Gupta, R. Garg, I. Bahl, and P. Bhartia, Microstrip lines and slotlines, 2nd Ed., Norwood, MA., Artech House, 1996.

[82] H. Hayashi, and T. Ishikawa,"Design, fabrication and experiment of GaAs Traveling-wave directional coupler optical modulators," *Electron. Commun. Japan*, vol. 74, pp. 29-39, 1991.

[83] K. Wu, R. Vahldieck, "Hybrid-mode analysis of homogenously and inhomogenously doped low-loss slow-wave coplanar transmission lines," *IEEE Trans. Microwave Theory Tech.*, vol.39, pp. 1348-1360, 1991.

[84] V. M Hietala, S. H. Kravitz, M. G. Armendariz, G. A. Vawter, R. F. Carson, "High-performance GaAs/AlGaAs optical phase modulators for microwave/photonic integrated circuits," *SPIE Conf.*, vol. 2155, pp. 29-36, 1994.

[85] K. Kubota, J. Noda, and O. Mikami, "Traveling-wave optical modulator using directional coupler LiNbO3 waveguide," *IEEE J. Quantum Electron.*, vol. 16, pp. 754-760, 1981.

APPENDIX I

Schematic Diagrams of the Electrodes on the Masks

The layout of the electrodes designed on LIT-1, LIT-2, and LIT-3 mask sets are presented. The LIT-1 mask set contains five different types of electrodes that provides a total of 30 different electrodes of various dimensions. The electrodes on LIT-1 are of CPW, CPWA, CPWB, CPWC, and CPWD (symmetric) configurations. Different capacitive elements are periodically added to the signal conductor, ground conductor, or both. Various dimensions of CPWD (symmetric), CPWD-as (asymmetric), CPSD, and CPSD-id (interdigitated) electrode structures provide 24 distinct electrodes on LIT-2 mask set. LIT-3 provides 30 electrodes of different configurations including CPWD-as, CPSD-id, and CPSD. A CPWD-as electrode with 90°-bend G-S-G pad is also added to the LIT-3 mask set to study the effect of the 90°-bend at very high frequency. This enables the designer to apply the optical and electrical signal at right angles and therefore provides more freedom in measurement, integration, and packaging. On LIT-3 The physical dimensions of all the electrodes on LIT-1, LIT-2, and LIT-3 mask sets are given in Appendix II.

Figure A1.1 Schematic diagram of a uniform coplanar waveguide, CPW.

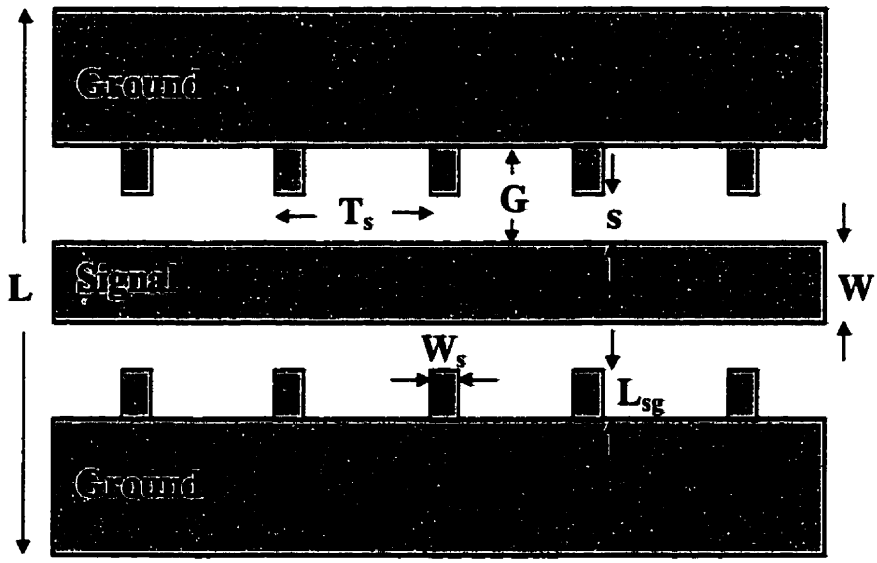

Figure A1.2 Schematic diagram of a loaded coplanar waveguide, CPWA, with narrow fins on the ground electrodes.

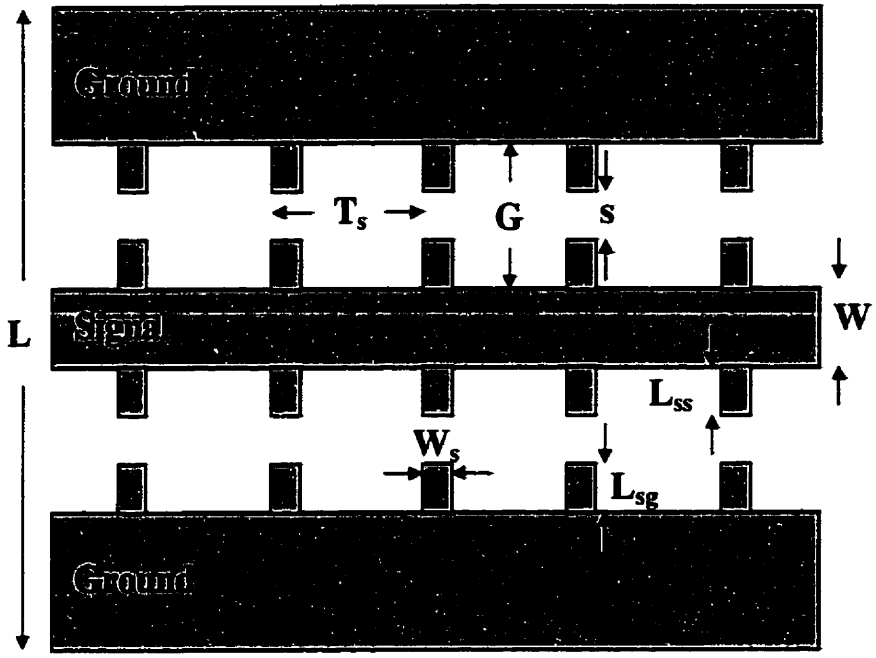

Figure A1.3 Schematic diagram of a loaded coplanar waveguide, CPWB, with narrow fins on the signal and ground electrodes.

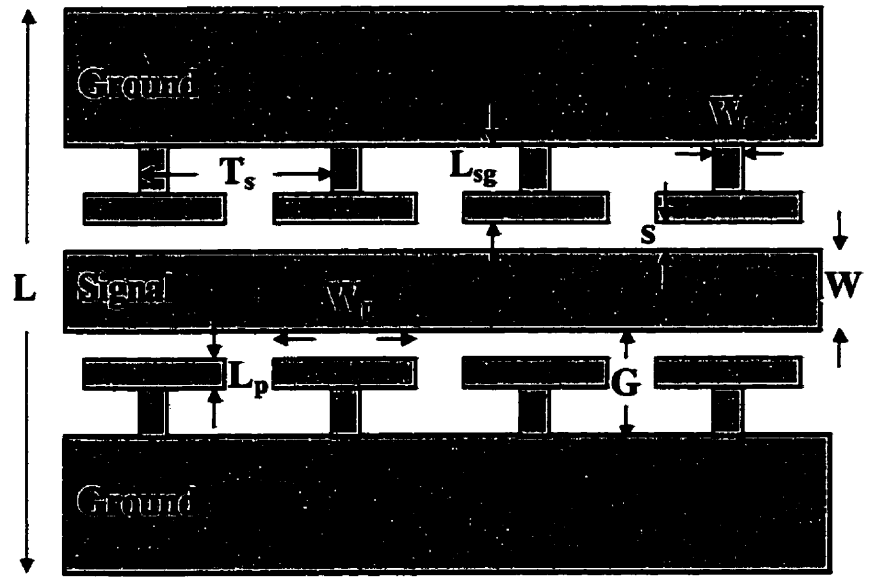

Figure A1.4 Schematic diagram of a loaded coplanar waveguide, CPWC, with narrow fins and pads on the ground electrodes.

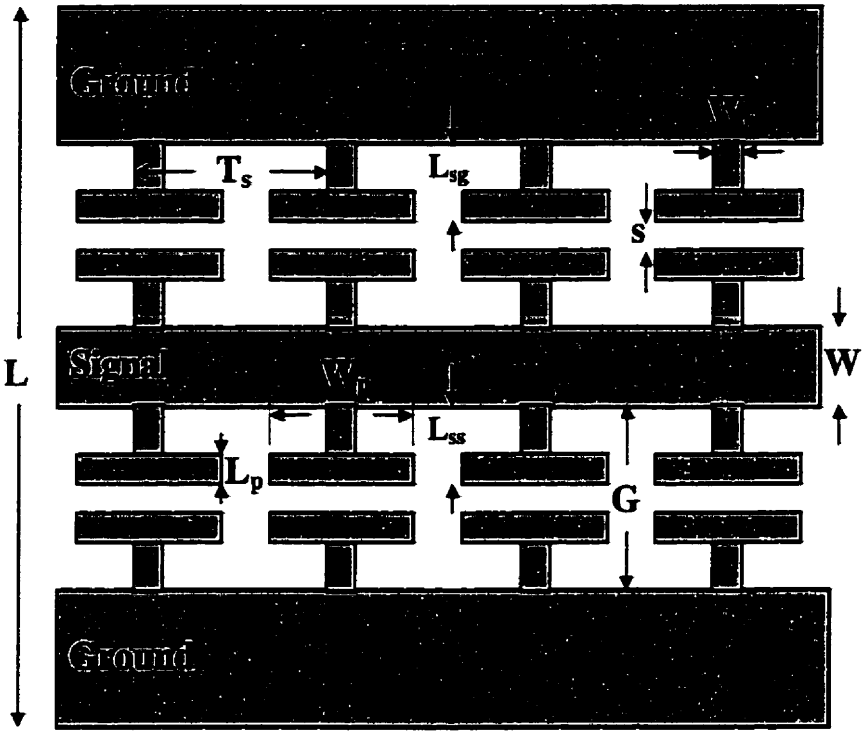

Figure A1.5 Schematic diagram of a loaded coplanar waveguide, CPWD, with narrow fins and pads on the signal and ground electrodes (CPWD-as when $L_{ss}<L_{sg}$).

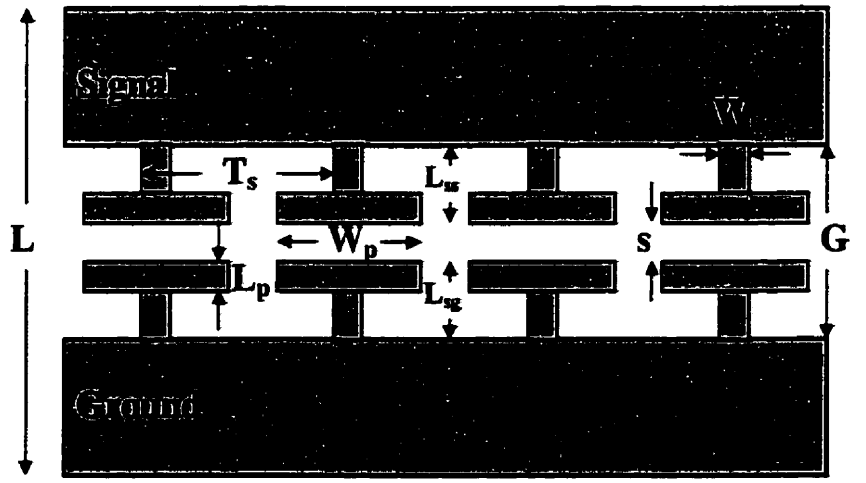

Figure A1.6 Schematic diagram of a loaded coplanar strips, CPSD, with narrow fins and pads on the signal and ground electrodes.

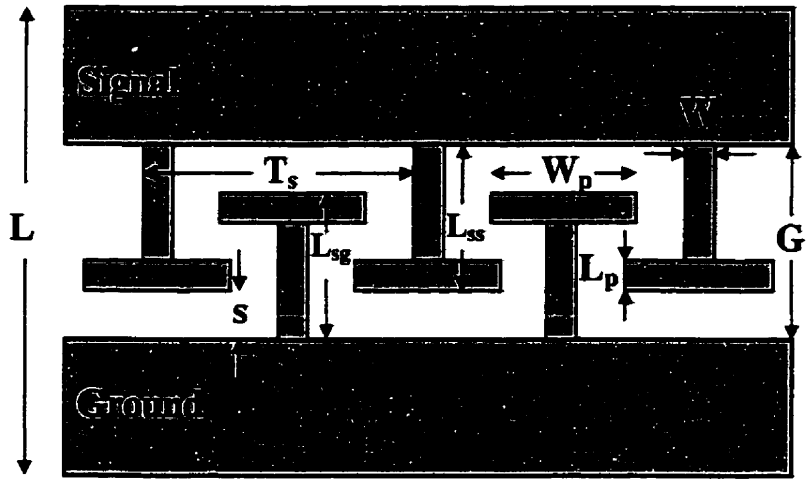

Figure A1.7 Schematic diagram of a loaded coplanar strips, CPSD-id, with interdigitated fins and pads on the signal and ground electrodes.

APPENDIX II

Design Parameters of the Modulators Designed on Three Mask Sets

The design parameters of the microwave electrodes and optical structures for all the electro-optic modulators designed on LIT-1 and LIT-2 mask sets are given below. The electrode configurations are given in Appendix I. Following comments are necessary for the definition of symbols used in the tables.

Waveguide types: determine the types of optical structure integrated with the electrode.

MZ: Symmetrical Mach-Zehnder interferometer with s-bend waveguides at the input and output junctions.

MZ-as: Asymmetrical Mach-Zehnder interferometer with s-bend waveguides at the input and output junctions. The optical path phase difference between the two arms at 1.55 μm is $\pi/2$.

MZ-Y: Symmetrical Mach-Zehnder interferometer with straight waveguides at the input and output junctions.

MZ-3: Symmetrical Mach-Zehnder interferometer with 3-branch coupler and s-bend waveguides at the input and output junctions.

Channel(ch): A straight waveguide.

2-channel(2-ch): 2 straight waveguides.

Location: determine the position of the optical structure relative to the microwave electrode.

a: The electrodes are on either side of the ridge optical waveguides. In the case of CPS electrode, the waveguide is in the centre of the gap. In the case of CPW electrode, the MZ is placed symmetrically relative to the centre (signal) electrode.

b: The optical waveguide is placed under the pads of signal and ground electrode. One arm of the MZ interferometer is under the pads of signal electrode and the other arm is under the pads of the ground electrode of the opposite side.

c: The optical waveguide is placed under the inner edge of the signal and ground electrodes.

The last two columns of each table also provide the simulation results without considering the effect of the ridge optical waveguide.

Table A2.1 Design parameters for electrodes designed on LIT-1 mask set.

Elec. No.	Ws	Lcs	Lg	Wf	Lf	W	S	L	T	Elec. Type	WG type	WG width	Dist. from	WG gap	Length (mm)	Zo	Vph
1						40	10	300		CPW	MZ	3	a	50	10	39.5	11.37
2						40	25	300		CPW	MZ	3	a	65	10	50.8	11.37
3						70	40	300		CPW	MZ	3	a	110	10	51.1	11.37
4	30		55			40	5	300	40	CPWA	MZ	3	a	45	10	45	8.78
5	20		55			40	5	300	40	CPWA	MZ	3	a	45	10	48.7	8.76
6	10		60			50	5	300	40	CPWA	MZ	3	a	55	10	50.7	8.86
7	30		65			50	10	300	40	CPWA	MZ	3	a	60	10	48.4	8.92
8	20		65			60	10	300	40	CPWA	MZ	3	a	70	10	49.1	8.89
9	20		65			60	10	300	40	CPWA	MZ	3	a	65	10	49.1	8.89
10	20		65			60	10	300	40	CPWA	MZ	3	a	75	10	49.1	8.89
11	10		65			70	10	300	40	CPWA	MZ	3	a	80	10	51.4	8.95
12	20	20	20			20	5	300	40	CPWB	MZ	3	a	65	10	49.4	8.85
13	20	25	25			20	10	300	40	CPWB	MZ	3	a	80	10	54.2	8.73
14	10		55			50	10	300	20	CPWA	MZ	3	a	60	10	51.5	8.8
15	40		65			40	5	300	80	CPWA	MZ	3	a	45	10	48.6	8.92
16	10		55	30	10	50	10	300	40	CPWC	MZ	3	a	60	10	49.3	8.91
17	5		50	15	5	50	10	300	20	CPWC	MZ	3	a	60	10	49.3	8.84
18	5	20	20	15	5	60	10	300	20	CPWD	MZ	3	a	80	10	50.1	8.44
19						40	10	300		CPW	MZ-Y	3	a	50	10	39.5	11.37
20	20		65			60	10	300	40	CPWA	MZ-Y	3	a	70	10	49.1	8.89
21						40	10	300		CPW	MZ-3	3	a	50	10	39.5	11.37
22	20		65			60	10	300	40	CPWA	MZ-3	3	a	70	10	49.1	8.89
23						40	10	300		CPW	MZ-3	3	a	50	10	39.5	11.37
24	20		65			60	10	300	40	CPWA	MZ-3	3	a	70	10	49.1	8.89
25	20		65			60	10	300	40	CPWA	MZ	4	a	70	10	49.1	8.89
26	20		65			60	10	300	40	CPWA	MZ	5	a	70	10	49.1	8.89
27						70	40	400		CPW	MZ	3	a	110	10	49.5	11.37
28	30		55			40	5	400	40	CPWA	MZ	3	a	45	10	44.6	8.85
29	10		65			70	10	400	40	CPWA	MZ	3	a	80	10	51.8	9.01
30	5	40	40	15	5	120	10	540	20	CPWD	MZ	4	a	210	10		

Table A2.2 Design parameters for electrodes designed on LIT-2 mask set.

Elec. No.	Ws	Ls	Lg	Wf	Lf	W	S	L	Ts	Elec. Type	WG type	WG width	Location	WG's gap	length (mm)	Zo	Vph
1						10	6	200		CPW					10		
2						10	6	200		CPW	2-ch	5	a		10		
3	4	30	30	30	4		4	320	38	CPSD	ch	3	a		15	52.1	8.85
4	4	29	29	30	4		6	320	36	CPSD	ch	5	a		15	52.9	8.89
5	2	30	30	30	4		4	320	36	CPSD	ch	3	a		15	52.2	8.85
6	4	15	15	30	4	20	4	300	51	CPWD	MZ	3	b	54	10	50.4	8.87
7	2	15	15	30	4	20	4	300	50	CPWD	MZ	3	b	54	10	50.5	8.86
8	4	15	15	30	5	20	4	300	54	CPWD	MZ	4	b	54	10	51.8	8.9
9	4	14	14	30	5	20	6	300	48	CPWD	MZ	4	b	54	10	52	8.91
10	4	15	15	30	6	20	4	300	55	CPWD	MZ	5	b	54	10	51.7	8.86
11	4	14	14	30	6	20	6	300	48	CPWD	MZ	5	b	54	10	51.5	8.85
12	4	14	14	30	2	20	6	300	39	CPWD	MZ	5	a	54	10	51.1	8.84
13	2	14	14	30	2	20	6	300	36	CPWD	MZ	5	a	54	10	50.6	8.87
14	4	15	15	30	2	20	4	300	44	CPWD	MZ	3	a	54	10	52.1	8.88
15	4	15	15	30	4	20	4	300	51	CPWD	MZ	3	a	54	10	50.4	8.87
16	2	15	15	30	4	20	4	300	50	CPWD	MZ	3	a	54	10	50.5	8.86
17	4	22	22	30	4	30	4	300	59	CPWD	MZ	3	b	78	10	51.7	8.9
18	4	22	22	30	5	30	4	300	61	CPWD	MZ	4	b	78	10	51.4	8.87
19	4	22	22	30	6	30	4	300	63	CPWD	MZ	5	b	78	10	51.3	8.86
20	4	10	34	30	2	30	4	300	43	CPWD-as	MZ	3	a	54	10	51.9	8.89
21	4	10	34	30	4	30	4	300	50	CPWD-as	MZ	3	b	54	10	51.6	8.89
22	4	7	21	30	2	20	6	300	32	CPWD-as	MZ	5	a	40	10	52	8.85
23	2	16	16	30	2		4	136	36	CPSD-id	MZ	3	c	25	10	50.3	8.86
24	4	16	16	30	2		4	136	38	CPSD-id	MZ	5	c	27	10	51.1	8.87

Table A2.3 Design parameters for electrodes designed on LIT-3 mask set.

Elec. No.	Ws	Ls	Lg	Wp	Lp	W	S	L	R	Elec. Type	WG type	WG width	Location	WG gap	length (mm)	Zc	Vpp
1	2	28	28	96	2		2	340	100	CPSD	ch	2	a		23	53	9.38
2	2	28	28	96	2		3	340	100	CPSD	ch	2.5	a		23	54	9.51
3	2	28	28	90	2		2	340	100	CPSD	ch	2	a		23		
4	2	28	28	90	2		3	340	100	CPSD	ch	2.5	a		23		
5	2	28	28	84	2		2	340	100	CPSD	ch	2	a		23		
6	2	28	28	84	2		3	340	100	CPSD	ch	2.5	a		23		
7	2	6	16	90	2	20	2	300	100	CPWD-as	MZ	2.5	b	34	20	46.3	8.94
8	2	6	16	90	2	20	3	300	100	CPWD-as	MZ	2.5	b	35	20	47.5	9.17
9	2	6	16	84	2	20	2	300	100	CPWD-as	MZ	2.5	b	34	20	46.9	9.06
10	2	6	16	84	2	20	3	300	100	CPWD-as	MZ	2.5	b	35	20	48.1	9.3
11	2	6	16	75	2	20	2	300	100	CPWD-as	MZ	2.5	b	34	20		
12	2	6	16	75	2	20	3	300	100	CPWD-as	MZ	2.5	b	35	20		
13	2	6	16	90	2	20	2	300	100	CPWD-as	MZ-as	2.5	b	34	20	46.3	8.94
14	2	6	16	90	2	20	3	300	100	CPWD-as	MZ-as	2.5	b	35	20	47.5	9.17
15	2	6	16	90	2	20	2	300	100	CPWD-as	MZ	2	a	34	20	46.3	8.94
16	2	6	16	90	2	20	3	300	100	CPWD-as	MZ	2.5	a	35	20	47.5	9.17
17	2	6	16	84	2	20	2	300	100	CPWD-as	MZ	2	a	34	20	46.9	9.06
18	2	6	16	84	2	20	3	300	100	CPWD-as	MZ	2.5	a	35	20	48.1	9.3
19	2	6	16	75	2	20	2	300	100	CPWD-as	MZ	2	a	34	20		
20	2	6	16	75	2	20	3	300	100	CPWD-as	MZ	2.5	a	35	20		
21	2	6	16	90	1	20	2	300	100	CPWD-as	MZ	2	a	34	20	48.5	9.33
22	2	6	16	90	1	20	3	300	100	CPWD-as	MZ	2.5	a	35	20	49.6	9.53
23	2	18	18	90	2		2	200	100	CPSD-id	MZ	2.5	c	22.5	20	44.3	8.92
24	2	17	17	90	2		3	200	100	CPSD-id	MZ	2.5	c	22.5	20	45.4	9.13
25	2	18	18	80	2		2	200	100	CPSD-id	MZ	2.5	c	22.5	20	45.4	9.14
26	2	17	17	80	2		3	200	100	CPSD-id	MZ	2.5	c	22.5	20	46.5	9.35
27	2	18	18	80	2		2	200	100	CPSD-id	MZ-as	2.5	c	22.5	20	45.4	9.14
28	2	17	17	80	2		3	200	100	CPSD-id	MZ-as	2.5	c	22.5	20	46.5	9.35
29	2	18	18	180	2		2	200	200	CPSD-id	MZ	2.5	c	22.5	20	45.3	9.13
30	2	17	17	180	2		3	200	200	CPSD-id	MZ	2.5	c	22.5	20	46.3	9.33

APPENDIX III

Fortran Code for Transmission Line Parameter Extraction

This appendix gives the code, written in Fortran 77, to calculate the transmission line parameters from the measured s-parameters of the line. It first calculates the ABCD matrix and then characteristic impedance, phase velocity, and insertion loss.

```
c       This program calculates the transmission line parameters. S-parameters and
c       physical dimensions of the transmission line are the inputs and the outputs
c       are the phase velocity, effective index, characteristic impedance and
c       microwave loss.

        complex s11,s21,s12,s22,A,B,C,D,z0,gamma
        character*150 text
        character*20 filein,fileout
        integer pos1,pos2
        real l,loss,mags11,mags21,mags12,mags22,neff,lghtspd
        real z0r,z0i

        print*,'enter the input file name! '
        read(*,5)filein
```

```
      print*,'enter the output file name! '
      read(*,5)fileout
5     format(A)
      open(unit=1,file=filein)
      open(unit=2,file=fileout)

      write(2,150)
150   format(' Freq(GHz)  Imp. real(ohm) Imp. imag.(ohm)        Vph(cm/ns)
     $         Neff      Loss(dB/cm)',//)

c     Impedance of the measurement system (network analyzer).
      zn=50.

      print*,'Enter the length of the transmission line'
      read*,l
      print*,'enter the number of data lines to be processed! '
      read*,num

      pi=4.*atan(1.)
      giga=1.e9
      lghtspd=3.e8
      pos1=1
      pos2=1
      n=0

      do 20 i=1,4
20    read(1,*)
      do 100 m=1,num
      read(1,110)text
110   format(A)
      read(text,*)freq,mags11,angs11,mags21,angs21,mags12,angs12,mags22,angs22

      angs11=angs11*pi/180.
      angs21=angs21*pi/180.
      angs12=angs12*pi/180.
      angs22=angs22*pi/180.

      s11=cmplx(mags11*cos(angs11),mags11*sin(angs11))
      s21=cmplx(mags21*cos(angs21),mags21*sin(angs21))
      s12=cmplx(mags12*cos(angs12),mags12*sin(angs12))
      s22=cmplx(mags22*cos(angs22),mags22*sin(angs22))

c     calculating the ABCD matrix element
```

```
      A=0.5*((1.+s11)*(1.-s22)+s12*s21)/s21
      B=0.5*zn*((1.+s11)*(1.+s22)-s12*s21)/s12
      C=0.5*((1.-s11)*(1.-s22)-s12*s21)/(zn*s21)
      D=0.5*((1.-s11)*(1.+s22)+s12*s21)/s12

c     Transmission line parameters calculation

      z0=(2.0*B)/((D-A)+csqrt((A+D)**2.0-4.0))
      if(real(z0).lt.0)then
            z0=(2.0*B)/((D-A)-csqrt((A+D)**2.0-4.0))
      endif
      z0r=real(z0)
      z0i=aimag(z0)
      gamma=(A+D)/2.0+csqrt(((A+D)/2.0)**2.0-1.0)
      if(real(gamma).lt.0)then
            gamma=(A+D)/2.0-csqrt(((A+D)/2.0)**2.0-1.0)
      endif

      anggam=atan2(aimag(gamma),real(gamma))
      if(anggam.lt.0.)then
      pos2=0
      else
      pos2=1
      endif

      if(pos2.ne.pos1)n=n+1
      if(pos2.eq.0)then
            beta=(n*pi)+(pi+anggam)
      else
            beta=(n*pi)+anggam
      endif

      alpha=log(real(csqrt(gamma*conjg(gamma))))/l
      vph=2.*pi*freq*l/beta
      neff=100.*lghtspd/(giga*vph)
      loss=8.686*alpha

      pos1=pos2
      write(2,120)freq,z0r,z0i,vph,neff,loss
120   format(f9.4,5f15.5)
100   continue

      stop
      end
```

APPENDIX IV

Microwave Measurement Results

This appendix contains the results of the microwave measurement on SI-GaAs substrate for LIT-1, LIT-2, and LIT-3 mask sets. The results are given on SI-GaAs to isolate the effects of materials on the microwave performance of the electrodes. The results include average characteristic impedance (Z_{0avg}), average phase velocity (V_{phavg}), and microwave insertion loss at the maximum measured frequency. We have also included some physical dimensions of the electrodes that are relevant to their performance, such as the gap between the main signal and ground electrodes (G), width of the signal electrodes (W_{signal}), longitudinal overlap factor (Γ_l), and interelectrode gap (S).

Table A4.1 Microwave characteristics and some physical dimensions of slow-wave electrodes on LIT-1 mask set. Loss is measured at 35 GHz.

Elect. #	Z_{0avg} (Ω)	V_{phavg} (cm/nsec)	α_m (dB/cm)	G(μm)	W_{signal}(μm)	S(μm)	Γ_l
CPW1	31.7	12.45	3.4	10	40	10	1
CPW2	44.9	11.98	2.1	25	40	25	1
CPW3	46.8	11.74	1.6	40	70	40	1
CPWA4	39.2	8.82	5.7	60	40	5	0.75
CPWA5	43.3	8.76	4.6	60	40	5	0.5
CPWA6	46	8.94	3.8	65	50	5	0.25
CPWA7	NA	NA	NA	75	50	10	0.75
CPWA8	45.4	8.85	5.2	75	60	10	0.5
CPWA9	45.4	8.85	5.2	75	60	10	0.5
CPW10	45.4	8.85	5.2	75	60	10	0.5
CPWA11	47.5	9.12	5	75	70	10	0.25
CPWB12	43.5	9.06	5.1	45	20	5	0.5
CPWB13	49	9.01	4.7	60	20	10	0.5
CPWA14	45.7	8.94	4.7	65	50	10	0.5
CPWA15	44.9	8.93	5	70	40	5	0.5
CPWC16	45.7	8.86	4.1	65	50	10	0.75
CPWC17	44.9	8.93	3.9	60	50	10	0.75
CPWD18	44.8	8.73	3.8	50	30	10	0.75
CPW19	31.7	12.45	3.4	10	40	10	1
CPW20	45.4	8.85	5.2	75	60	10	0.5
CPW21	31.7	12.45	3.4	10	40	10	1
CPW22	45.4	8.85	5.2	75	60	10	0.5
CPW23	31.7	12.45	3.4	10	40	10	1
CPW24	45.4	8.85	5.2	75	60	10	0.5
CPW25	45.4	8.85	5.2	75	60	10	0.5
CPW26	45.4	8.85	5.2	75	60	10	0.5
CPW27	46.8	11.74	1.6	40	70	40	1
CPWA28	39.2	8.82	5.7	60	40	5	0.75
CPWA29	45.8	9.32	4.5	75	70	10	0.25
CPWD30	37.3	8.29	2.4	50	120	10	0.75

Table A4.2 Microwave characteristics and some physical dimensions of slow-wave electrodes on LIT-2 mask set. Loss is measured at 40 GHz.

Elect. #	Z_{0avg} (Ω)	V_{phavg} (cm/nsec)	α_m (dB/cm)	G(μm)	W_{signal}(μm)	S(μm)	Γ_l
CPW1	44.826	11.162	7.5	6	97	6	1
CPW2	44.951	11.164	7.5	6	97	6	1
CPSD3	53.097	8.562	1.9	64	128	4	0.79
CPSD4	55.001	8.795	2	64	128	6	0.83
CPSD5	53.257	8.5	2	64	128	4	0.83
CPWD6	47.19	8.489	3.9	34	20	4	0.59
CPWD7	47.327	8.428	3.9	34	20	4	0.60
CPWD8	47.457	8.537	4	34	20	4	0.56
CPWD9	NA	NA	NA	34	20	6	0.63
CPWD10	47.183	8.511	4.1	34	20	4	0.55
CPWD11	48	8.674	4.1	34	20	6	0.63
CPWD12	NA	NA	NA	34	20	6	0.77
CPWD13	48.122	8.451	3.8	34	20	6	0.83
CPWD14	NA	NA	NA	34	20	4	0.68
CPWD15	47.323	8.452	4.1	34	20	4	0.59
CPWD16	47.406	8.407	4	34	20	4	0.60
CPWD17	47.733	8.462	3	48	30	4	0.51
CPWD18	47.726	8.487	3	48	30	4	0.49
CPWD19	47.654	8.484	3	48	30	4	0.48
CPWD-as20	47.782	8.32	3.2	48	30	4	0.70
CPWD-as21	46.923	8.358	3.5	48	30	4	0.60
CPWD-as22	48.05	8.539	4	34	20	6	0.94
CPSD-id23	43.874	7.647	4.6	20	58	4	0.83
CPSD-id24	45.135	7.763	4.8	20	58	4	0.80

Table A4.3 Microwave characteristics and some physical dimensions of slow-wave electrodes on LIT-3 mask set. Loss is measured at 40 GHz.

Elect. #	Z_{0avg} (Ω)	V_{phavg} (cm/nsec)	α_m (dB/cm)	G(μm)	W_{signal}(μm)	S(μm)	Γ_l
CPSD1	52.22	8.997	3.3	58	141	2	0.96
CPSD2	53.46	9.19	3.1	59	140.5	3	0.96
CPSD3	52.823	9.065	2.97	58	141	2	0.90
CPSD4	53.432	9.259	2.95	59	140.5	3	0.90
CPSD5	53.085	9.159	2.86	58	141	2	0.84
CPSD6	54.156	9.376	3.1	59	140.5	3	0.84
CPWD-as7	45.044	8.676	5.7	24	20	2	0.90
CPWD-as8	46.404	8.95	5.3	24	20	3	0.90
CPWD-as9	45.576	8.794	5.4	24	20	2	0.84
CPWD-as10	47.007	9.063	5.1	24	20	3	0.84
CPWD-as11	46.524	8.987	5.2	24	20	2	0.75
CPWD-as12	47.823	9.245	5	24	20	3	0.75
CPWD-as13	44.939	8.660	5.6	24	20	2	0.90
CPWD-as14	46.384	8.938	5.4	24	20	3	0.90
CPWD-as15	44.043	8.396	5.9	24	20	2	0.90
CPWD-as16	45.507	8.733	5.6	24	20	3	0.90
CPWD-as17	44.747	8.526	5.8	24	20	2	0.84
CPWD-as18	46.186	8.852	5.4	24	20	3	0.84
CPWD-as19	45.843	8.735	5.6	24	20	2	0.75
CPWD-as20	47.212	9.046	5.2	24	20	3	0.75
CPWD-as21	NA	NA	NA	24	20	2	0.90
CPWD-as22	NA	NA	NA	24	20	3	0.90
CPSD-id23	41.525	8.338	4.5	20	90	2	0.90
CPSD-id24	42.705	8.583	4.4	20	90	3	0.90
CPSD-id25	42.841	8.604	4.8	20	90	2	0.80
CPSD-id26	44.039	8.853	4.2	20	90	3	0.80
CPSD-id27	42.907	8.596	5	20	90	2	0.80
CPSD-id28	44.039	8.847	4.1	20	90	3	0.80
CPSD-id29	42.073	8.398	5	20	90	2	0.90
CPSD-id30	43.310	8.640	4.3	20	90	3	0.90

APPENDIX V

Sensitivity Analysis of the Transmission Line Parameters

The ABCD matrix of a transmission line as a function of s-parameters is as follow [76]:

$$\begin{bmatrix} A & B \\ C & D \end{bmatrix} = \begin{bmatrix} \dfrac{(1+s_{11})(1-s_{22})+s_{12}s_{21}}{2s_{21}} & Z_{0r}\dfrac{(1+s_{11})(1+s_{22})-s_{12}s_{21}}{2s_{21}} \\ \dfrac{1}{Z_{0r}}\dfrac{(1-s_{11})(1-s_{22})-s_{12}s_{21}}{2s_{21}} & \dfrac{(1-s_{11})(1+s_{22})+s_{12}s_{21}}{2s_{21}} \end{bmatrix} \quad \text{(A5.1)}$$

where Z_{0r} is the reference characteristic impedance of the measurement system, 50 Ω. The characteristic impedance, Z_0, of the transmission line can thus be found using the following expressions:

$$Z_0 = \frac{2B}{D-A\pm\sqrt{(A+D)^2-4}} \quad \text{(A5.2)}$$

Equation A5.2 yields two solutions for Z_0. The physically meaningful value of Z_0 has a positive real part. The measured results presented in chapter 5 show a large periodic ripple in Z_0. This phenomenon is not observed in other line parameters such as phase velocity and microwave loss. An analytical expression is extracted for the sensitivity of

characteristic impedance. A relative error in the measurement of amplitude and phase of the s-parameters is considered. These errors are assumed to be independent of each other. For the sake of simplicity of equations, the transmission line is considered to be symmetrical. This, in fact, is a good assumption for the electrodes under study. Therefore, $s_{11} = s_{22}$ and $s_{12} = s_{21}$.

$$\Delta A = A_1 \Delta s_{11} + A_2 \Delta s_{12} \tag{A5.3}$$

$$\Delta B = B_1 \Delta s_{11} + B_2 \Delta s_{12} \tag{A5.4}$$

$$\Delta Z_0 = Z_1 \Delta B + Z_2 \Delta A \tag{A5.5}$$

where

$$A_1 = -\frac{s_{11}}{s_{12}} \tag{A5.6}$$

$$A_2 = \frac{s_{11}^2 + s_{12}^2 - 1}{2 s_{12}^2} \tag{A5.7}$$

$$B_1 = Z_{0r}\left(\frac{1 + s_{11}}{s_{12}}\right) \tag{A5.8}$$

$$B_2 = -\frac{Z_{0r}}{2}\left\{1 + \left(\frac{1 + s_{11}}{s_{12}}\right)^2\right\} \tag{A5.9}$$

$$Z_1 = \frac{Z_0}{B} \tag{A5.10}$$

$$Z_2 = Z_0\left(\frac{1}{\sqrt{A^2 - 1}} + \frac{A}{A^2 - 1}\right) \tag{A5.11}$$

Δs_{11} and Δs_{12} are absolute errors in the complex s-parameters. The absolute error in any s-parameter is defined as follows:

$$\Delta s = \Delta|s| e^{j\Phi} + j s \Delta\Phi \tag{A5.12}$$

$\Delta|s|$ and $\Delta\Phi$ are the absolute error in the magnitude and phase of the s-parameter, respectively. ΔZ_0 can also be expressed as a function of Δs_{11} and Δs_{12}.

$$\Delta Z_0 = Z_3 \Delta s_{11} + Z_4 \Delta s_{12} \tag{A5.13}$$

$$Z_3 = Z_1 B_1 + Z_2 A_1 \tag{A5.14}$$

$$Z_4 = Z_1 B_2 + Z_2 A_2 \tag{A5.15}$$

Since ΔZ_0 is a complex value, the real, ΔZ_r, and imaginary, ΔZ_i, parts are given as:

$$\Delta Z_r = real(Z_3 s_{11})\Delta|s_{11}|_r + \Phi_{11} imag(Z_3 s_{11})\Delta\Phi_{11r} + real(Z_4 s_{12})\Delta|s_{12}|_r + \Phi_{12} imag(Z_4 s_{12})\Delta\Phi_{12r} \tag{A5.16}$$

$$\Delta Z_i = imag(Z_3 s_{11})\Delta|s_{11}|_r + \Phi_{11} real(Z_3 s_{11})\Delta\Phi_{11r} + imag(Z_4 s_{12})\Delta|s_{12}|_r + \Phi_{12} real(Z_4 s_{12})\Delta\Phi_{12r} \tag{A5.17}$$

$\Delta|s_{ij}|_r$ and $\Delta\Phi_{ijr}$ are the relative error in the magnitude and phase of s_{ij}. These equations were used to estimate the measurement error in characteristic impedance. It was found that the maximum error occurs when the magnitude of s_{11} and s_{12} are small and therefore their accurate measurement is practically impossible. A small error of 0.1% in the magnitude and phase of s-parameters can cause an error of more than 15% at high frequencies.

LIST OF PUBLICATIONS:

1. H. R. Khazaei, O. Berolo, W. Wang, P. Maigné, M. Young, K. Ozard, M. Reeves, F. M. Ghannouchi," Experimental analysis of microwave loss due to substrate carrier concentration in traveling-wave electro-optic modulators," *SPIE* vol. 3491, *Applications of Photonic Technology 3*, by G. A. Lampropoulos and R. A. Lessard, , pp. 90-95, 1998.
2. E. Berolo, H. R. Khazaei, W. Wang, F. M. Ghannouchi, N. A. F. Jaeger, and F. Rahmatian," Millimeter-wave laser modulation using III-V semiconductor traveling wave electro-optic Mach-Zehnder interferometer structures," *Symp. on Antenna Tech. and Appl. Electromag.* (ANTEM'98) Ottawa, pp. 365-369, Aug. 1998.
3. H. R. Khazaei, E. Berolo, and F. Ghannouchi,"High-speed slow-wave coplanar strip GaAs/AlGaAs electro-optic laser modulator," *Optical and Microwave Technology Letters*, vol. 19, No. 3, pp. 184-186, Oct. 1998.
4. H. R. Khazaei, W. J. Wang, E. Berolo, and F. Ghannouchi,"High speed GaAs/AlGaAs traveling wave electro-optic modulators," *Proc. SPIE, Integrated Optic Devices II*, San Jose, CA, USA, vol. 3278, pp. 94-100, Jan. 1998.
5. W. Wang, H. R. Khazaei, E. Berolo, P. Maigné, D. Coulas, J. Noad, and P. Borkowski,"GaAs/$Al_yGa_{1-y}As$ waveguide leakage loss reduction by inserting thin AlAs/ $Al_xGa_{1-x}As$ layers into the bottom," *Proc. SPIE, Integrated Optic Devices II*, San Jose, CA, USA, vol. 3278, pp. 187-190, Jan. 1998.
6. H. R. Khazaei, O. Berolo, R. James, W. J. Wang, P. Maigné, M. Young, K. Ozard, M. Reeves, and F. M. Ghannouchi,"Charge carrier effect on the microwave losses observed on traveling wave electro-optic modulators," *Optical and Microwave Technology Letters*, vol. 17, No. 4, pp. 236-241, March 1998.
7. H. R. Khazaei, R. James, E. Berolo, F. Rahmatian, N. A. F. Jaeger, and F. Ghannouchi,"Novel coplanar strip slow wave structure for ultra-wide bandwidth electro-optic modulators," *Optical and Microwave Technology Letters*, vol. 15, No. 5, pp. 303-305, 1997.
8. H.R. Khazaei, R. James, E. Berolo, and F. Ghannouchi,"Millimeter-wave coplanar structures on InP for electro-optic modulation applications," *Proc. SPIE, Emerging Components and Technologies for All-Optical System II*, Boston, MA, USA, Nov. 96, vol. 2918, pp. 60-66.
9. F. Rahmatian, A. Kulpa, N.A.F. Jaeger, R. James, M. Bégin, H.R. Khazaei, E. Berolo, and F. Ghannouchi,"Low-loss slow-wave coplanar strips and coplanar waveguides for electro-optic modulators," *Proc. CLEO/Europe 96*, Hamburg, Germany, Sept. 96, p. 255.

10. M. Bégin, H. R. Khazaei, F. Ghannouchi, R. James, E. Berolo, F. Rahmatian, N.A.F. Jaeger,"Slow-wave coplanar waveguides for GaAs-based electro-optic modulators," *Proc. XXVth General Assembly of URSI*, Lille, France, 96, p. 194.

11. H.R. Khazaei, R. James, E. Berolo, F. Ghannouchi,"Millimeter wave coplanar structures on InP for modulation applications," *Applications of Photonic Technology 2*, by G. A. Lampropoulos and R. A. Lessard, Plenum Press, New York, pp. 451-456, 1997.